UNIVERSITÉ DE MONTRÉAL

TWO-WAY FLUID-STRUCTURE COUPLING METHODOLOGY FOR MODELING 3D FLEXIBLE HYDROFOILS IN VISCOUS FLOW

ZAHRA MORTAZAVINIA
DÉPARTEMENT DE GÉNIE MÉCANIQUE
ÉCOLE POLYTECHNIQUE DE MONTRÉAL

THÈSE PRÉSENTÉE EN VUE DE L'OBTENTION
DU DIPLÔME DE PHILOSOPHIÆ DOCTOR
(GÉNIE MÉCANIQUE)
AOÛT 2018

UNIVERSITÉ DE MONTRÉAL

ÉCOLE POLYTECHNIQUE DE MONTRÉAL

Cette thèse intitulée :

TWO-WAY FLUID-STRUCTURE COUPLING METHODOLOGY FOR MODELING 3D FLEXIBLE HYDROFOILS IN VISCOUS FLOW

présentée par : MORTAZAVINIA Zahra
en vue de l'obtention du diplôme de : Philosophiæ Doctor
a été dûment acceptée par le jury d'examen constitué de :

M. REGGIO Marcelo, Ph. D., président
M. CAMARERO Ricardo, Ph. D., membre et directeur de recherche
M. GUIBAULT François, Ph. D., membre et codirecteur de recherche
M. TRÉPANIER Jean-Yves, Ph. D., membre
M. DANESHMAND Farhang, Ph. D., membre externe

DEDICATION

To my family
for their sincere love...

ACKNOWLEDGEMENTS

First and foremost, I would like to express my sincere gratitude to my advisors Professor Ricardo Camarero and Professor François Guibault for the continuous support of my Ph.D study and research, for their patience, motivation, enthusiasm, and immense knowledge. Their guidance helped me in all the time of research and writing of this thesis.

My time in Montreal was made enjoyable in large part due to the many friends and groups that became a part of my life. I am grateful for time spent with all of them and our memorable moments. I warmly thank Mr. Mojtaba Mirzaei and Mr. Soheil Namvar, for their valuable advices and helps during my study.

Computations are made on the supercomputers "Briarée" from "Université de Montréal", and "Guillimin" from "McGill University", managed by Calcul Québec and Compute Canada. The operation of this supercomputer is funded by the Canada Foundation for Innovation (CFI), the ministère de l'Économie, de la science et de l'innovation du Québec (MESI) and the Fonds de recherche du Québec - Nature et technologies (FRQ-NT).

Last, but definitely not the least by any measure, I would like to acknowledge with deepest gratitude, support from my family. My parents have been a constant source of inspiration throughout my life. I would like to express my exceptional gratitude to my sister and brother, Sepideh and Amir, for their continuous and loving support. I am indebted to my husband, Sina, who supported my research with his patience and of course for his knowledge on the fluid mechanics. I would like to thank my son, Kian, who brought shine, joy and motivation to my life.

RÉSUMÉ

Les surfaces portantes. telles que des pâles, ailes, et hydrofoil sont sujets à des instabilités comme la divergence, le battement et la résonnance qui peuvent provoquer la fatigue de la structure et réduire sa tenue en service. Par conséquent, il est important de comprendre et de prédire avec précision la réponse et la stabilité de telles structures afin d'en assurer la sécurité, et de faciliter la conception et optimisation de concepts nouveaux et existants.

L'interaction entre un écoulement et une structure, nommée interaction fluide-structure (IFS), doit être prise en compte lors de l'étude la réponse élastique et des instabilités de surfaces portantes. Pour de telles applications, l'écoulement et la structure sont couplés au travers de la charge qui s'exerce sur la structure par le fluide, et la déformation qui en découle. Pour certaines applications IFS, le fluide et le solide peuvent être couplés par un transfert uni-directionnel de la charge. Dans ce cas, un champ donné peut fortement affecter l'autre sans l'être lui même. Cependant, pour certaines applications en ingénierie, où il y a une relation forte et potentielement nonlinéaire entre ces champs, un couplage uni-directionnel n'est pas adéquat. Alors, les déplacements de la structure causés par l'écoulement accentuent les forces du fluide de telle sorte que le fuide et la structure intéragissent en boucle de facon complexe. Donc, une analyse bi-directionnelle doit être entreprise.

Les structure légères et flexibles sont courament utilisées grâce aux avancées récentes dans les technologies des matériaux afin d'améliorer les caractéristiques hydrodynamiques et structurelles par rapport aux matériaux lourds et rigides. Dans cette thèse, on cherche une meilleure compréhension de la phénomènologie hydroélastique d'hydrofoils hautement flexibles, qui subissent de grandes déformations sous de fortes charges. Ceci milite en faveur d'une méthodologie IFS bi-directionnelle fortement couplée, en plus de l'incorporation de techniques numériques avancées pour la modélisation de la déformation de maillages adaptés.

Pour des nombres de Reynolds moyens à élevés, le dévelopement d'un écoulement turbulent autour de l'hydrofoil provoque un transfert du mouvement perpendiculaire à la paroi et permet à l'écoulement de se re-attacher, et ainsi former une bulle laminaire de séparation (Laminar Separation Bubble, LSB). Le décrochage de l'écoulement, la formation de tourbillons dans le sillage, la localisation et le mouvement de la bulle laminaire sont tous des phénomènes qui affectent les charges hydrodynamiques et les vibrations de la structure. Par conséquent, une méthodologie numérique avancée, avec une précision spatiale suffisamenent élevée a été incorporée dans ce travail pour capturer finement ces phénomènes à l'interface

fluide-structure, tels que l'apparition et l'étendue de la zone de séparation.

L'interaction entre la surface portante et l'écoulement environnant implique d'importantes caractéristiques tri-dimensionnelles qui ne seront pas négligées dans cette thèse. Par exemple, les effets visqueux, la séparation, le sillage et le décrochage de tourbillons dont les effets directs ont été démontrés pour établir les charges hydrodymaniques, sont à l'origine de tels effets tri-dimensionnels qui doivent être pris en compte pour améliorer la précision de la modélisation d'écoulements turbulents. À cause de la déformation due au flèchissement et à la torsion de la surface, la charge hydrodynamique n'est pas uniforme dans la direction de l'envergure. En particulier, pour une surface portante flexible soumise à des écoulements à grandes vitesses et incidences élevées, la déformation élastique est importante, et par conséquent, ces caractéristiques tri-dimensionnelles ne peuvent plus être négligées.

Dans cette thèse, on propose une méthodologie avancée d'interaction fluide-structure bi-directionnelle fortement couplée pour étudier la réponse hydro-élastique de surfaces portantes légères et flexibles, et tri-dimensionnelles, dans des écoulements visqueux à des nombres de Reynolds moyens à élevés. Le problème de l'interaction fluide-structure est résolu par un logiciel de résolution numérique par volumes finis pour la partie fluide, CFX, et un code d'éléments finis, ANSYS, pour la partie solide du domaine. Au cours des simulations fortement couplées, les résoluteurs fluide et solide exécutent une suite d'étapes multi-champs, chacune comprenant un ou plusieurs couplages itératifs.

Le résoluteur fluide visqueux et le résoluteur IFS couplé sont tous deux validés par des comparaisons avec des résultats numériques et des mesures expérimentales. Pour quantifier les effets IFS, l'étude porte sur des hydrofoils rigides (en acier inoxydable) et flexibles (Polyacetate POM) avec la même géométrie non-déformée. La déformation due à l'écoulement ainsi que la réponse élastique de ces structures sous plusieurs conditions (vitesses amont, angles d'incidence) pour des nombres de Reynolds moyens à élevés, sont étudiées.

ABSTRACT

Lifting bodies, such as blades, wings, and hydrofoils, may be subject to instabilities, such as divergence, flutter, and resonance, which can fatigue the structure and reduce its operational longevity. Therefore, it is important to understand and accurately predict the response and stability of such structures to ensure their structural safety and facilitate the design and optimization of new and existing concepts.

The interaction between fluid and structure, known as Fluid-Structure Interaction (FSI), should be taken into account in the study of elastic response and instabilities of flexible lifting bodies. In such applications, the fluid flow and structure are coupled through the loads exerted on the structure by the fluid, which results in the the structural deformation. In some FSI applications, fluid and solid can be coupled by one-way (unidirectional) load transfer. In this case, a given field may strongly affect, but not be affected significantly by the other field. However, for some practical engineering applications, in which there is a strong and potentially nonlinear relationship between the fields, one-way coupling is not adequate. In such cases, the structural displacement caused by the flow further enhances the fluid forces in such a way that both fluid and structure are interacting in a complex feedback fashion. Hence, two-way FSI analysis needs to be undertaken.

Light-weight, flexible structures are widely used through recent advances in material technologies to improve hydrodynamic and structural performance compared to heavy and stiff materials. This project seeks to gain greater insight into the hydroelastic response of highly flexible hydrofoils, which undergo large deformation when subjected to high hydrodynamic loadings. This increases the necessity of incorporating strongly-coupled two-way FSI methodology in addition to the numerical challenges in mesh deformation modelling.

At moderate to high Reynolds numbers, the development of turbulent flow around a hydrofoil causes a momentum transfer normal to the wall and allows the flow to re-attach, and form a Laminar Separation Bubble (LSB). Flow separation, formation of trailing edge vortices, location and movement of the LSB affect the hydrodynamic loading and structural vibration. Hence, an advanced numerical technique with sufficiently high spatial accuracy is incorporated in the present study to precisely capture these local interface phenomena, such as the onset and the amount of flow separation.

The interaction between the foil and surrounding flow involve significant three-dimensional features that will not be neglected in the present study. For instance, the viscous effects, separation, wakes and vortex shedding, which have been shown to have immediate effects

in determination of hydrodynamic loads on hydofoils, have significant 3D features that have to be accounted for to improve the accuracy of turbulent modelling. Due to the bending and twist deformation of the foil, the hydrodynamic loading is not uniform along the span-wise direction. Particularly, for a flexible foil subjected to high flow velocities at hich angles of attacks, the elastic deformation is significant and hence, these 3D features cannot be neglected.

This PhD project proposes an advanced strongly-coupled two-way fluid-structure interaction methodology to investigate hydroelastic response of three-dimensional lightweight flexible hydrofoils in viscous flow at moderate to high Reynolds number. The fluid-structure problem is solved with a finite volume-based code for the fluid domain, CFX, and a finite element-based code, ANSYS, for the structural domain. During the strongly-coupled simulations, the fluid and structural solvers execute the simulation through a sequence of multifield steps, each of which consists of one or more coupling iterations.

The viscous fluid solver and the coupled FSI solver are both validated by comparing the numerical results with measured experimental data. To quantify the FSI effects, rigid (stainless steel) and flexible (POM Polyacetate) hydrofoils with the same undeformed geometry are simulated and compared. The flow-induced deformation and elastic response of those structures at various operating conditions, i.e. inlet velocities and angles of attack, subjected to moderate to high Reynolds number flows will be studied.

TABLE OF CONTENTS

LIST OF TABLES

LIST OF FIGURES

LIST OF APPENDICES

CHAPTER 1 INTRODUCTION

1.1 Motivation

Aeroelastic/hydroelastic behaviour of flexible lifting bodies, such as propulsors, blades and wings, is a very active area of research in the fields of aero/hydrodynamics, structural dynamics, and acoustics. From the fluid dynamics point of view, the dynamic loading on a blade, for instance, is affected by the motion of the blade, as given in classic texts such as aeroelastic theory by Theodorsen (Theodorsen, 1935). This unsteady loading causes time-dependent lift and drag forces that can lead to instabilities if not carefully controlled (Chae et al., 2013; Liaghat et al., 2014; Ducoin and Young, 2013). Structurally, these uncontrolled static or dynamic instabilities can lead to vibration, noise issues, excessive deformation, accelerated fatigue, and even catastrophic structural failures (Coutu et al., 2004, 2005, 2007; Seeley et al., 2012; Thapa et al., 2012; Liaghat et al., 2014). Structural vibration causes acoustic wave propagation in the fluid domain that can travel into the far-field and cause structural damage given enough energy (Reese, 2010). An important step towards the prediction of such structural damage consists in studying and precisely predicting material response to ensure the structural safety and to facilitate the design/optimization of new/existing structures.

In the majority of earlier studies on the interaction between flexible lifting bodies and the surrounding flows, the focus has been on aerospace or wind energy applications, in which fluid damping and inertia have a limited effect on the solid. However, in the interaction between fluid and hydraulic turbines or marine propeller blades for instance, the influence of fluid inertia and fluid damping can be much more important. In those cases, the fluid viscous effects can significantly affect and interact with the dynamic response of the structures and must be taken into account in the analysis and design of such equipments.

Hydroelasticity

Hydroelasticity is the term used to denote the field of study concerned with the interaction between the change in shape of a deformable structure subjected to a fluid flow and the resulting hydrodynamic forces.

The interdisciplinary nature of the field is illustrated in Fig. 1.1 which represents the relationships between the three disciplines of hydrodynamics, dynamics and elasticity, i.e. each circle represents a field of study related to hydroelasticity. The classical hydrodynamic theories, adapted from aerodynamics (Hodges and Pierce, 2004; Harwood et al., 2016), provide a

prediction of the forces acting on a structure of a given shape. Elasticity provides a prediction of the shape of a deformable structure under a given load. Dynamics describes the effects of inertial forces.

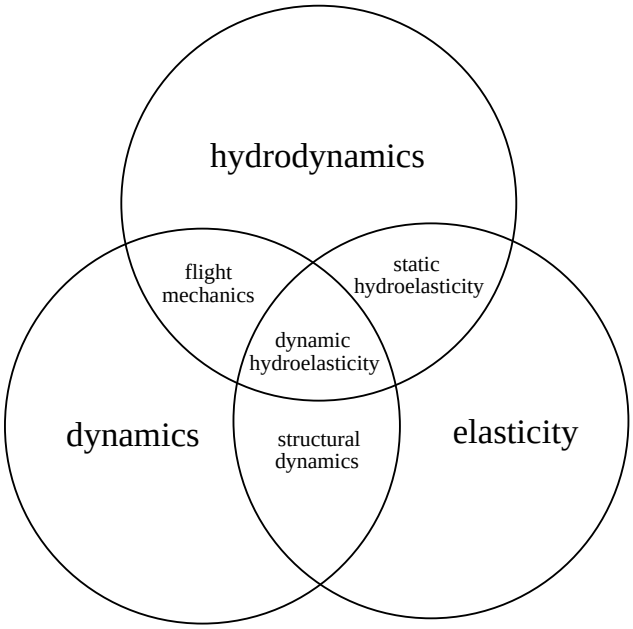

Figure 1.1 Schematic of the field of hydroelasticity (from (Hodges and Pierce, 2004) adapted to hydroelasticity)

The areas where these circles overlap represent the interaction between the relevent domains of study (Hutchison, 2012). Overlap between:

- elasticity and dynamics subfields represents structural dynamics;
- fluid dynamics and dynamics represents flight mechanics;
- fluid dynamics and elasticity represents static hydroelasticity, in which the inertial forces have little effect; and,
- all the three subfields represents dynamic hydroelasticity, in which the inertial forces become more significant and phenomena such as flutter can occur.

It is not always easy to distinguish between static and dynamic hydroelasticity as the change can be dictated by the point at which the inertial interaction becomes significant, and may cause instability in the system dynamics (Hutchison, 2012). Hydroelasticity can be considered as the analysis of time-dependent interaction of hydrodynamic and elastic structural forces.

Fluid-Structure Interaction

Fluid–Structure Interaction (FSI) is a broad term spanning many engineering applications, but generally denotes the bidirectional energy transfer in a domain consisting of both fluid and structure (Liaghat et al., 2014). From both theoretical and practical points of view, the complex interaction between flow and structure, known as fluid–structure interaction, must be taken into account in the study of the elastic response and instabilities of flexible lifting bodies. In such applications, the fluid flow and structure are coupled through the force exerted on the structure by the fluid, which results in the structure deformation leading to a change of its orientation to the flow. The orientation and velocity of the structure relative to the fluid flow determines the fluid forces that will be exerted on the structure in a feedback system.

At the boundary between fluid and structure, known as the fluid-structure interface, information for the solution is shared between the fluid and structural solvers. The information exchanged is dependent on the coupling method. In a one-way coupling, it is assumed that one domain is driven by the other, with the driven domain having no feedback effect on the driving domain. This method, however, is not always adequate for practical engineering applications, in which the structural displacement caused by the flow further enhances the fluid forces in such a way that both fluid and structure are interacting in a complex feedback fashion. In such cases, two-way FSI analysis needs to be undertaken. Numerically, weak coupling methods are explicit and hence, suffer from possible instabilities. Strong coupling methods, in which equilibrium is satisfied jointly between fluid and structure in each time step, provide better fidelity. To the best of our knowledge, most of the numerical studies on flow over hydrofoils thus far have focused primarily on problems with weak FSI. In the present study, a strongly coupled two-way FSI methodology will be presented to tackle the large flow-induced deformation and accurately simulate the subsequent complex flow phenomena.

Through recent advances in material technologies, it is possible to take advantage of lightweight, flexible hydrofoils to improve hydrodynamic and structural performance. Physical material properties of the structure (density, Young's modulus and Poisson's ratio) are important factors in determination of the elastic deformation and, hence, have immediate effect on how strongly the fluid and structure are coupled in the FSI simulation. Physically, under a specified hydrodynamic loading, a more flexible structure undergoes larger deformation. Such a large deformation requires a two-way coupling method, which leads to additional challenges in mesh deformation modelling. To the best of our knowledge, most of the former studies on the dynamic response of hydrofoils thus far involved hydrofoils made of relatively heavy and stiff materials, such as lead, stainless steel and aluminium. In the present study, a highly

flexible hydrofoil will be studied.

The interaction between the hydrofoil and the surrounding flow involves significant three-dimensional features, such as separation, wakes and vortex shedding, that have been shown to have immediate effects in the determination of hydrodynamic loads on hydofoils. Due to the bending and twist deformation of the foil, the hydrodynamic loading is not uniform along the span-wise direction. Particularly, for a flexible foil subjected to high flow velocities at high angles of attacks, the elastic deformation is significant and hence, these 3D features cannot be neglected. Most of the previous studies on the hydroelastic response of hydrofoils have focused mainly on 2D simulations, where the 3D features are neglected. In the present study, we will emphasize these 3D features.

1.2 Research goal

Even though several numerical techniques have been developed to simulate fluid-structure interaction of hydrofoils and provide precise prediction of their hydroelastic response, there still remain some issues that require further investigation. Special care must be taken for the multiphysics nature of the problem which requires implementation of proper numerical techniques for capturing both the global hydroelastic response, and also very local phenomena at the interface, such as development and movement of Laminar Separation Bubble (LSB) that has been shown to have immediate effects on the hydroelastic response of the structure.

The goal of this research is to develop an advanced strongly-coupled two-way fluid-structure interaction methodology with sufficiently high spatial accuracy to investigate hydroelastic response of a three-dimensional lightweight flexible hydrofoil in viscous flows. The flow-induced deformation and elastic response of those structures at various operating conditions, i.e. inlet velocities and angles of attack, subjected to moderate to high Reynolds number flows will be studied.

1.3 Thesis overview and organization

Following the present introduction, Chapter 2 provides a literature review on FSI response and stability of hydrofoils. This chapter will provide the context for additional research in the field of hydroelasticty at high Reynolds number flows and presents the different numerical methods to study fluid-structure interaction along with their advantages and drawbacks according to the literature. Furthermore, this chapter will illustrate the lack of an adequate account of three-dimensional features in this field. In Chapter 3, the fundamental concepts of fluid and solid mechanics as a necessary background for the fluid-structure analysis are

reviewed. This chapter includes a brief theoretical description of numerical modelling of FSI and the governing equations for the fluid and the structural domain. The test cases used for validation of the proposed methodology will be described in Chapter 4. The numerical modeling, including the fluid and solid models, meshes and boundary conditions are described in this chapter. In chapter 5, the proposed methodology will be presented. Chapter 6 provides a general discussion about the results. Finally, Chapter 7 presents the conclusion and contributions of the thesis followed by recommendations for future studies.

CHAPTER 2 LITERATURE REVIEW

In this chapter, we aim to provide a literature review to situate our research topic in relation to previous studies and present the current state of the art, upon which our study will build.

First, the instability modes of a structure subjected to different fluid flows will be presented. The effects of fluid viscosity along with the limitation of previous studies in the field of hydroelasticity will also be explained to situate the contribution of this work, which is the study of hydroelasticity at high Reynolds number flows. Fluid-structure interaction, the relevant previous studies as well as the different solution methods will next be presented. The advantages and drawbacks of those methods will also be discussed to highlight that the two-way coupling method used in this study is better suited for the FSI analysis of flexible hydrofoils. Furthermore, the necessity of performing 3D analysis, which is the contribution of the present study, rather than previous 2D studies will be highlighted. Finally, the objectives of the present study will be outlined.

It should be noted that we will focus on the numerical techniques that are especially useful for FSI problems with very small length and time scales, for which it is diffcult to perform high resolution experimental studies in detail.

2.1 Physical instability modes

Flexible lifting bodies, such as blades, wings, and hydrofoils, may be subject to instabilities such as divergence, flutter, resonance, etc. (Ducoin and Young, 2013; Chae et al., 2013), which are almost always undesireable. These instabilities can fatigue the structure and reduce its operational longevity and, hence, have to be studied and precisely predicted.

Divergence is one of the most common physical instability modes that cause a system to fail due to excessive deformation and/or material failure. Both static and dynamic divergence may be observed. Static divergence occurs when the deflection induced by the fluid load increases with time without oscillations. It is caused by the loss of the effective torsional stiffness, which occurs when the fluid disturbing moment exceeds the structure's twist capacity (Ducoin and Young, 2013). In dynamic divergence, the mean deformation also increases with time. However, it has an oscillation frequency, which decays with increasing deformation (Chae et al., 2013). In the studies of Bendiksen (Bendiksen, 1992, 2002) it was shown how dynamic divergence can lead to accelerated fatigue and structural failure. Chae et al. (Chae et al., 2013) showed that dynamic divergence cannot be predicted with linear

frequency domain methods because it is a nonlinear instability mode where the oscillation frequency changes with time.

Airfoils/hydrofoils at high angles of attack experience the well-known phenomenon of stall. This occurs when the critical angle of attack of the foil is exceeded, where separated flow is so dominant that additional increases in angle of attack produce less lift and more drag (Clancy, 1975). This phenomenon can occur in the form of a light or massive stall. In the case of a light stall, the vortex developed from the foil's trailing edge moves toward the foil's leading edge (Fig. 2.1), which reduces the slope of the lift curve, $dC_L/d\alpha$ (where C_L is the lift coefficient and α is the effective angle of attack), and also increases the drag (Rhie and Chow, 1983; Clancy, 1975). When massive stall occurs, periodic shedding of a leading edge vortex may be observed, which creates large load fluctuations, significant lift decrease such that the slope of the lift curve becomes negative (Lee and Gerontakos, 2004), and significant increase in drag. The periodic shedding of the vortices induced by stall may also lead to flutter or resonance (Ducoin and Young, 2013).

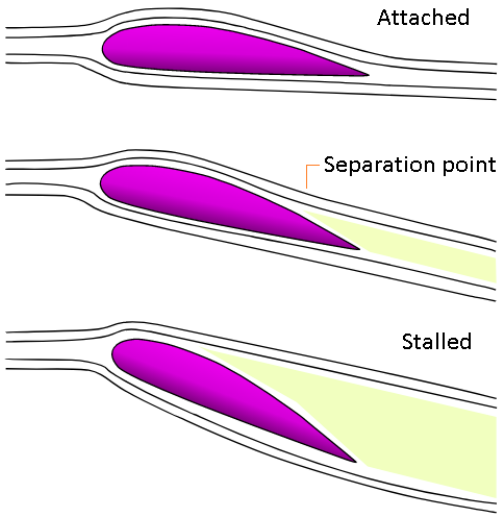

Figure 2.1 Flow separating from a foil and stall at high angles of attack (Wikipedia, 2018)

Flutter is defined as a dynamic self-excited aeroelastic/hydroelastic instability of a structure in steady, uniform inflow (i.e. flow that is steady in absence of the structure) (Ducoin and Young, 2013). In this case, the flow-induced deformations oscillate with a fixed frequency. Poirel et al. (Poirel et al., 2008) and Poirel and Yuan (Poirel and Yuan, 2010) showed that flutter can be caused by unsteady bursting of a laminar separation bubble and/or unsteady vortex shedding.

Resonance is an externally-excited dynamic instability caused by an externally applied load or

by spatially/temporally varying inflow (Ducoin and Young, 2013). It accounts for unexpected vibrations with large amplitudes that can accelerate fatigue and lead to detrimental failure (Visbal et al., 2009; Young and Savander, 2011).

2.2 Viscous effects

Although the above-mentioned instability modes have received much attention in recent years, most of the analytical and numerical studies thus far have focused on inviscid flows due to interest driven by aerospace or wind turbine applications. Nevertheless, these physical instabilities can also occur in hydraulic turbines or marine propeller blades in which the effects of loads exerted from dense fluids such as water are significant on flexible structures. Due to the lower operating speed, the Reynolds number associated with such structures is typically lower than occuring in aerospace systems, leading to enhanced viscous effects. The enhanced fluid inertial and viscous effects associated with flow separations and vorticity in hydroelasticity might result in nonlinear FSI responses and can significantly modify the hydroelastic stability boundaries (Chae et al., 2013, 2017; Ward et al., 2018).

As previously mentioned, in most of the earlier works on elastic response of flexible bodies, the effects of fluid inertia or damping forces are often ignored. In the studies of Theodorsen (Theodorsen, 1935), Sears(Sears, 1941), and Garrick(Garrick, 1946) linear potential theory was used to obtain analytical expressions for the aerodynamic lift and moment of 2-D thin airfoils undergoing small amplitude oscillations in uniform inflow. Theodorsen's (Theodorsen, 1935) approach assumed that: 1) the total lift force acts at the aerodynamic center (a quarter-chord downstream from the foil's leading-edge; and 2) the wake behind the foil consists of shed vortices from the trailing-edge that convect downstream in a direction parallel to the inflow without any dissipation, at a fixed frequency. However, the real wake patterns shown in the studies of Anderson et al. (Anderson et al., 1998) and Munch et al.(Munch et al., 2010) are typically more complex than the wake patterns assumed in linear potential theory. The former author experimentally studied the wake patterns of a NACA0012 foil in a water tank for different flow regimes and observed a wavy wake without distinct vortices and with a very weak leading-edge vortex. Munch et al. (Munch et al., 2010) conducted numerical and experimental studies on a NACA0009 hydrofoil and showed that the pattern and strength of the wakes depend on the the reduced frequency of the oscillation motion, as depicted in Fig. 2.2.

Linear potential flow theory has been shown to be inadequate for modeling FSI problems with strong viscous effects. Connell and Yue (Connell and Yue, 2007) and Akcabay and Young (Akcabay and Young, 2012) numerically studied the dynamic response and stability

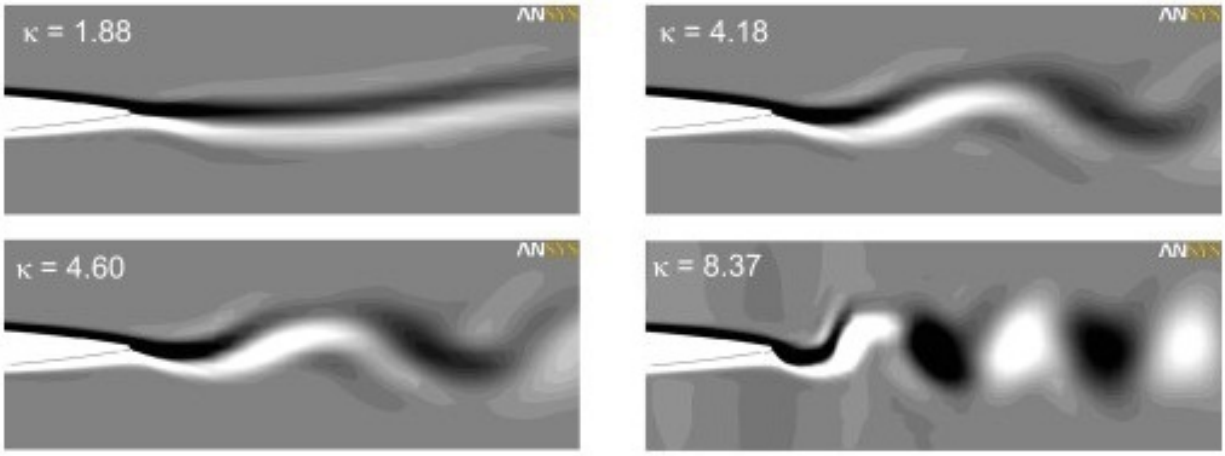

Figure 2.2 The wake pattern of a NACA0009 hydrofoil for four values of the reduced frequency, κ, (Munch et al., 2010)

of cantilever beams in viscous and axial flows. The latter authors validated their numerical results with several experimental data and showed that viscous effects are more significant for light beams in dense fluids due to the increased relative contribution of the fluid forces. They also found that fluid viscosity affects flutter of the structure, reduces the vibration amplitude, and changes the oscillation modes. More recently, Akcabay and Young (Akcabay and Young, 2014) compared their viscous simulation results with the predictions from the quasi-steady inviscid linear potential flow based theory. They concluded that the observed differences between results could be attributed to viscous effects, e.g. thickening of boundary layers, formation of trailing edge vortices, and flow separation. Considering the viscous effects, Ducoin and Young (Ducoin and Young, 2013) calculated the static divergence speed of a spanwise flexible cantilevered hydrofoil and showed that viscous effects help suppress or delay divergence.

The fluid damping and disturbing forces also depend on the flow velocity (Theodorsen, 1935; Sears, 1941; Liaghat, 2014). Reese (Reese, 2010) showed that the resonance frequencies and total loss factors of flexible hydrofoils depend on the flow velocity. This study involved hydrofoils made of relatively heavy and stiff materials for a limited range of flow velocity, and hence showed only a small dependence on the flow velocity.

In addition to the effects of velocity on the structural response, which is intuitively apparent, Reynolds number and angle of attack are also expected to affect the oscillations. Huang and Lin (Huang and Lin, 1995) and Jung and Park (Jung and Park, 2005) studied the unsteady characteristics of vortex shedding in the near wake of an oscillating foil for low Reynold numbers, $Re \leq 2.7 \times 10^4$, and showed that the vortex shedding frequency varies with the

angle of incidence.

Boundary layer flows can be transitional around a lifting body at moderate Reynolds numbers. The development of turbulent flow, which causes a momentum transfer normal to the wall, allows the flow to re-attach, and form a Laminar Separation Bubble (LSB). Flow separation, formation of trailing edge vortices, location and movement of the LSB affect the hydrodynamic loading and vibration of a flexible hydrofoil, which is the topic problem studied in this thesis. Hence, the precise prediction of the onset and the amount of flow separation plays a key role in the determination of the hydrodynamic loads on hydrofoils. Ducoin et al. (Ducoin et al., 2012a) experimentally investigated fluid structure interaction on a flexible hydrofoil in various flow regimes and concluded that the structural vibrations are induced by the laminar to turbulent boundary layer transition and depend on the vortex shedding frequency. Ducoin et al. (Ducoin et al., 2009a) showed that the LSB first appears near the trailing edge for low to moderate angles of attack, and as this is increased, it moves towards the leading edge. It was shown in the studies of Poirel et al. (Poirel et al., 2008) and Ducoin et al. (Ducoin et al., 2012b) that this movement of the LSB affects the hydrodynamic loading and vibration of a flexible hydrofoil. Poirel and Yuan (Poirel and Yuan, 2010) studied the laminar separation at transitional Reynolds numbers, $5.0 \times 10^4 \leq Re \leq 1.3 \times 10^5$ and showed that the laminar separation can lead to flutter.

Summary

To recapitulate, the viscous effects, such as flow separation and vortices, have immediate effect on the hydrodynamic loads and response of hydrofoils. Furthermore, in the determination of hydroelastic response of flexible hydrofoils, it is crucial to precisely predict the onset and the amount of flow separation. This is particularly the case for high Reynolds number flows, in which the change of the wake pattern and vortex shedding frequency is substancially more noticeable. However, very limited studies are available for flexible hydrofoils at high Reynolds number flows.

In the present study, the hydroelastic response of hydrofoils subjected to moderate to high Reynolds number flows will be investigated.

2.3 Fluid-structure interaction

Fluid-structure interaction is a multiphysics phenomenon where the interaction between fluid flow and structural mechanics is taken into account. FSI is characterized by interactions, which can be stable or oscillatory, between a moving or deformable solid structure and a

surrounding or internal fluid flow. These effects cannot be neglected when evaluating the elastic response of lightweight flexible bodies due to the strong interplay between the body deformations and load distributions (Ward et al., 2018). This is a consequence of the high hydrodynamic load, which is proportional to the density of fluid. For instance, the density of water is approximately three orders of magnitude greater than that of air. Hence, a lifting body operating in water will experience much higher loads and resulting amplified FSI effects than a geometrically identical body in air at the same operating conditions (Harwood et al., 2016; Ward et al., 2018).

As evidenced from these studies, FSI problems play prominent roles in many engineering and scientific applications, yet, due to their strong nonlinearity and multidisciplinary nature, a comprehensive study of such problems remains a challenge (Hou et al., 2012). Different methods for the investigation of fluid–structure coupling have been extensively investigated (Tran et al., 2005; Dowell and Hall, 2001).

The FSI analyses can be generally categorized into two approaches; monolithic and partitioned methods. In monolithic approaches, both sub-fields (fluid and solid) are combined as one single problem. The non-linear, discrete system of equations resulting from the discretization of the governing equations are solved as a whole (Barker and Cai, 2010; Gee, 2011). Ryzhakov et al. (Ryzhakov et al., 2010) presented a monolithic method for the simulation of the interaction between flexible structures and free surface flows and showed that their method was robust. However, this method leads to ill-conditioned system due to the different scaling of variables in the multi-field problem (velocity, displacement, pressure) (Ryzhakov et al., 2010) and might be very challenging to implement (Wu et al., 2015) and computationally expensive (Raja, 2012).

In contrast, the computational fluid dynamics (CFD) and computational structure dynamics (CSD) solvers can be coupled in a partitioned way. In this approach, which will be incorporated in this study, the fluid and solid parts are solved using their distinct numerical methods. Interaction takes place regularly between the fluid and structure solvers via the coupling scheme which is based on successive solutions produced by the two solvers (Wu et al., 2015; Lefrançois, 2017). In an industrial context, the most important advantage that a partitioned approach offsets over a monolithic coupling approach (with a single solver) is the modularity of the coupling method, which makes the different solvers much easier to implement (Ryzhakov et al., 2010) and allows distributed computation (Lefrançois, 2017).

Partitioned approaches can be categorized into two types: the loose coupling approach and the strong coupling approach. In a loosely coupled approach, only one single computation per time step is performed for each field (Lefrançois, 2017; Akcabay et al., 2017). Hence,

the coupling conditions at the interface may not be satisfied accurately (Sotiropoulos and Yang, 2014). Furthermore, loosely coupled (LC) partitioned FSI solvers suffer from numerical instabilities (Sotiropoulos and Yang, 2014), as each of the solid and fluid solvers can only use the other's solution explicitly. This time-delay in the exchange of the boundary conditions (surface tractions and displacements) between the fluid and solid solvers can lead to errors, specially for FSI problems with lightweight structures in dense, incompressible flow (such as water); i.e. problems with low solid-to-fluid density ratios (Akcabay et al., 2017).

In order to avoid this numerical instability, strongly coupled partitioned algorithms with an iterative procedure are developed to improve the accuracy of the satisfaction of coupling conditions (Sotiropoulos and Yang, 2014; Lefrançois, 2017).

Two of the most common terms used when referring to the type of FSI analyses are one-way (unidirectional) and two-way (bidirectional). These terms reflect how the loads and displacements are transferred between the two domains. When fluid and solid are coupled by unidirectional load transfer, a given field may strongly affect, but not be affected significantly by the other field (Reference: ANSYS User Guide). When solving a one-way FSI problem, flow and structure are modeled within separate domains. The resultant loads from the flow field are then used to calculate the structural deflection (Liaghat et al., 2014), or the displacement of the structure can be used to update the boundary conditions and solve the flow field. In some Fluid-Structure Interaction simulations, however, there is a strong and potentially nonlinear relationship between the fields that are coupled. This is often the case in situations where the structure undergoes large amplitude deflections (Liaghat et al., 2014). Under these conditions, which is the case in many engineering applications, two-way FSI is required. Benra et al. (Benra et al., 2011) compared the one-way and two-way coupling methods for numerical analysis of fluid-structure interactions and showed that the results of two-way coupling methods were more accurate, especially for larger deflections where the fluid field is strongly influenced by structural deformation. They showed that a one-way coupling algorithm gives plausible results only for specific values in some cases, and does not guarantee energy conservation at the interface (Benra et al., 2011).

Matthies and Steindorf (Matthies and Steindorf, 2003) found that the weak coupling methods are explicit and hence, suffer from possible instabilities. They proposed a partitioned method to compute the transient response and showed that their method was faster, both in the number of iterations and in the overall numerical effort. In addition, it was shown to have superior convergence characteristics, and they concluded that strong coupling methods, where equilibrium is satisfied jointly between fluid and structure at each time step, are better suited.

The hydroelastic coupling method of Young and Kinnas (Young and Kinnas, 2003a,b) as-

sumed small blade deformations. Applying Bernoulli's equation, the total pressure was expressed in terms of the rigid and elastic blade components, with the change in load stiffness and damping matrices. Coupling of the hydrodynamics with a structural analysis model to include the effect of blade vibration is described in (Young and Kinnas, 2004). Young (Young, 2007, 2008) analyzed time-dependent FSI of a propeller using a one-way approach by developing a 3-D potential-based boundary element method coupled with a 3-D finite element method. Their predicted blade tip deflections, cavitation inception coefficient values, as well as cavitation patterns agreed well with experimental measurements.

Carstens et al. (Carstens et al., 2003) developed a coupled fluid-structure interaction algorithm to study the aeroelastic behaviour of vibrating blade assemblies. In their study, the motion of fluid and structure were integrated in time by separate time integration methods while their interaction was accounted for through a coupling algorithm. However, to reduce the immense computational effort of a full-scale calculation, simplified structural and aerodynamic models were taken for the computations.

Moffatt and He (Moffatt and He, 2005) performed an evaluation on the use of coupled and decoupled methods for various turbomachinery applications. They predicted the resonant forced response of turbomachinery blades using a fully coupled approach and expected that, by combining the aerodynamic forcing and damping calculations in a single analysis, a higher computational efficiency would result compared to a classical uncoupled approach. Blade vibration in their coupled approach was modelled with a single degree-of-freedom (DoF) modal equation on the CFD mesh and solved simultaneously with the flow equations. The modal equation was solved and directly coupled with the flow equations at each solution step.

Ducoin et al. (Ducoin et al., 2009b) incorporated a numerical one-way approach to analyze a deformable hydrofoil with transient pitching motion with a CFD finite volume code (CFX) for the fluid and a CSD finite element code (ANSYS) for the structure. Although there was good agreement with the experiments for the maximum displacement of the hydrofoil at low pitching velocities, for the highest pitching velocity, the simulation showed a stronger hysteresis effect than the experiment.

In the study of Munch et al. (Munch et al., 2010) a model was proposed to predict fluid–structure coupling by linearizing the hydrodynamic load acting on a rigid, oscillating NACA0009 hydrofoil subjected to a turbulent, incompressible flow. The hydrofoil was modeled with forced and free pitching motions and the unsteady simulations of the flow were performed in ANSYS CFX and validated experimentally. Their proposed model could predict fluid–structure coupling with good precision when the response of the system was linearized. Their method was validated for limited values of the motion amplitude.

Ducoin and Young (Ducoin and Young, 2013) and Akcabay et al. (Akcabay et al., 2014) studied the hydroelastic response of two-dimensional flexible hydrofoils in viscous flows. Their numerical approach was based on a simple 2-DOF system (mass-spring-damper) to simulate the chordwise rigid hydrofoil which undergoes bend and twist deformations only, as shown in Fig. 2.3. In their study, the fluid and structure solvers were coupled using the Loose Hybrid Coupled (LHC) method presented in (Chae et al., 2013) and (Young et al., 2012). The LHC method is a partitioned FSI method, as it couples the solutions of the two separate fluid and structure solvers. The 2-DOF solid model in Refs. (Ducoin and Young, 2013) and (Akcabay et al., 2014) was used to calculate the hydrofoil motion at each time step. The fluid forces were extracted and applied on the 2-DOF model and solved for the new position of the hydrofoil within each time step. Ducoin and Young (Ducoin and Young, 2013) compared the predicted and measured lift coefficient and tip section displacement. Some discrepancies between experimental and numerical results were observed, which might be partly due to the 2-D flow assumption in their research, which ignored 3-D effects such as boundary layer effects, induced drag, and the use of a generalized 3-D structural model in their numerical framework. In their studies, LHC approach does not iterate within each time step and that is why the coupling between fluid and structure is loose in their simulations.

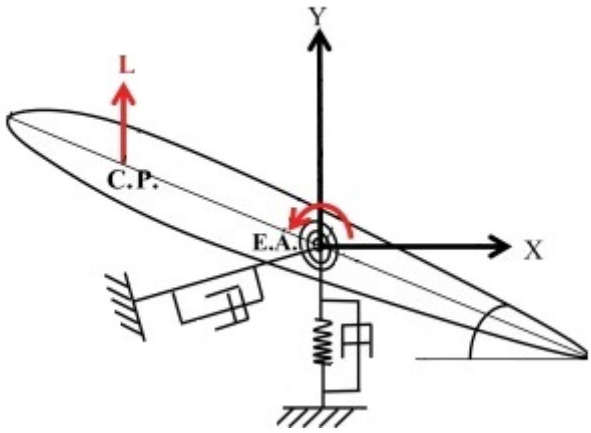

Figure 2.3 Dynamics of a 2D hydrofoil cross section with two DOF (Ducoin and Young, 2013)

Sotiropoulos and Yang (Sotiropoulos and Yang, 2014) presented an immersed boundary method to simulate complex fluid–structure interaction problems in engineering and biology. This method has emerged as a powerful numerical approach due to its inherent ability to handle arbitrarily complex domains with arbitrarily complex deformable immersed boundaries without the need for expensive and cumbersome dynamic re-meshing strategies or construct grids that conform to and deform with solid boundaries. However, a major disadvantage

of this method is the limitation in its ability to selectively cluster grid nodes in the vicinity of solid boundaries, which results in difficulties in simulations of high Reynolds number turbulent flows.

The major drawback of the classical partitioned FSI coupling scheme, according to (Lefrançois et al., 2016; Lefrançois, 2017), is that where the structure is surrounded by high density fluid there will be strong effects of added mass. Under this condition, convergence is not always guaranteed, or may be slow. Divergence will generally be observed, regardless of the chosen time step (Lefrançois, 2017). In 2016, Lefrançois et al. (Lefrançois et al., 2016) presented a numerical model for fluid-structure interactions in the context of sloshing effects in movable, partially filled tanks. The purpose of this model was to counteract the penalizing impact of the added mass effect on classical partitioned FSI coupling schemes. Results show that the corrected version systematically ensures convergence in cases where the classical FSI scheme fails to converge. In the rare cases where convergence was already obtained, the corrected version was shown to significantly reduce the number of required iterations.

In 2017, Lefrançois (Lefrançois, 2017) presented a modified version of a partitioned FSI scheme for studying the dynamics of a NACA2412 foil flexibly attached and immersed in a heavy fluid. This work was based on an added mass corrected version of the classical strongly coupled partitioned scheme presented in (Song et al., 2013). The mathematical model for the structure in his study was limitted to the dynamics of a 2D foil that encountered only plunging and pitching motions ($\omega(t)$ and $\theta(t)$), as shown in Fig. 2.4. Whereas the classical scheme encountered an acceptable (no numerical oscillation) convergence limit for fluid with certain density values, the corrected scheme in the study of Lefrançois (Lefrançois, 2017) was not dependent on fluid density.

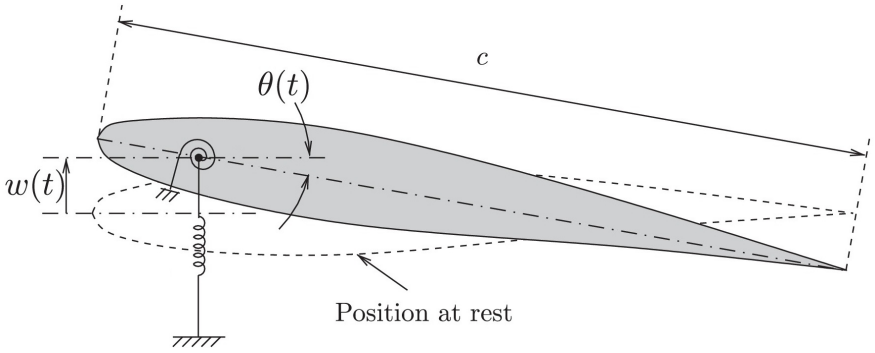

Figure 2.4 A two-degrees-of-freedom model representing plunging and pitching ($\omega(t)$ and $\theta(t)$) of a 2D hydrofoil (Lefrançois, 2017)

Chae et al. (Chae et al., 2017) studied the influence of the flow-induced bend–twist coupling

of hydrofoils by comparing the inviscid and viscous fluid–structure interaction simulation of cantilevered NACA0015 hydrofoils in water. They studied hydrofoils made of stainless steel, aluminium and polyacetate (POM) under attached flow conditions in fully turbulent regimes at low angles of attack, and incorporated the LHC method presented in the studies of Young et al. (Young et al., 2012), Chae et al. (Chae et al., 2013), and Akcabay et al. (Akcabay et al., 2014). The 3D effects were neglected in their FSI method and it was recently applied by Wu et al. (Wu et al., 2018) to investigate transient characteristics of cavitating flow over a flexible 2D hydrofoil via combined experimental and numerical studies. The hydrofoil in theses studies was presented with a chord-wise rigid, two degree of freedom model and the pitching and plunging motion of the tip section was considered as the corresponding twisting and bending deformation of the hydrofoil.

Akcabay et al. (Akcabay et al., 2017) examined the numerical stability behavior of the LHC method, incorporated in (Young et al., 2012; Chae et al., 2013; Akcabay et al., 2014), to solve partitioned fluid and solid solvers for FSI problems. They showed that the LHC method is capable of stable solution to FSI problems, even for the difficult cases with small solid-to-fluid density ratios.

To the best of our knowledge, most of the former studies on the dynamic response of hydrofoils involved hydrofoils made of relatively heavy and stiff materials (Seeley et al., 2012; Liaghat et al., 2014; Yao et al., 2014; Liaghat, 2014). Hutchison (Hutchison, 2012) studied FSI for hydrofoils made of stainless steel (E=193 GPa, ρ=7750 kg/m^3) and aluminium (E=71 GPa, ρ=2770 kg/m^3). The flexible hydrofoil in the study of Liaghat et al. (Liaghat et al., 2014; Liaghat, 2014) had a Young's modulus of E=193 GPa and a density of ρ=8000 kg/m^3. The increasing interest in the use of lightweight materials in the applications in which the solid-to-fluid density ratio is typically in the range of 1 and 2 (Chae et al., 2016), points to a better understanding of the elastic response and stability of lightweight lifting structures. These were investigated in Refs. (Ducoin and Young, 2013; Chae et al., 2013, 2016; Akcabay et al., 2014; Akcabay and Young, 2014).

Summary

Different methods for the solution of fluid-structure coupling have been extensively investigated in the literature. To study the hydroeastic behaviour of flexible hydrofoils, particularly at high hydrodynamic loadings, fluid and structure fields have strong and potentially nonlinear effects on each other. Hence, the solution method should be capable of strongly coupling and jointly satisfaction of equilibrium between fluid and structure. The two-way coupling method, which will be incorporated in the present study, is clearly required to tackle the large

structural deformations and subsequent effects on the flow fields, such as flow separation and instabilities. However, this method has not been recently used in this field. Recent increases in computer power coupled with advances in numerical methods, enable coupled two-way analyses of FSI in a reasonable time frame at an acceptable computational cost.

In addition, most of the hydrofoils studied in this field, have been made of relatively heavy and stiff materials. The present study will focus on highly flexible hydrofoils that undergo large deformation. As a consequence, the two-way FSI coupling is more challenging, particularly in the flow mesh deformation modelling.

2.4 Reasons for 3D simulation

In this dissertation, a two-way fluid-structure interaction (FSI) methodology is presented to study the hydroelastic response and stability of flexible hydrofoils with emphasis on three-dimensional features. This approach is validated by comparing the numerical results with measured experimental data by Akcabay et al. (Akcabay et al., 2014). To the best of our knowledge, despite the fact that the physics of the stated problem is 3D (as will be explained in what follows), most of the the previous studies on the hydroelastic response of hydrofoils have been restricted mainly to 2D simulations.

Experimentally and numerically, Chae et al. (Chae et al., 2016) investigated the natural flow-induced vibrations of flexible NACA0015 hydrofoils. The cantelivered hydrofoil in their study was clamped to the back wall of the test tunnel (foil root) and free to move on the other end of the test section wall (foil tip), as shown in Fig. 2.5. This set-up clearly illustrates the importance of 3D effects; i.e. the spanwise tip bending and twisting deformations of the flexible hydrofoil in their experiments. Due to these deformations, the hydrodynamic loading is not uniform in the spanwise direction. However, in their numerical simulation the flow was assumed to be two-dimesional.

The above mentioned cantilevered configuration of flexible hydrofoils have been studied in Refs. (Akcabay et al., 2014), (Akcabay and Young, 2014), (Ducoin and Young, 2013), (Wu et al., 2015), and (Chae et al., 2013). The hydrodynamic loading was assumed to be uniform over the spanwise direction in these studies. Despite the fact that the spanwise deformation will change the pressure distribution along that direction, they assumed that its effect on the foil deformation response is limited because of the small elastic deformation. However, for a flexible hydrofoil subjected to high flow velocities at high angles of attack, the elastic deformation is significant and cannot be neglected.

Due to the flow-induced deformations of the flexible hydroils along the spanwise direction,

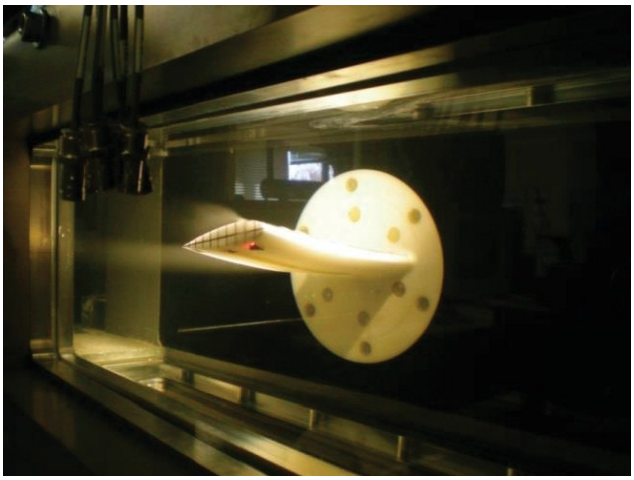

Figure 2.5 NACA0015 POM hydrofoil inside the tunnel (Chae et al., 2016)

such as bend and twist (as depicted in Fig. 2.5), the hydrodynamic loading is not uniform in the spanwise direction. For this reason, the interaction between hydrofoil and the surrounding flow has significant three-dimensional features that clearly should not be neglected. Furthermore, the flow is turbulent in the present study. It has been discussed in the previous sections that the flow separation and enhanced momentum exchange accompanied by the vortices induced by flow turbulence have a significant effect on the structural hydrodynamic response. Hence, the precise prediction of turbulence plays a key role in this area of research.

It is widely accepted that turbulence is a three-dimensional phenomenon (Nichols, 2010). Turbulent disturbances can be considered as a series of three-dimensional eddies of different sizes that are in interaction with each other (Nichols, 2010). One important phenomenon in turbulent flows is vortex stretching. This is the lengthening of vortices in the flow, associated with a corresponding increase of the component of vorticity in the stretching direction (Tennekes and Lumley, 1972). Vortex stretching is associated with a particular term in the vorticity dynamics equation:

$$\frac{D\vec{\omega}}{Dt} = (\vec{\omega} \cdot \vec{\nabla})\vec{v} + \nu\nabla^2\omega \tag{2.1}$$

where D/Dt is the material derivative, $\vec{v}$ is the velocity vector, ν is the fluid kinematic viscosity and ∇^2 is the Laplace operator. The first term on the right hand side describes the stretching or tilting of vorticity due to the flow velocity gradients. It amplifies the vorticity, $\vec{\omega}$, when the velocity diverges in the direction parallel to $\vec{\omega}$. This term has been shown to be zero in 2D formulation, and hence, 3D simulations are necessary to capture this important feature of turbulence.

Summary

The hydroelastic deformation of hydrofoil has significant 3D features that will be accounted for in the present study. Particularly, in the case of highly flexible hydrofoils which undergo large deformation, the 3D effects should not be neglected for the accurate prediction of the hydrodynamic loading. Furthermore, for proper investigation of turbulent flows and the 3D turbulence structures, which have immediate effects on the response of flexible hydrofoils, 3D simulation is a necessity. However, most of the the previous studies on the hydroelastic response of hydrofoils have focused mainly on 2D simulations.

2.5 Objectives

This project seeks to gain greater insight into the hydroelastic response of a 3D highly flexible hydrofoil, incorporating a strongly-coupled two-way fluid-structure interaction. The fluid-structure problem in the present study is solved with a finite volume technique using the CFD code CFX, for the fluid, and a finite element code using the CSD code ANSYS, for the structure.

As discussed in the preceeding literature review, the elastic response and stability of lifting bodies have been studied extensively in the literature. However, to the best of our knowledge, most of the studies are limited to no or small viscous effects, low Reynolds number flows, and low structural deformation due to the low material flexibility. Furthermore, in the numerical studies of hydrofoils, most of the analyses have focused on 2D problems with weak or no FSI.

Accordingly, the objectives of the project are outlined as follows:

- To develop an advanced methodology to investigate the strongly-coupled two-way FSI of a 3D flexible hydrofoil with a focus on the in-water response,
- To improve the accuracy of the available numerical results for the lift and drag coefficients in comparison with the available experimental data,
- To investigate and quantify the foil flexibility effects by studying the differences in structural response as well as hydrodynamic loading (fluid response) between a lightweight, highly flexible hydrofoil and a rigid hydrofoil,
- To investigate the hydrodynamic response of a hydrofoil subject to different flow regimes at moderate to high Reynolds numbers.

CHAPTER 3 THEORETICAL BACKGROUND

The solution of FSI problems involves the simulation of the fluid and solid domains and their interaction. In the present study, we will focus on the interaction between an incompressible flow and a flexible hydrofoil. This area inherits all the difficulties of the 3D turbulent flow simulation in hydrodynamics, and complements them with the ones related to the strong FSI coupling, such as moving boundaries and large mesh deformation. There are various numerical techniques to tackle this kind of problems, some of which will be elaborated on in this chapter. In the study of FSI, which is a complex combination of CFD and CSD, it is essential to understand the basic physical principles and governing equations of these fields. These will be addressed in the present chapter.

3.1 Numerical modeling of Fluid-structure interaction

FSI modeling consists in performing a structural analysis coupled to a corresponding fluid flow analysis. There are two different approaches for solving such problems, the monolithic approach and the partitioned approach, which are described below.

3.1.1 Monolithic approach

In monolithic approaches a single, non-linear, discrete system of equations is considered taking into account both the fluid and the structure domains simultaneously, as described in (Barker and Cai, 2010; Gee, 2011). Figure 3.1 represents the solution process of such an approach in which S^f and S^s denote the fluid and structure solutions, respectively. t_n and t_{n+1} represent the n^{th} and $n+1^{th}$ time steps.

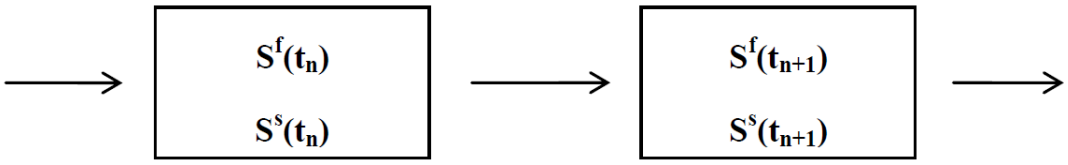

Figure 3.1 Monolithic approach (Raja, 2012)

The interaction between fluid and structure at the interface is treated synchronously in this approach. This leads to the conservation of properties at the interface, which increases the stability of the solution. However, as explained in the previous chapter, this expensive

approach is complicated to implement and leads to ill-conditioned systems due to the different scaling of variables in the multi-field problem (velocity, displacement, pressure).

3.1.2 Partitioned approach

In the partitioned methods, the equations governing the flow field and the structure are solved alternatingly in time with two distinct solvers. The intermediate flow solution is prescribed as a boundary condition to update the structure and vice versa, and the iterations continue until a convergence criterion is satisfied. Figure 3.2 illustrates the solution process in a partitioned approach. The exchange of information occurs at the fluid-structure interface based on the type of coupling technique applied; i.e. one-way or two-way coupling methods that will be described in the following sections.

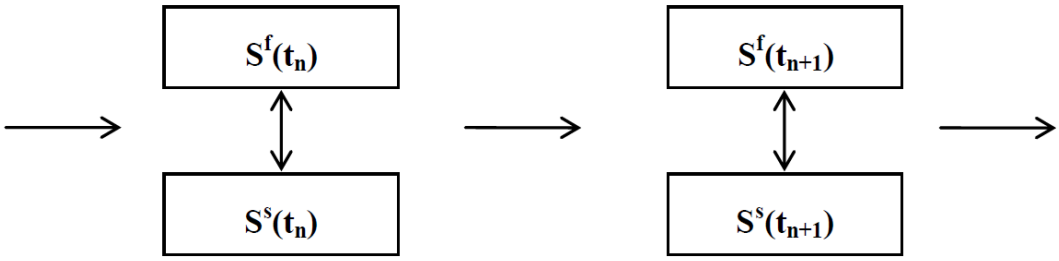

Figure 3.2 Partitioned approach (Raja, 2012)

One-way coupling

In a one-way FSI analysis, the CFD results are transferred and applied as loads to the mechanical model, but the subsequently calculated displacements from the mechanical analysis are not transferred back to the CFD analysis. The other way around is also possible, i.e. the deformation of structure influences the flow field but the reaction of the fluid upon the solid object is negligible.

As illustrated in Fig. 3.3, in a one-way coupling method, initially, the fluid flow calculation is performed until convergence is reached. Then, the resulting forces at the interface from the fluid calculations are interpolated onto the solid computational domain. Next, the structural dynamic calculations are performed until the convergence criterion is reached. This is repeated until the final time of the simulation is reached.

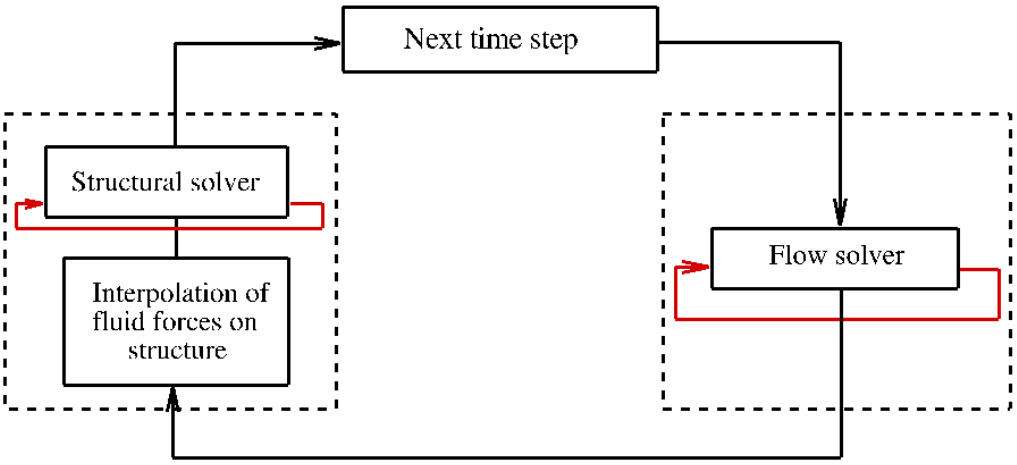

Figure 3.3 One-way coupling

Two-way coupling

The work flow of the strongly-coupled two-way algorithm is depicted in Fig. 3.4. After the first time step, the converged solution of the flow simulation provides the hydrodynamic forces that are applied on the solid body as loads. The loads are then interpolated to the structural mesh. As a consequence, the mesh is deformed according to the displacements of the structure. These displacements are interpolated back to the fluid mesh which results in a deformation of the fluid domain. This process is repeated within each time-step until both forces and displacements are converged to the desired values, which constitutes a strongly-coupled two-way approach used in the present study.

3.1.3 FSI modeling in ANSYS

Recently, many commercial softwares have been developed to simulate FSI problems. Companies like ANSYS provide efficient multi-physics softwares with versatile features. ANSYS supports both one-way and two-way modeling of fluid-structure interaction problems. Regardless of whether one-way or two-way coupling methods are used, the simulations are based on a partitioned method where separate simulation set-ups are required for each physical field.

The FSI problem in the present study is solved with a finite volume technique using the CFD code CFX, for the fluid domain, and a finite element code ANSYS, for the structural domain. The available coupling capability enables CFX to work with the ANSYS Mechanical solver within an ANSYS Multi-field simulation. During coupled simulations, the ANSYS CFX and Mechanical solvers execute the simulation through a sequence of multi-field steps, each of

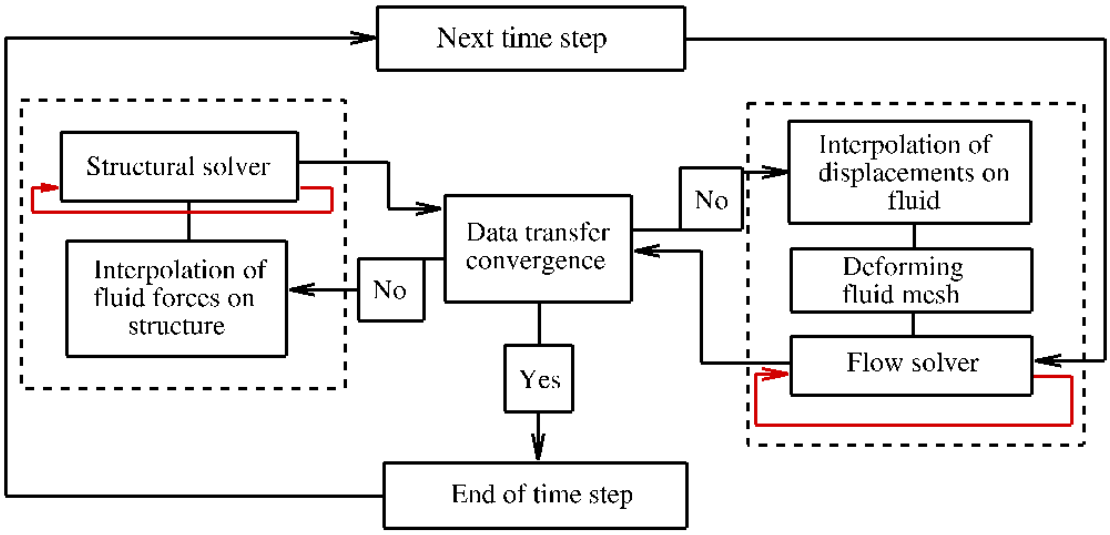

Figure 3.4 Two-way coupling

which consists of one or more coupling iterations (Reference: ANSYS User Guide). The coupling capability available in ANSYS enables CFX to communicate data with the ANSYS Mechanical solver within an ANSYS Multi-field simulation.

Coupled simulations begin with the execution of the Mechanical application and CFX field solvers. The Mechanical application solver is considered as a coupling master process to which the CFX solver connects. Once the connection is established, the solution proceeds through a sequence of six pre-defined synchronization points (SPs), as illustrated in Fig. 3.5.

As mentioned before, multifield simulation set-up requires separate creation of the fluid and structure models in CFX-Pre and the Mechanical application user interfaces, respectively, and the specification of coupling data transfers and controls.

The first three SPs are used to prepare the solvers for the calculation intensive solution process, which takes place during the last three SPs. The last three SPs define a sequence of coupling steps, each of which consists of stagger iterations. During every stagger iteration, each field solver (CFX and ANSYS Mechanical) gathers the required data from the other solver, and solves its field governing equations for the current coupling step. The stagger iterations are repeated until a maximum number of iterations is reached or until convergence is achieved for the data transferred between solvers and all field equations.

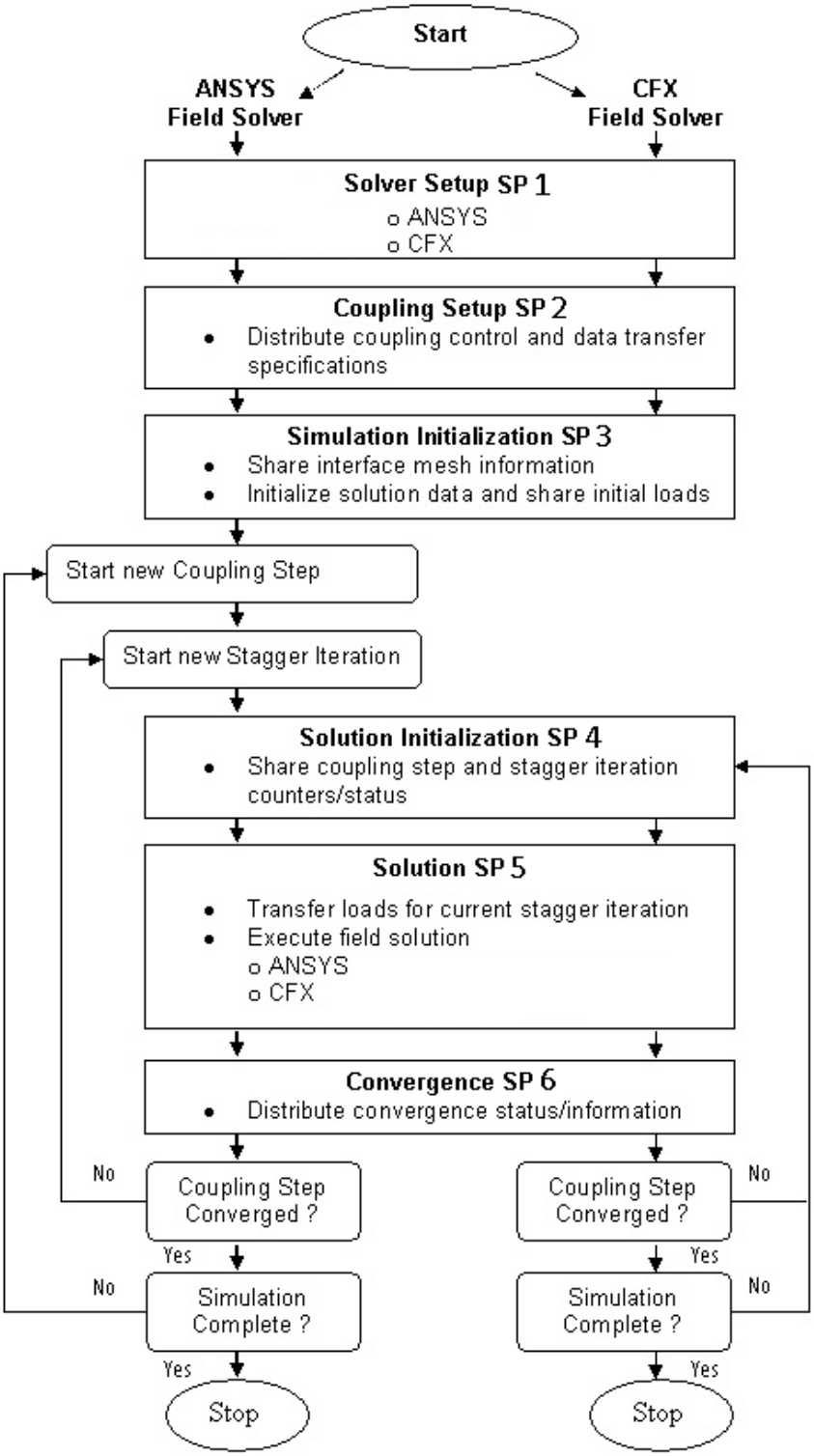

Figure 3.5 Sequence of synchronization points in ANSYS multifield solver (Reference: ANSYS User Guide)

3.2 Governing equations

For the two-way coupling method incorporated in this study, two sets of equations are solved separately for the fluid and solid domains. In addition, mesh deformation is an important component for solving problems with moving boundaries such as FSI. In this section, the governing equations for both the fluid and structure domains are presented.

3.2.1 Fluid domain

The incompressible fluid flow is described with the mass and momentum conservation equations for a Newtonian viscous fluid without body forces and heat transfer.

$$\frac{\partial v_j}{\partial x_j} = 0 \tag{3.1}$$

$$\frac{\partial(\rho_f v_i)}{\partial t} + \frac{\partial(\rho_f v_i v_j)}{\partial x_j} = -\frac{\partial p}{\partial x_i} + \mu_f \frac{\partial^2 v_i}{\partial x_j \partial x_j} \tag{3.2}$$

where v_j, ρ_f, p and μ_f denote the fluid velocity, density and pressure, and dynamic viscosity, respectively.

Reynolds Averaged Navier-Stokes (RANS) Equations

In principle, the Navier-Stokes equations describe both laminar and turbulent flows without the need for additional information. However, the time and space scales of a turbulent motion, characterized by random variations of physical quantities, could be so small that the Direct Numerical Simulation (DNS) of these flows would require an unacceptably large amount of computer resources. Turbulence models have been specifically developed to account for the effects of turbulence without recourse to a prohibitively fine mesh and direct numerical simulation, such as Reynolds-averaged Navier-Stokes (RANS) models, large eddy simulation (LES) and detached-eddy simulation (DES) models.

Simulation of the Reynolds Averaged Navier-Stokes (RANS) equations greatly reduces the computational effort compared to a Direct Numerical Simulation (DNS) and is generally adopted for practical engineering calculations. In this approach, a modified set of transport equations are solved by introducing averaged and fluctuating components. For example, a velocity, V, may be divided into an average component, $\bar{V}$, and a time varying component, V':

$$V = \bar{V} + V' \tag{3.3}$$

The averaged component is given by:

$$\bar{V} = \frac{1}{2\Delta t}\int_{t-\Delta t}^{t+\Delta t} V dt \tag{3.4}$$

where Δt is a time scale that is much smaller than the time scale to which the equations are solved, but large relative to the turbulent fluctuations.

Substituting the averaged quantities into the original transport equations results in the Reynolds averaged equations:

$$\frac{\partial \rho_f}{\partial t} + \frac{\partial}{\partial x_j}(\rho_f \bar{v_j}) = 0 \tag{3.5}$$

$$\frac{\partial \rho_f \bar{v_i}}{\partial t} + \frac{\partial}{\partial x_j}(\rho_f \bar{v_i}\bar{v_j}) = -\frac{\partial p}{\partial x_i} + \frac{\partial}{\partial x_j}(\tau_{ij} - \rho_f \overline{v_i' v_j'}) \tag{3.6}$$

where τ is the molecular stress tensor (including both normal and shear components of the stress).

Eq. 3.6 shows that the averaging procedure in this approach introduces additional unknown terms containing products of the fluctuating quantities, which act like additional stresses in the fluid. These terms, called "turbulent" or "Reynolds" stresses, must be determined as further unknowns. The method used to solve the system defines the type of turbulence model.

Turbulence Modeling

Turbulence consists of various sizes eddies that form and dissipate continuously, and in which the Reynolds stresses are assumed to be proportional to mean velocity gradients. This defines eddy viscosity turbulence models. In this approach, the Reynolds stresses can be related to the mean velocity gradients and turbulent viscosity by a gradient diffusion hypothesis similar to the relationship between the stress and strain tensors in laminar flow:

$$-\rho_f \overline{v_i' v_j'} = \mu_t \left(\frac{\partial \bar{v}_i}{\partial x_j} + \frac{\partial \bar{v}_j}{\partial x_i}\right) - \frac{2}{3}\delta_{ij}\left(\mu_t \frac{\partial \bar{v}_k}{\partial x_k} + \rho_f k\right) \tag{3.7}$$

where μ_t is the eddy viscosity or turbulent viscosity.

Eddy viscosity models cover several methods with different levels of complexity and accuracy such as algebraic (zero equation) models, one-equation models and two-equation models.

Two-equation turbulence models are very widely used, as they offer a good compromise between numerical accuracy and computational effort. In two-equation models, the turbulence velocity scale is computed from the turbulent kinetic energy, k, which is computed as the solution of a transport equation. The turbulent length scale is estimated from two properties of the turbulence field, for instance the turbulent kinetic energy and its dissipation rate.

One of the main challenges in turbulence modeling is the accurate prediction of flow separation from a surface. Standard two-equation turbulence models are often unable to predict the onset of the flow separation under adverse pressure gradient conditions. This is an important phenomenon in many technical applications, particularly for aero/hydrodynamics because the stall characteristics of a foil are controlled by the flow separation from the surface (Reference: ANSYS User Guide). Currently, the most prominent two-equation models in this area are the $k-\omega$ based models.

The current simulation uses the $k-\omega$ Shear Stress Transport (SST) turbulence model (Menter and Egorov, 2005) which has been shown to be an accurate model for boundary layer detachment prediction and turbulence behaviors of flexible foils at high Reynolds numbers (Ducoin and Young, 2013). The superior performance of this model has been demonstrated in a large number of validation studies (Menter et al., 2003; Haase et al., 2006). Further, this model has widely been used in various studies similar to the focus of the current dissertation, such as Refs. (Munch et al., 2010; Hutchison, 2012; Ducoin and Young, 2013; Chae et al., 2013; Akcabay et al., 2014; Akcabay and Young, 2014; Wu et al., 2015; Chae et al., 2016; Akcabay et al., 2017; Wu et al., 2018).

The SST turbulence model combines the advantages of the $k-\epsilon$ model away from the wall and the $k-\omega$ model near the wall. It solves two transport equations, one for the turbulent kinetic energy, k, and one for the turbulent frequency, ω.

$$\frac{\partial}{\partial t}(\rho_f k) + \frac{\partial}{\partial x_j}\left[\rho_f v_j k - (\mu + \sigma^* \mu_t)\frac{\partial k}{\partial x_j}\right] = -\rho_f P - \beta^* \rho_f k\omega \tag{3.8}$$

$$\frac{\partial}{\partial t}(\rho_f \omega) + \frac{\partial}{\partial x_j}\left[\rho_f u_j \omega - (\mu + \sigma \mu_t)\frac{\partial \omega}{\partial x_j}\right] = \frac{\gamma}{\nu_t}\rho_f P - \beta \rho_f \omega^2 + 2(1 - F_1)\frac{\rho_f \sigma_\omega}{\omega}\frac{\partial k}{\partial x_i}\frac{\partial \omega}{\partial x_i} \tag{3.9}$$

The proper transport behavior in SST turbulence model can be obtained by a limiter to the formulation of the eddy-viscosity:

$$\nu_t = \frac{k/\omega}{max\left(1, \frac{\Omega F_2}{a_1 \omega}\right)} \tag{3.10}$$

where

$$\Omega = \sqrt{2\Omega_{ij}\Omega_{ij}} \qquad and \qquad \Omega_{ij} = \frac{1}{2}\left(\frac{\partial v_i}{\partial x_j} - \frac{\partial v_i}{\partial x_j}\right) \tag{3.11}$$

F_1 is the function that allows the use of the $k-\epsilon$ model away from the wall and the $k-\omega$ model near the wall.

$$\begin{aligned} F_1 = \tanh(\zeta^4) \qquad where \qquad & \zeta = min\left[max\left(\frac{\sqrt{k}}{0.09\omega y}, \frac{500\nu}{y^2\omega}\right); \frac{4\rho\sigma_{\omega 2}k}{D_\omega y^2}\right] \\ and \qquad & D_\omega = max\left(\frac{\rho\sigma_{\omega 2}}{\omega}\frac{\partial k}{\partial x_j}\frac{\partial \omega}{\partial x_j}; 10^{-20}\right) \end{aligned} \tag{3.12}$$

The F_2 function is defined as:

$$F_2 = \tanh(\iota^2) \qquad where \qquad \iota = max\left(2\frac{\sqrt{k}}{0.09\omega y}; \frac{500\nu}{y^2\omega}\right) \tag{3.13}$$

where y is the distance from the wall.

The constants in this turbulence models are defined based on the index value of 1 for the $k-\omega$ and 2 for the $k-\epsilon$ standard models. For a constant ϕ, we have:

$$\phi = F_1\phi_1 + (1 - F_1)\phi_2 \tag{3.14}$$

and:

${\sigma_1}^* = 0.5$	;	$\sigma_1 = 0.55$	;	$\beta_1 = 0.0755$	;	$\sigma_{\omega 1} = 0$	
${\sigma_2}^* = 0.8$	;	$\sigma_2 = 0.856$	;	$\beta_2 = 0.0828$	;	$\sigma_{\omega 2} = 0.856$	
$k = 0.41$	;	$a_1 = \sqrt{\beta^*} = 0.3$	;	$\gamma_i = \frac{\beta_i}{\beta^*} - \sigma_i\frac{k^2}{\sqrt{\beta^*}}$	for	$i = 1, 2$	

Transition modeling

In order to accurately capture the major transition effects in the case of separation-induced transition, the turbulence model could be coupled with a laminar-to-turbulent transition model. The effects of incorporating the laminar-to-turbulent transition modeling has been demonstrated in previous literature (Smith et al., 2004). Shelton et al. (Shelton et al.,

2005) incorporated a transition model in their study and showed that the hydrodynamic coefficients match better with the experiments compared to fully turbulent computations. They also showed that the transition models can be important for stall prediction. The experimental and numerical study of Ducoin et al. (Ducoin et al., 2008) has also highlighted the importance of accounting for the transition in the hydrodynamic loading predictions. Based on their conclusion, they coupled the turbulence model in their later studies on the transient flows over hydrofoils (Ducoin et al., 2009a,b).

The SST turbulence model in this study is coupled with the 'Gamma Theta' transition model, which is based on two transport equations, one for the intermittency and one for the transition onset criteria in terms of momentum thickness Reynolds number. CFX uses new empirical correlations based on the studies of (Menter et al., 2004) that has been extensively validated together with the SST turbulence model for a wide range of applications with transitional flows. This will be reviewd in this section (Reference: ANSYS User Guide).

The first transport equation is for the intermittency, γ, which triggers the transition process:

$$\frac{\partial}{\partial t}(\rho_f \gamma) + \frac{\partial}{\partial x_j}(\rho_f U_j \gamma) = P_{\gamma 1} - E_{\gamma 1} + P_{\gamma 2} - E_{\gamma 2} + \frac{\partial}{\partial x_j}\left[(\mu_f + \frac{\mu_t}{\sigma_\gamma})\frac{\partial \gamma}{\partial x_j}\right] \tag{3.15}$$

The transition sources are defined as follows:

$$P_{\gamma 1} = 2F_{length}\rho_f S(\gamma F_{onset})^{c\gamma 3} \tag{3.16a}$$

$$E_{\gamma 1} = P_{\gamma 1}\gamma \tag{3.16b}$$

where S is the magnitude of strain rate. F_{length} is an empirical correlation that controls the length of the transition region.

The destruction/relaminarization sources are defined as follows:

$$P_{\gamma 2} = (2c_{\gamma_1})\rho_f \Omega \gamma F_{turb} \tag{3.17a}$$

$$E_{\gamma 2} = c_{\gamma_2} P_{\gamma 2}\gamma \tag{3.17b}$$

where Ω is the magnitude of vorticity rate. The transition onset is controlled by the following functions:

$$Re_\nu = \frac{\rho_f y^2 S}{\mu_f} \qquad and \qquad R_T = \frac{\rho_f k}{\mu_f \omega} \tag{3.18}$$

$$F_{onset1} = \frac{Re_\nu}{2.193.Re_{\theta_c}} \tag{3.19}$$

$$F_{onset2} = min[max(F_{onset1}, {F^4}_{onset1}), 2.0] \tag{3.20}$$

$$F_{onset3} = max(1 - (\frac{R_T}{2.5})^3, 0)$$

$$F_{onset} = max(F_{onset2} - F_{onset3}, 0)$$

$$F_{turb} = e^{-(\frac{R_T}{4})^4}$$

Re_{θ_c} is the critical Reynolds number where the intermittency first starts to increase in the boundary layer. This occurs upstream of the transition Reynolds number, $\tilde{Re}_{\theta_t}$, and the difference between the two must be calculated from an empirical correlation. F_{length} and Re_{θ_c} correlations are both functions of $\tilde{Re}_{\theta_t}$.

The constants for the intermittency equation are:

$$C_{y1} = 0.03;\ C_{y2} = 50;\ C_{y3} = 0.5;\ \sigma_y = 1.0 \tag{3.21}$$

The modification for separation-induced transition is:

$$\gamma_{sep} = min\left(2.max[(\frac{Re_\nu}{3.235Re_{\theta_c}}) - 1.0]F_{reattach}, 2\right) F_{\theta_t} \tag{3.22}$$

$$F_{reattach} = e^{-(\frac{R_T}{20})^4} \tag{3.23}$$

$$\gamma_{eff} = max(\gamma, \gamma_{sep}) \tag{3.24}$$

The transport equation for the transition momentum thickness Reynolds number, $\tilde{Re}_{\theta_t}$, reads:

$$\frac{\partial\left(\rho\tilde{Re}_{\theta t}\right)}{\partial t} + \frac{\partial\left(\rho U_j\tilde{Re}_{\theta t}\right)}{\partial t} = P_{\theta t} + \frac{\partial}{\partial x_j}\left[\sigma_{\theta t}\left((\mu + \mu_t)\frac{\partial\tilde{Re}_{\theta t}}{\partial x_j}\right)\right] \tag{3.25}$$

The source term is defined as follows:

$$P_{\theta t} = c_{\theta t}\frac{\rho}{t}(Re_{\theta t} - \tilde{Re}_{\theta t})(1.0 - F_{\theta t});\ t = \frac{500\mu}{\rho U^2} \tag{3.26}$$

$$F_{\theta t} = min\left(max\left(F_{wake} \cdot e^{-\left(\frac{y}{\delta}\right)^4}, 1.0 - \left(\frac{\gamma - 1/50}{1.0 - 1/50}\right)^2\right), 1.0\right) \tag{3.27}$$

$$\theta_{BL} = \frac{\tilde{Re}_{\theta t}\mu}{\rho U};\ \delta_{BL} = \frac{15}{2}\theta_{BL};\ \delta = \frac{50\Omega y}{U} \cdot \delta_{BL} \tag{3.28}$$

$$Re_{\omega} = \frac{\rho\omega y^2}{\mu};\ F_{wake} = e^{-\left(\frac{Re_{\omega}}{1\times10^5}\right)^2} \tag{3.29}$$

The model constants for the $\tilde{Re}_{\theta t}$ equation are:

$$c_{\theta t} = 0.03;\ \sigma_{\theta t} = 2.0 \tag{3.30}$$

The model contains three empirical correlations; $Re_{\theta t}$ which is the transition onset as observed in experiments and goes in Eq. 3.26, F_{length} is the length of the transition zone and is used in Eq. 3.16), and $Re_{\theta c}$ is the point where the model is activated in order to match both $Re_{\theta t}$ and F_{length} and goes into Eq. 3.19.

The transition model interacts with the SST turbulence model, as follows:

$$\frac{\partial}{\partial t}(\rho_f k) + \frac{\partial}{\partial x_j}(\rho_f u_j k) = \tilde{P}_k - \tilde{D}_k + \frac{\partial}{\partial x_j}\left((\mu_f + \sigma_k\mu_t)\frac{\partial k}{\partial x_j}\right) \tag{3.31}$$

$$\tilde{P}_k = \gamma_{eff}P_k;\ \tilde{D}_k = min(max(\gamma_{eff}, 0.1), 1.0)D_k \tag{3.32}$$

$$R_y = \frac{\rho_f y\sqrt{k}}{\mu};\ F_3 = e^{-(\frac{R_y}{120})^8}; F_1 = max(F_{1orig}, F_3) \tag{3.33}$$

where P_k and D_k are the original production and destruction terms for the SST model and F_{1orig} is the original SST blending function.

The reader is referred to Ref. (Menter et al., 2004) for more details on the above model formulation.

Modeling Flow Near the Wall

The structure of any flow field is noticeably influenced by the presence of solid walls where mean and fluctuation velocities become zero due to the no-slip conditions. There are strong

gradients in the dependent variables near a no-slip wall and viscous effects on the transport processes are also large.

It is illustrated in Fig. 3.6 that the near-wall region can be subdivided into two layers (Reference: ANSYS User Guide). The viscous sublayer is the innermost layer, where the flow is almost laminar-like, and the viscosity plays a dominant role in momentum. Further away from the wall, in the logarithmic layer, turbulence dominates the mixing process. There is also a buffer layer between the viscous sublayer and the logarithmic layer, where the effects of viscosity and turbulence are of equal importance .

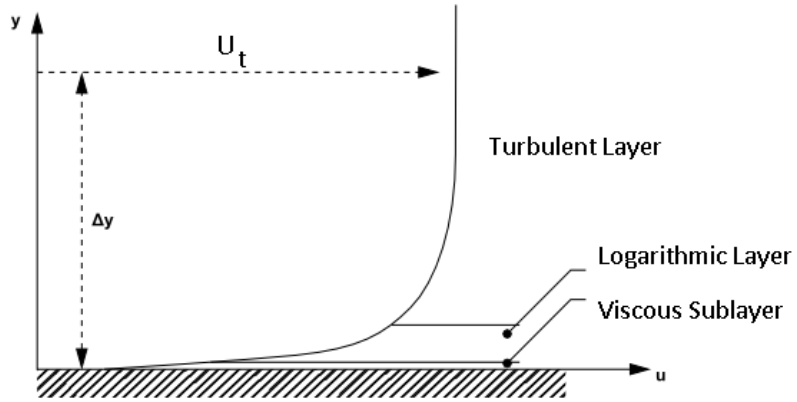

Figure 3.6 Subdivisions of the near-wall region (Reference: ANSYS User Guide)

The differential Reynolds stress and standard turbulence models, are applicable only to the full turbulent regions, outside the so called viscous layers, where the flow is considered to be only controlled by the turbulent stresses. However, an appropriate turbulence model closure is required in the near-wall region in order to correctly predict the behavior of the flow.

To model the flow in the near-wall region in ANSYS CFX, two approaches are commonly used (Reference: ANSYS User Guide) which will be reviewed in the following sections.

Scalable wall functions

Assuming that the logarithmic profile reasonably approximates the velocity distribution near the wall, it provides a means to numerically compute the fluid shear stress as a function of the velocity at a given distance from the wall. This is known as a "wall function".

The wall function method uses empirical formulas that impose suitable conditions near the wall without resolving the boundary layer. Hence, the major advantage of the wall function approach is that the high gradient shear layers near walls can be modeled with relatively coarse meshes, yielding substantial savings in computational resources.

The logarithmic relation for the near wall velocity in this approach is given by:

$$u^+ = \frac{U_t}{u_\tau} = \frac{1}{\kappa} ln(Y^+) + C \tag{3.34}$$

where u^+ is the near wall velocity, $u_\tau = \sqrt{\tau_w/\rho_f}$ denotes the friction velocity, U_t is the known velocity tangent to the wall at a distance of Δy from the wall, κ denotes the von Karman constant (≈ 0.41), and C is a constant depending on the wall roughness. τ_w denotes the wall shear stress and Y^+ is the non-dimensional wall distance, defined as:

$$Y^+ = \frac{\rho_f u_\tau \Delta y}{\mu_f} \tag{3.35}$$

Equation 3.34 has the problem that it becomes singular at separation points where the near wall velocity approaches zero. An alternative velocity scale, u^*, is used instead of u_τ in the logarithmic region.

$$u^* = {C_\mu}^{1/4} k^{1/2} \tag{3.36}$$

The following explicit equation is obtained to compute u_τ based on the above definition:

$$u_\tau = \frac{U_t}{\frac{1}{k} ln(Y^*) + C} \tag{3.37}$$

The absolute value of the wall shear stress τ_w, is then obtained from the following equation:

$$\tau_w = \rho_f u^* u_\tau \tag{3.38}$$

where:

$$Y^* = \frac{\rho_f u^* \Delta y}{\mu_f} \tag{3.39}$$

One of the main disadvantages of the wall function formulation is that the computations depend on the location of the first node away from the wall and are sensitive to the near-wall meshing. If the value of Y^+ is too large, then the wall function will impose wall type conditions further from the wall than would normally be appropriate. The use of the "scalable wall function" formulation in ANSYS CFX has removed issues associated with the lower valid limit for Y^+.

The incentive for the formulation of the scalable wall function is to limit the Y^* value used in the logarithmic formulation by introducing a limiter in the Y^* calculations such that:

$$\tilde{Y}^* = max(Y^*, Y^*_{limit}) \tag{3.40}$$

$Y^*_{limit} = 11.06$ is the value of Y^* at the intersection between the logarithmic and the linear near wall profile. The use of Eq. 3.40 in the context of the scalable wall functions concept is straightforward, that is, the Y^* formulation used for any standard wall function formula is replaced by $\tilde{Y}^*$. All mesh points are thus outside the viscous sublayer and all fine mesh inconsistencies are prevented.

The following relation, which is valid in the logarithmic region, yields the boundary condition for the dissipation rate, ϵ:

$$\epsilon = \frac{\rho_f u^*}{\tilde{Y}^* \mu} \frac{{C_\mu}^{3/4}}{k} k^{3/2} \tag{3.41}$$

Automatic near-wall treatment

The wall functions presented above, which enable a consistent mesh refinement, are based on problematic physical assumptions, particularly in flows at lower Reynolds numbers ($Re < 10^5$), since the sublayer part of the boundary layer is not considered in the mass and momentum balance. This can cause an error in the displacement thickness of up to 25% for flows at low Reynolds numbers.

Ideally, we would want a formulation which would automatically switch from wall functions to a low-Re near wall formulation as the mesh is refined. The $k - \omega$ model has the benefit of providing an analytical expression for ω in the viscous sublayer, which can be used in order to reach this goal. The aim of the current formulation is to blend the wall value for ω between the logarithmic and the near wall formulation.

The automatic wall treatment, which is used in the present study, allows a consistent Y^+ insensitive mesh refinement from coarse grids, which do not resolve the viscous sublayer, to fine grids placing mesh points inside the viscous sublayer. It has to be mentioned that for highly accurate simulations, like the present study, a fine grid with Y^+ around 1 is recommended.

The flux for the $k-$equation is artificially kept at zero; $F_k = 0$. The flux in the momentum equation, F_U, is computed from the velocity profile:

$$F_U = -\rho_f u_\tau u^* \tag{3.42}$$

with:

$$u^* = \sqrt[4]{\left(\sqrt{\frac{\mu_f}{\rho_f} \mid \frac{\Delta U}{\Delta y} \mid}\right)^4 + \left(\sqrt{a_1 k}\right)^4} \tag{3.43}$$

$$u_\tau = \sqrt[4]{(u_\tau^{vis})^4 + \left(u_\tau^{log}\right)^4} \tag{3.44}$$

where:

$$u_\tau^{vis} = \sqrt{\frac{\mu_f}{\rho_f} \mid \frac{\Delta U}{\Delta y} \mid} \tag{3.45}$$

and

$$u_\tau^{log} = \frac{U}{1/klog(Y^+) + C} \tag{3.46}$$

An algebraic expression is specified in the ω-equation instead of an added flux. It is a blend between the analytical expression for ω in the logarithmic region (Eq. 3.47) and the corresponding expression in the sublayer (Eq. 3.48).

$$\omega_l = \frac{u^*}{a_1 k y} = \frac{1}{a_1 k \nu} \frac{u^{*2}}{Y^+} \tag{3.47}$$

$$\omega_s = \frac{6\nu}{\beta(\Delta y)^2} \tag{3.48}$$

Δy represents the distance between the first and the second mesh points. The following formulation is opted for to achieve a smooth blending and to avoid cyclic convergence behavior:

$$\omega_\omega = \omega_s \sqrt{1 + \left(\frac{\omega_l}{\omega_s}\right)^2} \tag{3.49}$$

Mesh Deformation

Mesh deformation is an important component for solving problems with moving boundaries. In a two-way FSI, mesh motion is an implicit part of the coupled simulation. At every time-step, once the new solid position is computed from the structural solver, the fluid mesh has

to be deformed to conform to the new solid position.

The mesh deformation model utilised in ANSYS CFX is "Displacement Diffusion". In this approach, the mesh is treated as an elastic solid and it is constrained to conform to the moving structure geometry, as well as the other domain boundaries. With this model, the displacements applied on domain boundaries or in domains are diffused to other mesh points by solving the following equation (Reference: ANSYS User Guide):

$$\nabla.(\Gamma_{disp}\nabla\delta) = 0 \tag{3.50}$$

where δ is the displacement relative to the previous mesh locations and Γ_{disp} is the mesh stiffness, which determines the degree to which regions of nodes move together.

With a constant mesh stiffness applied in the simulation, displacements are homogeneously diffused throughout the mesh. When a variable stiffness is specified for the mesh throughout the domain, there is little relative motion and nodes in regions of high stiffness move together. Variable mesh stiffness is particularly useful to preserve the mesh quality and limit mesh distortion issues near fine geometrical features (such as the hydrofoil trailing edge) and/or boundary layer elements. The mesh stiffness should increase in regions where mesh distortion is most likely to occur. There are two available options for variable mesh stiffness in CFX; increase stiffness near boundaries and increase stiffness near small volumes.

Increase stiffness near boundaries

By increasing the stiffness near certain boundaries in the domain, such as walls, the interior mesh (that is, away from those boundaries) absorbs more mesh motion. This option does not depend upon the control volume size distribution in the original mesh and it treats regions near all wall, interface, inlet, outlet, and opening boundaries identically. Γ_{disp}, applied in the displacement diffusion equation is determined from the following relationship:

$$\Gamma_{disp} = (\frac{L_{ref}}{d})^{C_{stiff}} \tag{3.51}$$

This relationship provides an exponential increase in the mesh stiffness as the distance from the nearest boundary, d, decreases. The stiffness model exponent, C_{stiff}, determines how quickly this increase occurs. For example, large values will yield a much more abrupt stiffness variation.

L_{ref} is the reference length, which can be automatically computed (as a global length scale) or directly specified. The reference length should be representative of a typical length within

the model (Reference: ANSYS User Guide).

Increase stiffness near small volumes

By increasing the stiffness near small mesh volumes, mesh quality will benefit from having larger control volumes absorb more mesh motion. Applying this option in the simulation and its behavior does depend on the initial mesh distribution, for instance, having a fine mesh in regions where the motion is likely to be more significant.

The following equation is used to determine the mesh stiffness, Γ_{disp}, applied in the displacement diffusion equation:

$$\Gamma_{disp} = (\frac{\forall_{ref}}{\forall})^{C_{stiff}} \tag{3.52}$$

According to this relationship, the mesh stiffness increases exponentially, as the control volume size ($\forall$) decreases. $\forall_{ref}$ is the reference volume, which can be automatically computed (as a mean control volume) in the domain or directly specified. The reference volume should be representative of a typical control volume within the domain. C_{stiff} is the stiffness model exponent that determines how quickly the exponential increase in the mesh stiffness occurs. For instance, large values will yield a much more abrupt stiffness variation (Reference: ANSYS User Guide).

In the present study, in which interactions take place between two different domains, care has to be taken to generate very fine meshes at the interface. Furthermore, in order to reproduce flow phenomena like laminar separation bubble and transition, which have immediate effect on the foil response and hydrodynamic loading, boundary layer elements have to be generated. Mesh refinements have also to be performed near the foil leading edge, trailing edge and in the wake region in order to accurately capture the turbulence features over the foil. Therefore, to mitigate the mesh distortion close to the small volume elements, the mesh stiffness is specified to be inversely proportional to the volumes of elements in this study.

3.2.2 Structural model

The structure behavior is described in the frame of linear elasticity, using the following displacement formulation (Ducoin et al., 2009b; Lai et al., 2010; Mortazavinia et al., 2012):

$$\sigma_{ij} + \rho_s f_i = \rho_s \ddot{v}_i \tag{3.53}$$

where ρ_s is the solid density, σ_{ij} and f_i are the components of the stress tensor and body force in the solid domain, respectively and v_i represent the components of the velocity field. σ_{ij} can be obtained from the constitutive equation of the material. For a Hookean elastic solid, it is:

$$\sigma_{ij} = \lambda e_{kk}\delta_{ij} + 2\mu_L e_{ij} \tag{3.54}$$

where λ and μ_L are Lame's constants and δ_{ij} is the Kronecker delta. e_{ij} are the components of the strain tensor and can be expressed as:

$$e_{ij} = \frac{1}{2}(\frac{\partial d_i}{\partial x_j} + \frac{\partial d_j}{\partial x_i} - \frac{\partial d_k}{\partial x_i}\frac{\partial d_k}{\partial x_j}) \tag{3.55}$$

It has to be mentioned that in the present study, due to the high hydrodynamic loading from the flow, the structure undergoes large deformation. Hence, the geometrical nonlinearities have to be considered and the nonlinear form of equations has to be taken into account.

Lame's constants are related to Young's modulus E, and Poisson's ratio ν, by the following equations Lai et al. (2010); Mortazavinia et al. (2012):

$$\lambda = \frac{\nu E}{(1+\nu)(1-2\nu)} \tag{3.56}$$

$$\mu_L = \frac{E}{2(1+\nu)} \tag{3.57}$$

By combining the above equations, the Navier's equation of motion is obtained which can be written as:

$$(\lambda + \mu_L)\nabla(\nabla.\mathbf{d}) + \mu_L\nabla^2\mathbf{d} + \rho_s\mathbf{f} = \rho_s\dot{\mathbf{v}} \tag{3.58}$$

The technique which is used to determine the dynamic response of a structure under the action of any type of time-varying loads is a transient dynamic analysis. The basic equation of motion solved by a transient dynamic analysis is:

$$M\ddot{d} + C\dot{d} + Kd = F(t) \tag{3.59}$$

where:

M = mass matrix
C = damping matrix
K = stiffness matrix
$\ddot{d}$ = nodal acceleration vector
$\dot{d}$ = nodal velocity vector
d = nodal displacement vector
$F(t)$ = load vector

This type of analysis is used in ANSYS to determine the time-dependent displacements, strains, stresses, and forces in a structure as it responds to any transient loads (Reference: ANSYS User Guide).

CHAPTER 4 DESCRIPTION OF THE TEST CASE

This thesis numerically models a 3D hydrofoil subjected to water flow. The aim is to study the hydroelastic behavior of flexible hydrofoils. To investigate and quantify the effects of hydrofoil flexibility, a solid understanding of the rigid foil dynamics is required. This will be undertaken by comparing the performance of rigid and flexible hydrofoils. In addition, the hydroelastic response and stability of rigid and flexible hydrofoils will be studied at various operating condition; i.e. different inlet velocities and angles of attack.

In our study, a two-way strongly-coupled FSI approach is used to study the interaction between the hydrofoil and water flow. As explained in the previous chapters, the fluid part and the solid part are solved separately, using their own numerical methods and the interaction takes place regularly between the two solvers via the available coupling scheme in ANSYS.

In this chapter, the study test case will be described. The geometry details and both of the fluid and solid domains will be presented along with the appropriate boundary conditions.

4.1 Geometry selection

The selected foil to study in this project is a cambered foil of the NACA66 series. This foil is chosen because there are several studies available in the literature that have numerically or experimentally investigated the flow over this type of hydrofoil, such as (Leroux et al., 2004; Ducoin et al., 2009b,a, 2012b; Ducoin and Young, 2013; Akcabay et al., 2014; Akcabay and Young, 2014; Wu et al., 2015; Tran et al., 2015; Wu et al., 2018). The experimental study of Akcabay et al. (Akcabay et al., 2014) on the NACA66 hydrofoils will be our main reference to validate our numerical FSI results. The experimental set-up for the flexible hydrofoil is shown in Fig.4.1.

The 3D NACA66 hydrofoils have a 12% maximum thickness-to-chord ratio, a 0.8 camber distribution, a maximum camber-to-chord length ratio of 2%, a constant chord length c =0.15 m, and span length b=0.191 m, for which the theoretical coordinates are given in appendix A (Ref. (Leroux et al., 2004)).

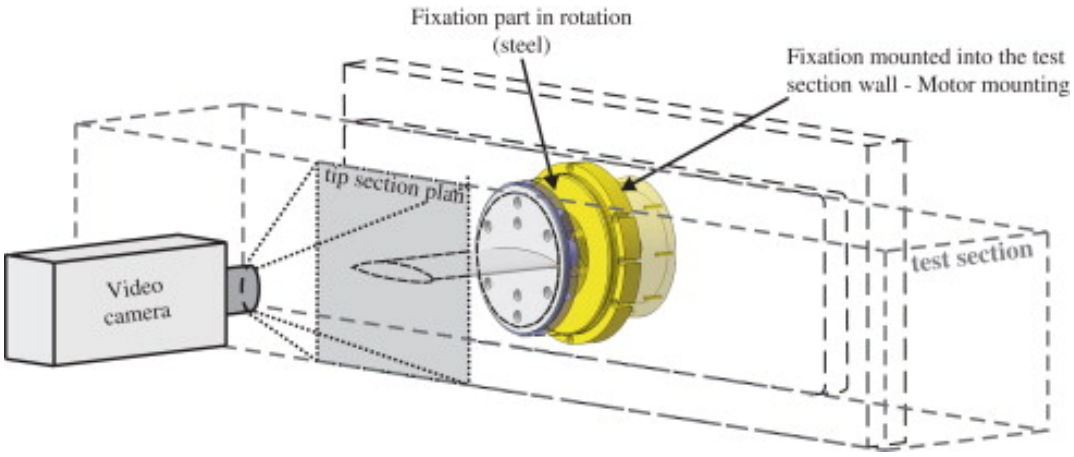

Figure 4.1 The experimental set-up for NACA66 flexible hydrofoil in Ref. (Akcabay et al., 2014)

4.2 Fluid domain

The 3D domain of the CFD solver, shown in Fig. 4.2, is 2.25 m long and 0.192 m tall with a width equal to the foil span length, which matches the dimensions of the experimental facility in the study of (Akcabay et al., 2014). The set-up involves a cantilevered hydrofoil with a uniform cross-section that is mounted horizontally at mid-height of the test section. The foil is clamped to the side wall of the tunnel section (foil root) and free to move on the other side of the test section wall (foil tip). In the experimental studies of Akcabay et al. (Akcabay et al., 2014) and Ducoin and Young (Ducoin and Young, 2013) there was a 1 mm clearance (0.5% of the foil span) between the free tip of the hydrofoil and the other end of the test section wall. However, according to both experimental and numerical simulations in the study of (Ducoin and Young, 2013), the foil tip is located in the boundary layer of the tunnel wall which limits the effects of tip vortices in the gap region. Hence, this gap is neglected in the present study.

The fluid domain is 15c long, the foil leading edge is at 4.5c from the inlet, and the foil trailing edge is at 9.5c from the outlet.

The density and dynamic viscosity of the fluid are $\rho_f = 997kg/m^3$ and $\mu_f = 8.9\times10^{-4}kg/(ms)$, respectively, which correspond to pure water at $25°c$, as specified in the experiments of (Akcabay et al., 2014).

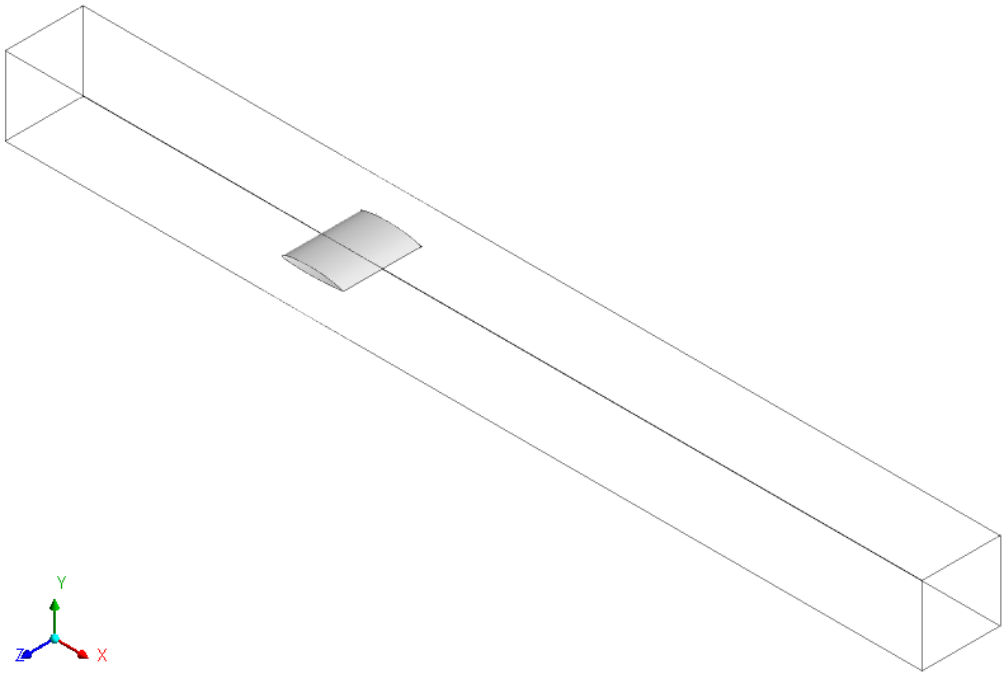

Figure 4.2 3D domain of the computational fluid dynamics solver

4.3 Structural domain

The structural domain is shown in Fig. 4.3. As explained in the previous sections, to investigate the effects of material flexibility on the hydroelastic response of hydrofoils, both rigid and the flexible hydrofoils will be studied in this dissertation. A rigid hydrofoil, made of stainless steel, and a flexible hydrofoil, made of POM Polyacetate, are in the same operating conditions, both with identical initial undeformed geometries. The specific properties of the materials are given in Table 4.1.

Table 4.1 Material properties of the rigid and flexible hydrofoils

	Modulus of elasticity E (GPa)	Density ρ (kg/m^3)	Poisson ratio ν
Stainless steel (rigid)	210	7800	0.30
POM Polyacetate (flexible)	3	1480	0.35

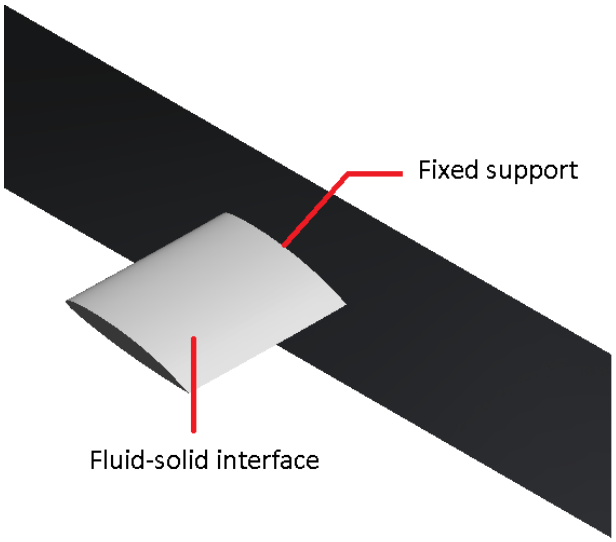

Figure 4.3 Solid domain

4.4 Boundary conditions

The hydrofoil in the experimental study of Akcabay et al. (Akcabay et al., 2014) was subjected to an inlet flow velocity of u_0= $5m/s$. Hence, u_0= $5m/s$ is the nominal free stream velocity in the X-direction used in the validation part of our study. However, higher values of u_0= $10m/s$, $15m/s$, $20m/s$ and $25m/s$ are also applied as nominal free stream velocities in subsequent study cases to investigate the hydroelastic response of hydrofoils at higher Re number flows. The inlet velocities of u_0= $5m/s$ to u_0= $25m/s$ yield a moderate to high Reynolds number of $Re = 0.75 \times 10^6$ to $Re = 3.75 \times 10^6$. A constant turbulent intensity of 2.95%, which is equal to the experimentally measured turbulent intensity in Ref. (Akcabay et al., 2014), is set at the inlet boundary.

The outlet pressure is set to a zero average, and no-slip and no-penetration conditions are applied on the hydrofoil surface. A no-slip wall boundary condition is also imposed on the back wall of the tunnel, to which the foil is clamped.

As indicated in Ref. (Akcabay et al., 2014), the hydrofoil free tip is located within the boundary layer of the wall and this minimizes the tip vortices. Therefore, in this study, the 1 mm gap between the free tip of the hydrofoil and the other end of the test section wall is neglected. Under this assumption, a free-slip wall condition is imposed on the other side plane of the test section that allows the free tip to move and enables the water-induced deformation of the hydrofoil.

Symmetrical conditions are applied at the top and bottom walls of the computational domain, as opposed to a wall boundary condition, which would require much finer elements near the top and bottom walls. This reasonable boundary condition is used in many studies available in the literature (Ducoin and Young, 2013; Akcabay et al., 2014; Akcabay and Young, 2014; Chae et al., 2013; Wu et al., 2015). Because the blockage ratio, defined as the ratio between the maximum thickness of the profile and the height of the tunnel test section, is less than 7% and, thus, the effect of blockage is negligible (Munch et al., 2010).

Transient structural analysis is used, and the total force computed from the CFD transient simulation is interpolated at the fluid structure interface. The foil surface is specified as the fluid-solid interface in both fluid and solid domains. The fixation system of the hydrofoil is rigid. Hence, it is not considered in the computations and a clamped condition (fixed support) is set on the root section, whereas the foil is free to move at the tip. The structural constraints on the foil are shown in Fig. 4.3.

CHAPTER 5 METHODOLOGY

A 3D strongly-coupled two-way fluid-structure interaction methodology with sufficiently high spatial accuracy will be incorporated to study the hydroelastic response of flexible hydrofoils.

In this chapter:

- Some of the important aspects of the fluid and structural modelling and numerical set-ups, including the mesh deformation modeling, will be presented.
- The viscous fluid solver, described in the previous chapters, will be validated by comparing the numerical results for a NACA0012 airfoil with measured experimental data for a range of Reynolds numbers and angles of attack.
- Mesh convergence study will be conducted for the case corresponding to a rigid NACA66 hydrofoil at an angle of attack of α=8°.
- The two-way FSI coupling method in our study will be validated by comparing the numerical results with the available experimental data for rigid and flexible NACA66 hydrofoils.
- One-way and two-way FSI coupling methods will be compared for the analysis of the flexible hydrofoils.
- Effects of transition modelling on laminar to turbulent flow transition over the foils will be investigated.

The proposed methodology will be used in the next chapter to investigate the hydrodynamic response of the hydrofoils subjected to different flow regimes including higher Reynolds number flows. It will be shown that the proposed methodology is able to accurately predict the local phenomena at the interface, such as development and movement of LSB that has been shown to have immediate effects on the hydroelastic response of the structure.

5.1 Numerical set-up: fluid domain

The fluid domain shown in Fig. 4.2 and Fig. 5.1.(a) has boundaries that match the experimental test section of the NACA66 hydrofoil measurements and is used in this study for the sake of validation of the results. However, to avoid confinement effects caused by large elastic

foil deformations, particularly in the case of flexible hydrofoil at highly loaded conditions; i.e. high angles of attack or high Re number flows, the infinite-like boundary fluid domain shown in Fig. 5.1.(b) is used. As depicted in this figure, the top and bottom walls of the domain are moved far enough to avoid blockage effects.

Both domains are 15c long, the foil leading edge is at 4.5c from the inlet, and the foil trailing edge is at 9.5c from the outlet. Domain 2 differs from domain 1 with a much greater distance between the foil and the top and bottom boundaries.

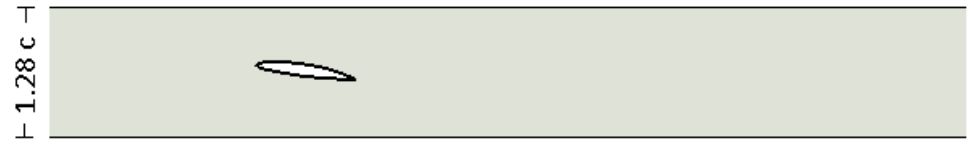

(a)

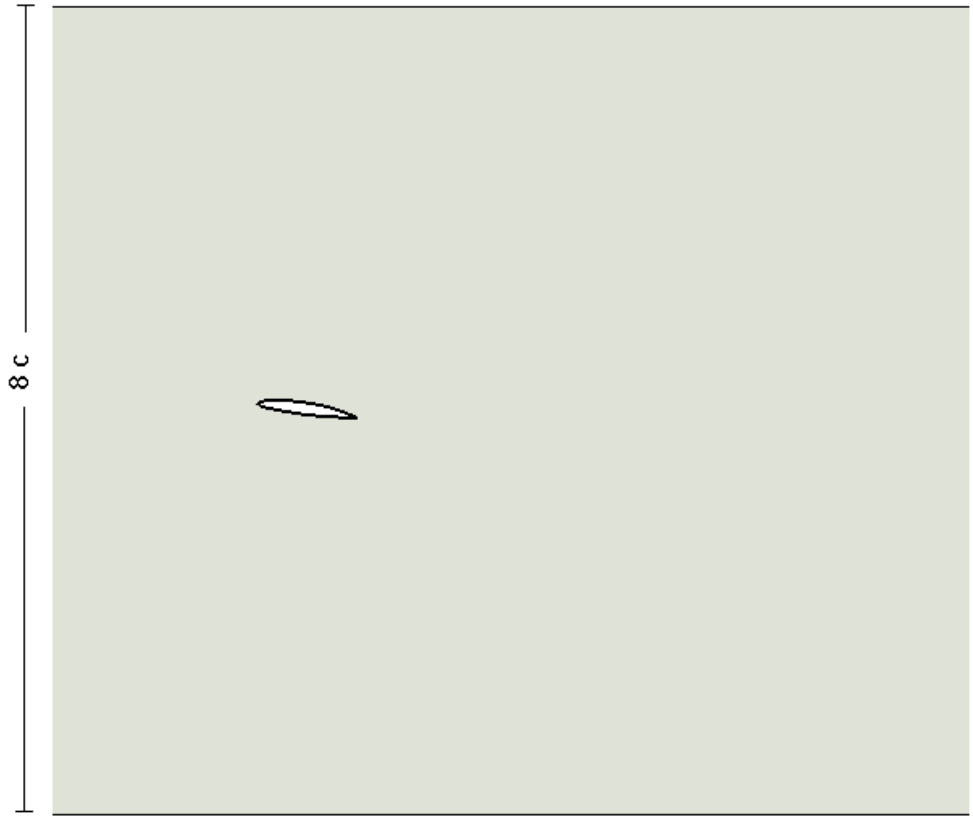

(b)

Figure 5.1 (a) Domain 1 corresponds to experimental facility for use in the validation of the results; (b) The infinite-like boundary domain (Domain 2)

5.1.1 Inlet velocity

As the fluid flows over the hydrofoil, the latter initially oscillates and then damps to a steady-state position. The present study focuses only on static response of the hydrofoil, and therefore only steady-state results will be presented.

The transient coupled FSI simulations are initialized with steady-state calculations. This initialization is suitable for cases in which the initial fluid force on the FSI interface will not cause a sudden deformation of the structure at the start of the transient simulation, causing the solvers to fail. However, for highly flexible hydrofoils subjected to high Re number flows, there exist an issue regarding the sudden deformation of the foil. As the high-turbulence incoming flow reaches the flexible hydrofoil, it suddenly causes high deformation in the foil and as a consequence, the simulation stops after the first few iterations due to the highly distorted elements in the domain. In this case, the deformation can be applied gradually, to reduce the likelihood of mesh folding.

In the present study, mesh folding is avoided by slowly ramping up the velocity inlet boundary condition from an initial value of $u_{initial}$ to the desired value of u_0, as shown in Fig. 5.2. It is shown that for instance, for a study test case of flow with u_0= $15m/s$, the fluid flow starts with an inlet velocity of $u_{initial}$=$2m/s$ over the foil and slowly reaches u_0=$15m/s$ in t_1=$0.5sec$. For the test case with u_0=$20m/s$, the inlet velocity ramps up with the same slope and reaches its maximum value in t_1=$0.69sec$. T is the final time when the simulation becomes steady-state. It has to be mentioned that the slope of the velocity ramp-up, $u_{initial}$ and t_1 are chosen based on the numerical experiment during this study.

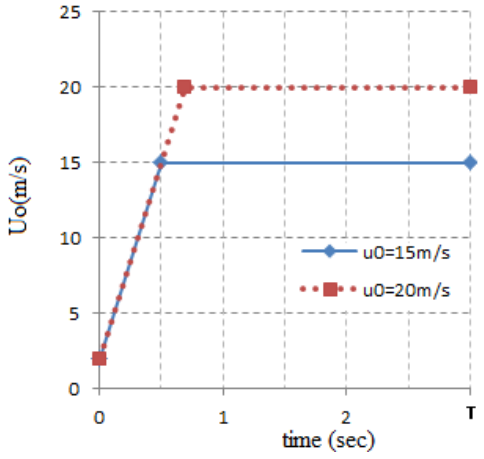

Figure 5.2 Inlet velocity

5.1.2 Undeformed (initial) mesh

To limit mesh distortion issues in the moving boundary problem at hand, care was taken to ensure that the initial mesh is fine enough. Furthermore, in the study of hydroelasticity, the mesh resolution should be high enough particularly at the interface between fluid and solid domains where interaction takes place between a highly flexible stucture and a viscous flow. It is only with the use of a fine mesh that we will be able to reproduce flow phenomena like laminar separation bubble and transition, which have immediate effect on the foil response and hydrodynamic loading and might lead to vibration of flexible hydrofoils.

The mesh convergence study, which will be presented in Section 5.4, shows the effects of mesh refinement on the flow parameters such as pressure coefficient distribution along the hydrofoil surface and the hydrodynamic lift coefficient. It suffices to mention in this section that the mesh used for the CFD analysis is constructed with 2,660,000 elements in ANSYS ICEM CFD. A close-up view of the fluid mesh is shown in Fig. 5.3 for the confined case (domain 1), which will be used for the sake of mesh convergence study and validation of the results with experiments in Chapter 6. Care was taken to generate boundary layer elements that ensure $Y^+ \approx 1$, as will be explained in the next chapter. As depicted in Fig. 5.3, mesh refinements are performed in the regions with high gradients of the flow parameters, such as high curvature region near the foil leading edge, the trailing edge and wake regions.

5.1.3 Mesh deformation

Using a mesh of adequate geometric quality is an important part of controlling discretization error, particularly in problems with moving boundaries. It has to be mentioned that in the transient moving boundary problem at hand, each operating condition, i.e. each angle of attack and inlet velocity, requires a specific setting of the mesh deformation parameters depending on the magnitude of the mesh displacement. It is not feasible to propose a unique methodology for all test cases with different operating conditions and consequently, different hydroelastic deformations. In the test cases with high deformations, each initial mesh setting leads to its own specific solution and because, to the best of our knowledge, there is no available experimental data for high Re number flows, the results cannot be validated. Thus, our methodology in the case of flow with u_0=$5m/s$ is based on validating the results with the experimental data in Ref. (Akcabay et al., 2014), as will be explained in Chapter 6. However, for the test cases with higher inlet velocities, we will:

1. generate an initial mesh with acceptable quality and run the simulation,

2. post process the results and verify if the deformed mesh has acceptable quality so that

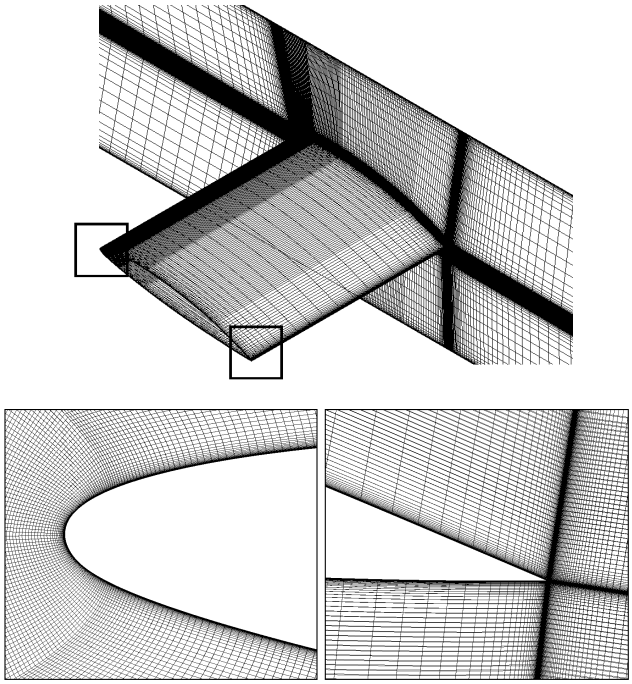

Figure 5.3 Fluid mesh details

the obtained results are reliable,

3. identify the proper settings and adjustments to reach the desireable mesh quality, on which the final computations will be performed.

Variable mesh stiffness

The mesh deformation is determined by the variable mesh stiffness which should increase in regions where mesh distortion is most likely to occur. In the present study, the mesh stiffness is specified to be inversely proportional to the volumes of elements to mitigate the mesh distortion close to the small volume elements, such as high aspect ratio boundary layer elements, and the small elements near the leading and trailing edges of the foil. Since the mesh elements are finer near the hydrofoil, they are stiff enough to move with the hydrofoil without much of distortion. However, the relatively larger mesh elements far away from the hydrofoil in the domain might get distorted, because the mesh at the flow inlet and outlet is assumed to be stationary, while the mesh could stretch or compress towards the bottom and top boundaries in the domain. Hence, care must be taken to ensure that the mesh size is fine enough to limit mesh distortion issues after each structural displacement.

In this section, we will study the effect of mesh stifness and identify the mesh quality for a test

case corresponding to the flexible hydrofoil at α= 8°. For this purpose, the stiffness model exponent in Eq. 3.52, C_{stiff}, will be studied which determines how quickly the exponential increase in the mesh stiffness occurs.

Mesh quality

Mesh orthogonality angle and mesh expansion factor are the two measures of mesh quality which are most relevant to the CFX-Solver and will be investigated in this study. Readers could refer to the ANSYS User Guide for more details and the explanation of mesh quality measures. However, it suffices to mention that the concept of mesh expansion relates to the rate of change in the magnitude of adjacent element face areas or volumes. The mesh expansion factor is the ratio of largest to smallest sector volumes for each control volume. The concept of mesh orthogonality relates to how close the angles between adjacent element faces or adjacent element edges are to some optimal angle (90° for quadrilateral faced elements in our study). The acceptable ranges for these two measures are presented in Table. 5.1. Values outside of the suggested acceptable range will increase the discretization error. Poor convergence and divergence can be expected under these conditions (Reference: ANSYS User Guide).

Table 5.1 Acceptable ranges of mesh quality measures in CFX

Mesh quality measure	Acceptable range
Orthogonality angle	$> 20°$
Expansion factor	< 20

(a) Mesh expansion factor

Figure 5.4 shows the undeformed mesh and the corresponding contour of the mesh expansion factor, used to study the flow over a flexible hydrofoil with u_0= $15m/s$. The mesh expansion factors for the deformed mesh with different stiffness model exponents are shown in Fig. 5.5.

It can be observed that the expansion factor of the initial mesh is almost 1 everywhere through the domain. After the deformation of the hydrofoil, the expansion factor range does not change noticeably. This may be explained by the fact that care was taken to generate the initial mesh with an acceptable range for the expansion factor. As will be investigated

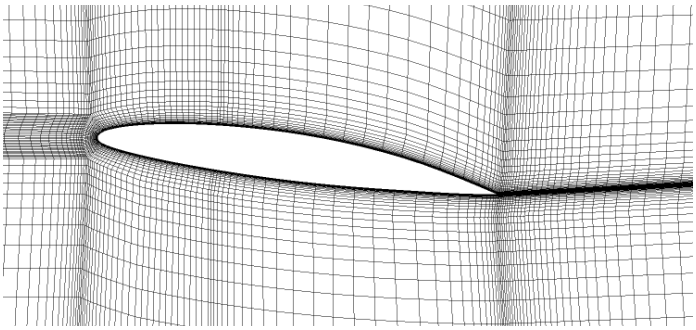

(a) Undeformed mesh

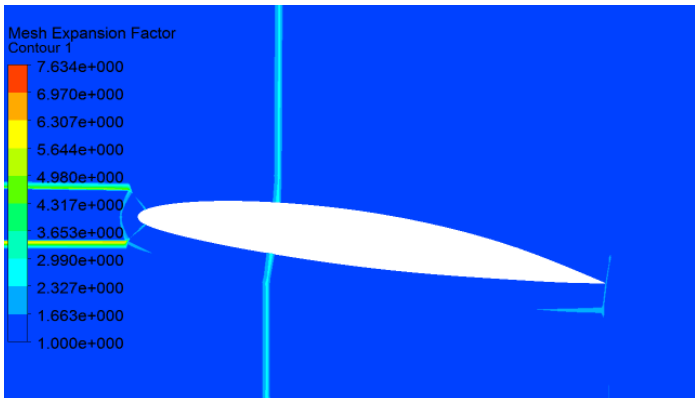

(b) Expansion factor

Figure 5.4 Undeformed mesh and the expansion factor, u_0= $15m/s$

in Chapter 6, the most noticeable DOFs for this hydrofoil set-up are the span-wise upward bending and the clockwise twisting deformation which physically, do not significantly change the expansion factor of the initial undeformed mesh. For this reason, the mesh expansion factor cannot be considered as a determining measure for the mesh quality in the present study and hence, we will investigate the mesh orthogonality angle in the following section which seems to be more important, particularly to determine the mesh quality after the twist deformation of the foil.

(b) Mesh orthogonality angle

The initial and deformed mesh and the corresponding orthogonality angles will be studied for three different test cases of flexible hydrofoils subjected to flow with u_0= $5m/s$, $15m/s$ and $20m/s$.

(a) C_{stiff}=0.5

(b) C_{stiff}=2

(c) C_{stiff}=10

(d) C_{stiff}=20

Figure 5.5 Effects of the stiffness model exponent, C_{stiff}, on the expansion factor of the deformed mesh for flows with u_0= $15m/s$

test case (1): u_0= **5**m/s

Figure 5.6 shows the undeformed mesh and the corresponding orthogonality angle contour, used to study the flow over flexible hydrofoils with u_0= $5m/s$. It is observed that the initial mesh has been generated with an acceptable orthogonality angle range of above ≈70°. Figure

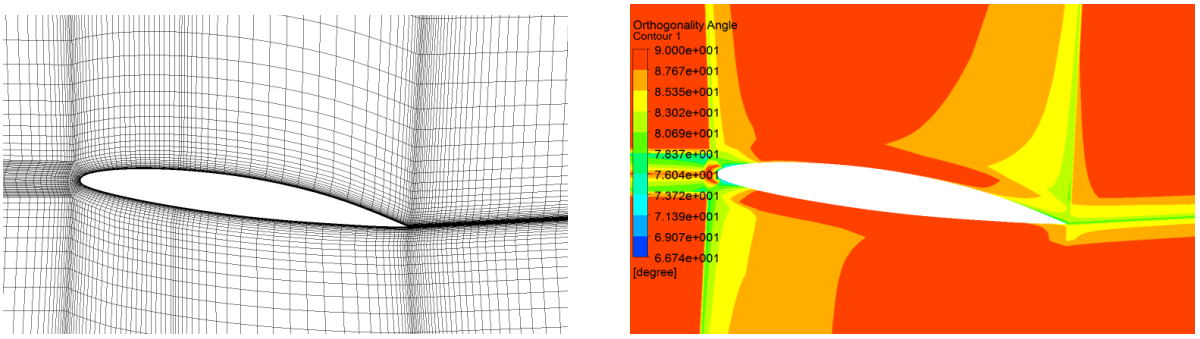

(a) Undeformed mesh (b) Orthogonality angle

Figure 5.6 Undeformed mesh and the orthogonality angle, u_0= $5m/s$

5.7 shows the deformed mesh and the orthogonality angle for the flexible hydrofoil subjected to flow with u_0= $5m/s$, using the default value of the stiffness model exponent in CFX, C_{stiff} = 2.0. It is shown in Fig. 5.7 that the configuration of the deformed mesh and

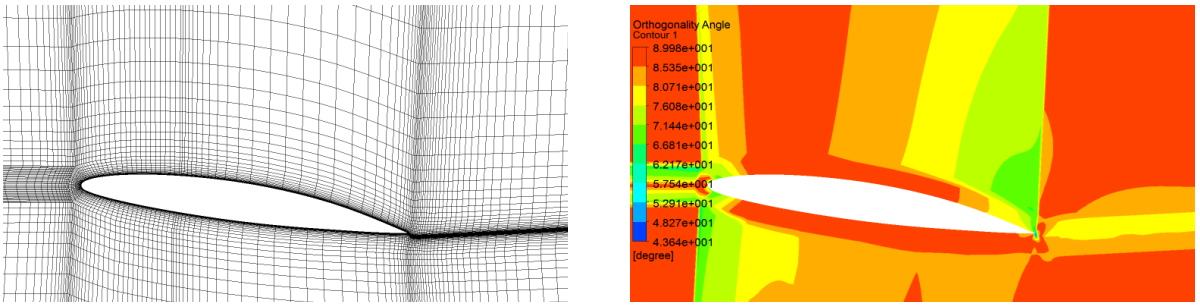

(a) Deformed mesh (b) Orthogonality angle, C_{stiff} = 2

Figure 5.7 Deformed mesh and the orthogonality angle, increasing the stiffness near small volumes with C_{stiff} = 2, u_0= $5m/s$

the orthogonality angle range for the test case with u_0= $5m/s$ is very similar to that of the undeformed mesh in Fig. 5.6, because of the low flow-induced deformations due to low hydrodynamic loading in this operating condition. The only noticeable difference is in the region near the trailing edge, where a decrease in the orthogonality angle is observed. As the comparison of the undeformed and deformed mesh near the sharp trailing edge in Fig.

5.8 shows, the elements in the wake region are unable to follow the upward movement of the hydrofoil and interfacial elements. The elements near the trailing edge should be stiffer so that the nodes in regions of high stiffness move together (that is, there is little relative motion).

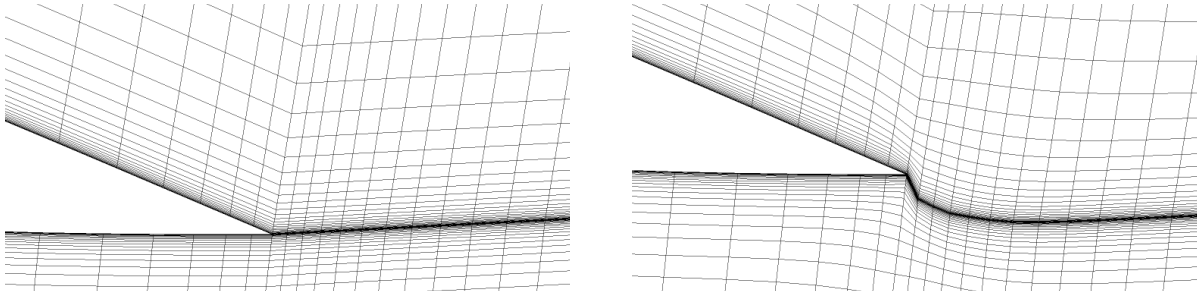

(a) Undeformed mesh (b) Deformed mesh, $C_{stiff} = 2$

Figure 5.8 Comparison of the undeformed and deformed mesh near the trailing edge, $C_{stiff} = 2$, $u_0 = 5m/s$

It is shown in Figs. 5.9 and 5.10 that increasing the stiffness model exponent to $C_{stiff} = 10$ retains the mesh quality after the deformation. The nodes in the trailing edge region with high stiffness move together and there is little relative motion.

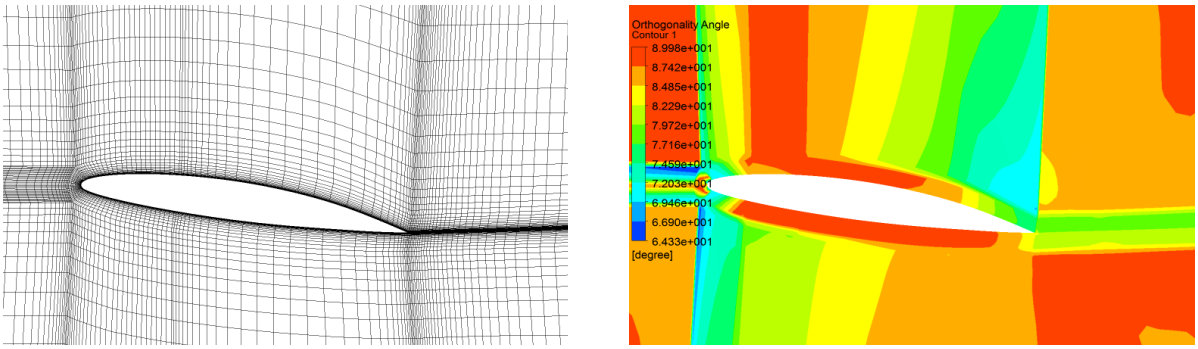

(a) Deformed mesh (b) Orthogonality angle, $C_{stiff} = 10$

Figure 5.9 Deformed mesh and the orthogonality angle, increasing the stiffness near small volumes with $C_{stiff} = 10$, $u_0 = 5m/s$

In conclusion, a variable mesh stiffness with the stiffness model exponent of $C_{stiff} = 10$ is used in the test case of a flexible foil at $\alpha = 8°$ subjected to flow with $u_0 = 5m/s$. This mesh is used for the sake of validation of the results and shows very good agreement with the experimental data, as will be discussed in the next chapter.

It has to be mentioned that, as discussed earlier, an acceptable initial mesh with its specific

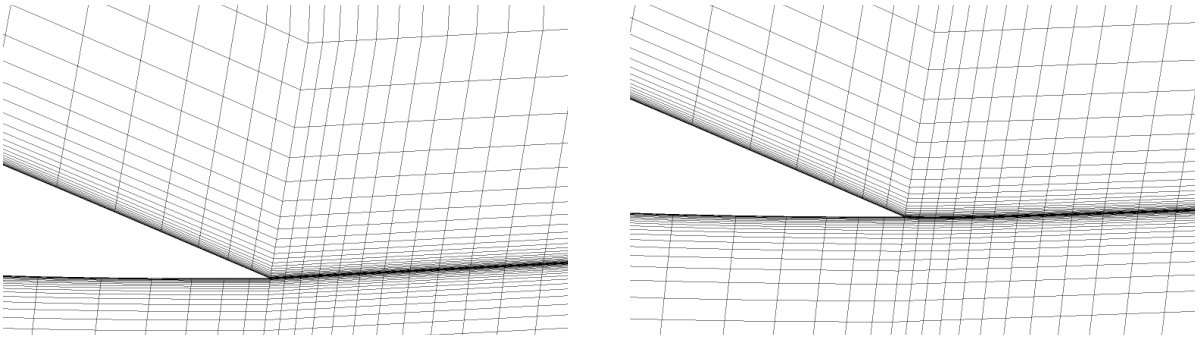

(a) Undeformed mesh (b) Deformed mesh, $C_{stiff} = 10$

Figure 5.10 Comparison of the undeformed and deformed mesh near the trailing edge, $C_{stiff} = 10$, $u_0 = 5m/s$

mesh deformation settings for a specific test case, might not be appropriate for another test case with different operating conditions.

test case (2): $u_0 = \mathbf{15}m/s$

In this section, we will use the initial mesh, shown in Fig. 5.6, to investigate the mesh quality in the test case with $u_0 = 15m/s$. Obviously, the higher hydrodynamic loading in this case leads to higher flow-induced deformations compared to the test case (1).

Figure. 5.11 shows the deformed mesh and the orthogonality angle for the test case (2) with $C_{stiff} = 2.0$, which is the default value in CFX, as well as the contours of the orthogonality angle for this case. The minimum orthogonality angle of the mesh in the regions near trailing edge is $\approx 2^\circ$ which indicates that the quality of mesh is not acceptable.

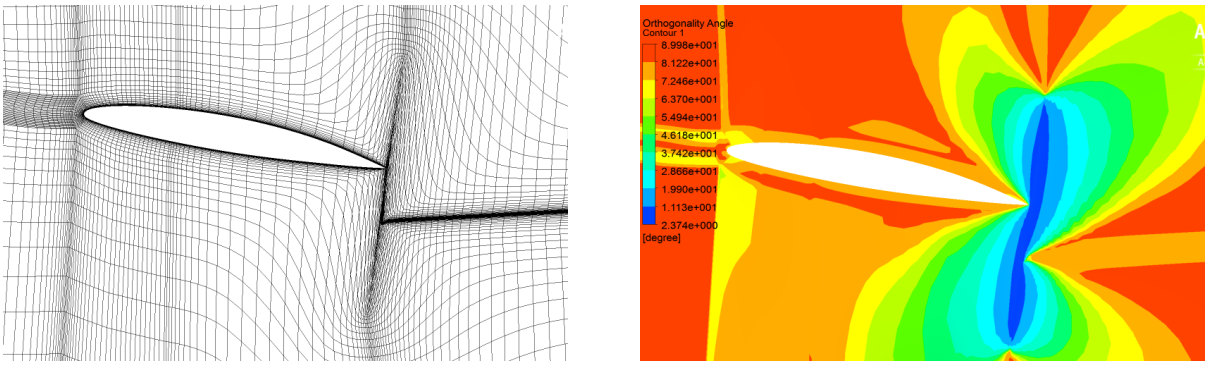

(a) Deformed mesh (b) Orthogonality angle, $C_{stiff} = 2$

Figure 5.11 Deformed mesh and the orthogonality angle, increasing the stiffness near small volumes with $C_{stiff} = 2$, $u_0 = 15m/s$

By decreasing the stiffness model exponent to C_{stiff}=1, negative volume elements appear near the foil trailing edge, as shown in Fig. 5.12, the simulation crashes and hence, the results are not reliable. The contours of the orthogonality angle in Fig. 5.12 show the poor mesh quality in this case. The configuration of the deformed mesh for both cases above,

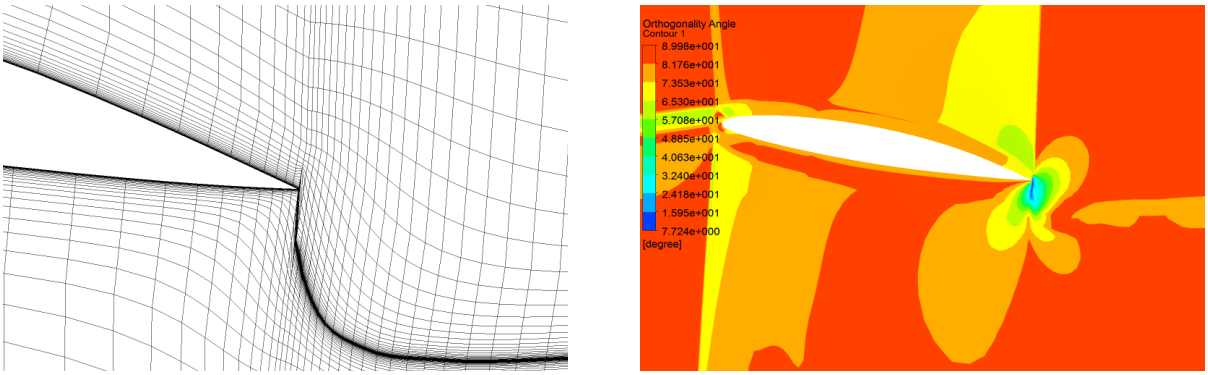

(a) Deformed mesh (b) Orthogonality angle, $C_{stiff} = 1$

Figure 5.12 Deformed mesh and the orthogonality angle, increasing the stiffness near small volumes with $C_{stiff} = 1$, u_0= $15m/s$

$C_{stiff} = 1$ and 2, shows that the elements in the wake region are unable to follow the upward movement of the hydrofoil and interfacial elements, as for the test case (1).

Figure 5.13 shows that by increasing the stiffness model exponent to $C_{stiff} = 10$, the orthogonality angle ranges between ≈50° and 90°. This figure illustrates that higher mesh stiffness is particularly useful to preserve the mesh distribution (and quality) near the sharp trailing edge.

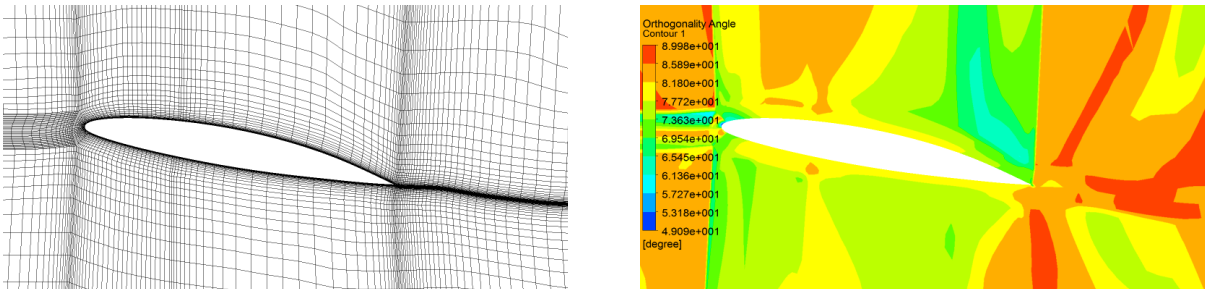

(a) Deformed mesh (b) Orthogonality angle, $C_{stiff} = 10$

Figure 5.13 Deformed mesh and the orthogonality angle, increasing the stiffness near small volumes with $C_{stiff} = 10$, u_0= $15m/s$

Figure 5.14 shows that further increase in the stiffness model exponent to $C_{stiff} = 20$, leads to low orthogonality angles of ≈16° near the leading edge, which is less than the acceptable

range of 20°. By setting the stiffness model exponent to $C_{stiff} = 30$, negative volume elements appear near the leading edge and as a consequence, the simulation crashes after a few iterations.

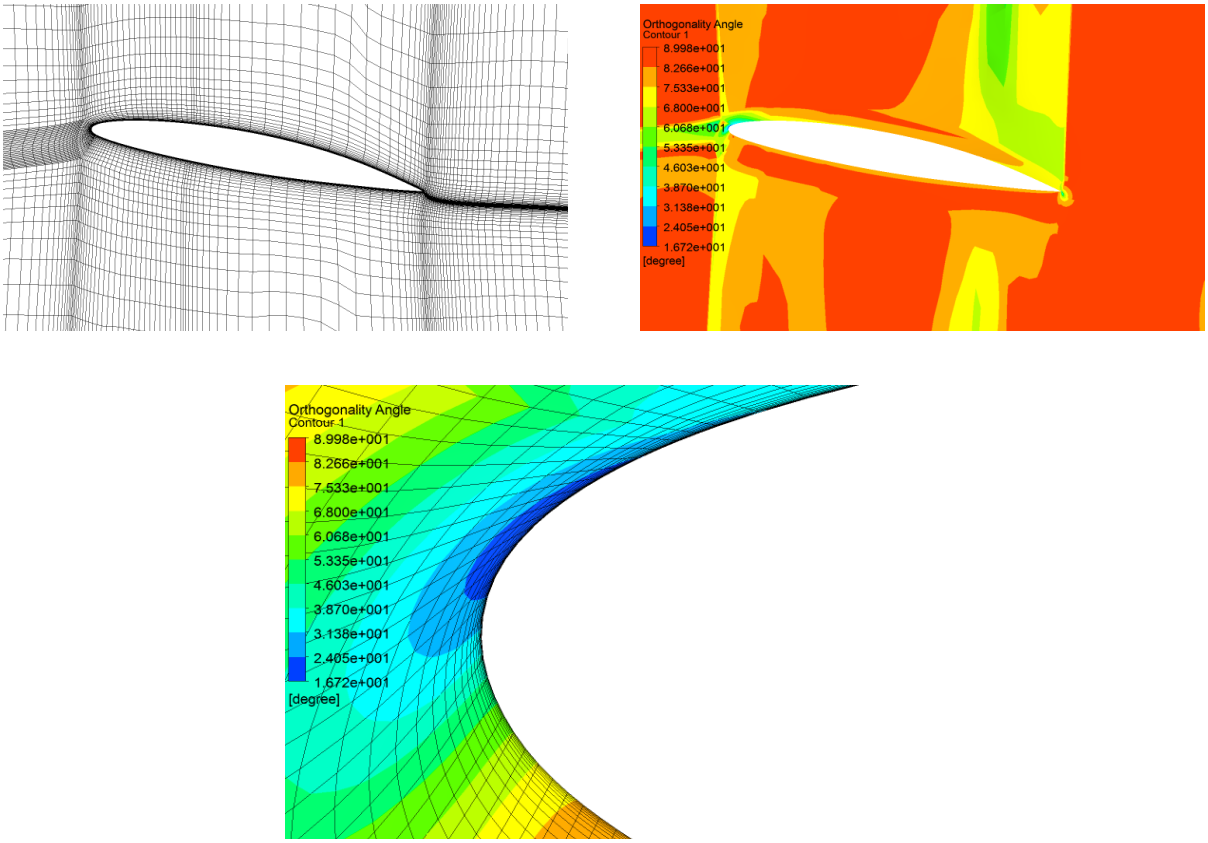

Figure 5.14 Deformed mesh and the orthogonality angle, increasing the stiffness near small volumes with $C_{stiff} = 20$, u_0= $15m/s$

In conclusion, the optimum stiffness model exponent of $C_{stiff} = 10$ is chosen for the simulation of flexible foil at α= 8° subjected to flow with u_0= $15m/s$, which mitigates the distortion of small volume elements near the leading edge and in the wake region.

For higher values of inlet velocities, the flexible hydrofoil undergoes higher deformation and as a consequence, different settings might be needed to avoid highly distorted elements. This will be verified in the following section.

test case (3): u_0= **20**m/s

Based on the conclusion of the test case (2), we will use the initial mesh shown in Fig. 5.6 with a stiffness model exponent of $C_{stiff} = 10$ to investigate the quality of the deformed mesh

for test case (3) with u_0= 20m/s. Figure 5.15 shows the deformed mesh and the orthogonality angle for this test case with $C_{stiff} = 10$. It is shown that due to higher hydrodynamic loading and higher twist deformation of the foil in this case, the minimum orthogonality angle near the leading edge is less compared to the test cases (1) and (2). However, it is still within the acceptable range and hence, this mesh can also be used for the investigations of flow with u_0= 20m/s.

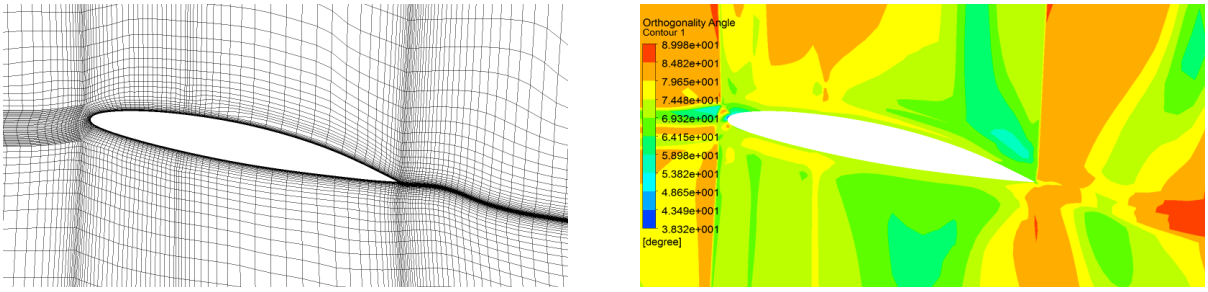

(a) Deformed mesh (b) Orthogonality angle, $C_{stiff} = 10$

Figure 5.15 Deformed mesh and the orthogonality angle, increasing the stiffness near small volumes with $C_{stiff} = 10$, u_0= 20m/s

5.1.4 Time step setting

According to the physics of the problem at the mentioned operating conditions, the hydrofoil initially oscillates as water flows and finally damps to a steady-state position. The present study uses a coupled transient structural and CFD model.

The selection of an appropriate time step size is essential in order to obtain good convergence rates for the simulation and to accurately resolve transient details and capture the important features. The time step size Δt has to be fine enough to ensure a mean CFL number $u_0\Delta t/\Delta x$ around 1.0, where Δx is the average cell size in the chord-wise direction. Therefore, the time step size in this study is chosen to be between $\Delta t = 1 \times 10^{-4}$ and $\Delta t = 1 \times 10^{-5}$, for flows over rigid hydrofoils with $u_0 = 5m/s$ to $u_0 = 25m/s$, respectively.

For the test cases of flow over flexible hydrofoils, the above time step sizes lead to transient start-up convergence problems and solver failure. This is because the hydrofoil made of highly flexible material undergoes large deformations. Our strongly-coupled FSI approach, iterates within each time-step. At each time-step, once the new solid position is obtained from the structural calculations, the fluid flow and the corresponding mesh has to be deformed to conform to the new solid position. If the time step is too small, for a given deformation in each time step, the fluid does not have enough time to respond and the mesh does not have

enough time to conform to the updated structural position. Hence, more time is required for the fluid flow to evolve between the subsequent structural positions. For this reason, a larger time step size of $\Delta t = 1 \times 10^{-3}$ is chosen in the case of flexible hydrofoils. The results obtained from the simulations with this time step show very good agreement with the experimental data, as will be discussed in Section 5.5. Furthermore, from a physical standpoint at the given operating conditions, the problem at hand does not exhibit noticeable transient features, such as large amplitude vibrations and unsteady wake patterns. That is why the choice of larger time step size in the simulation of flow over flexible hydrofoil at the operating conditions in the present study does not affect the accuray of the results.

5.1.5 Solver controls

In all the fluid computations, second order schemes are used to calculate the spatial derivatives in the finite volume discretization. The Second Order Backward Euler scheme is used for the time integration which is an implicit time-stepping scheme. This scheme is second-order accurate and is generally recommended for most transient applications in ANSYS CFX.

5.2 Validation of the viscous fluid solver

The viscous fluid solver is validated by comparing the present numerical results with previous experimental measurements for a NACA0012 airfoil. Two sets of experimental data are used in this section:

- Pressure coefficients for airfoils at incidence angles of α= 0°, 10° and 15° with a Reynolds number of $Re = 2.88 \times 10^6$ taken from Ref. (Gregory and O'Reilly, 1970), and
- Lift and drag coefficients for airfoils at various incidence angles with Reynolds numbers of $Re = 2 \times 10^6$, $Re = 4 \times 10^6$ and $Re = 6 \times 10^6$ taken from Ref. (Ladson, 1988).

Figure 5.16 shows the comparison between the computed and measured pressure coefficient, $C_p = (p - p_0)/(0.5\rho_f u_0^2)$, on the airfoil surfaces at $Re = 2.88 \times 10^6$ for incidence angles of α= 0°, 10° and 15°, where p_0 is the absolute tunnel pressure. In this figure, x/c=0 is the hydrofoil leading edge (LE) position and x/c=1 is the trailing edge (TE) position. Good agreement is observed in all the cases and it is shown that the present viscous fluid solver is able to resolve the leading edge upper surface pressure peak.

Numerical and experimental lift and drag coefficients at various angles of attack are compared in Fig. 5.17 and 5.18 for $Re = 2 \times 10^6$, $Re = 4 \times 10^6$ and $Re = 6 \times 10^6$.

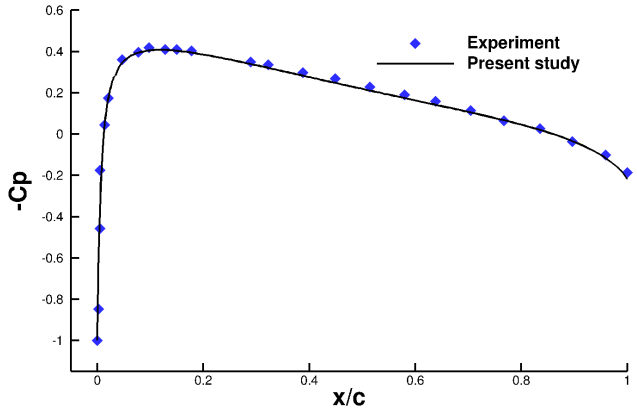

(a) α=0°

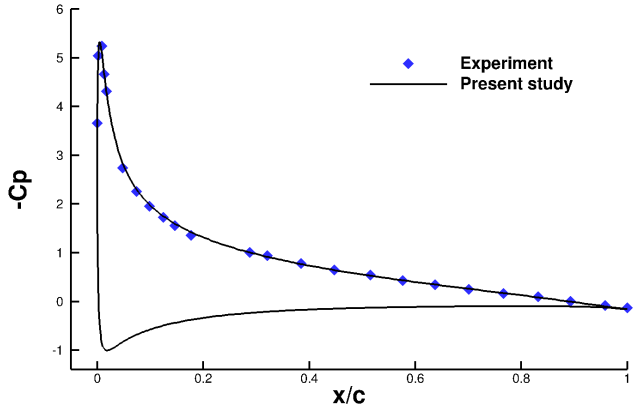

(b) α=10°

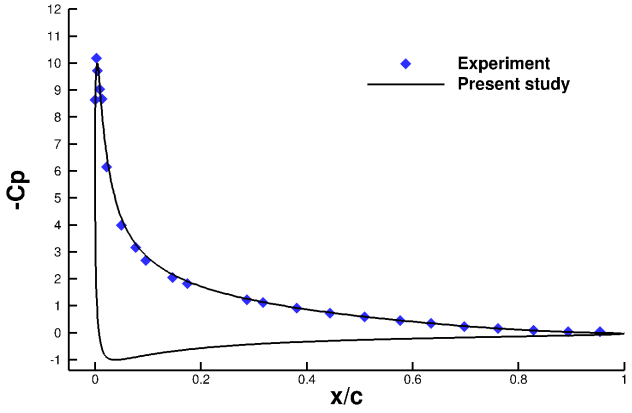

(c) α=15°

Figure 5.16 Comparison of experimental (Gregory and O'Reilly, 1970) and numerical pressure coefficient, C_p, on a NACA0012 foil for Reynolds number of $Re = 2.88 \times 10^6$

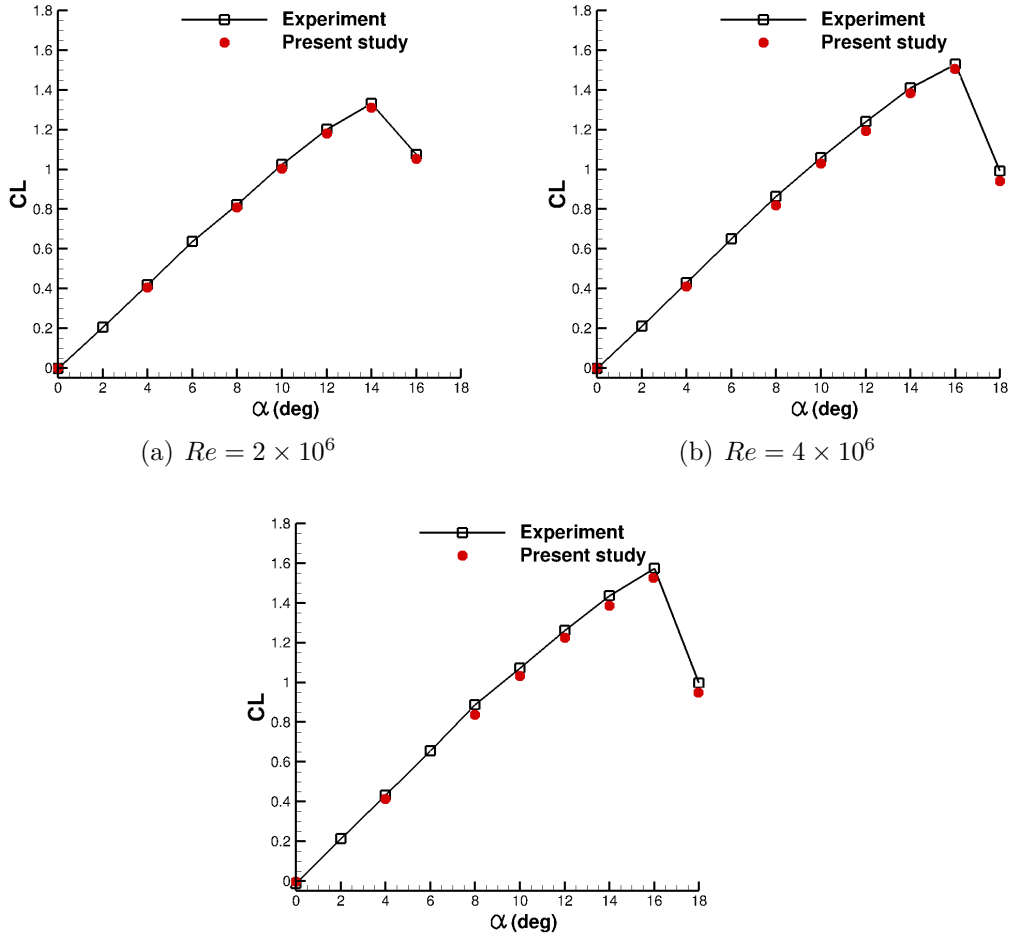

(a) $Re = 2 \times 10^6$

(b) $Re = 4 \times 10^6$

(c) $Re = 6 \times 10^6$

Figure 5.17 Comparison of experimental (Ladson, 1988) and numerical lift coefficients, C_L, on a NACA0012 foil for different Reynolds numbers as a function of the angle of attack, α

It is shown that the present viscous fluid solver is able to correctly predict the lift and drag coefficients. The observed difference between the measured and predicted results at high angles of attack, corresponds to the cases where the flow becomes fully detatch and stall occurs. Due to the flow seperation during stall, the lift coefficient decreases significantly such that the slope of the lift curve becomes negative. Furthermore, a dramatic increase is observed for the drag coefficient, as shown in Fig. 5.18. In this case, the results are no doubt very far from being steady-state any more, and hence, the mean lift and drag coefficients are shown in the diagrams above. It is also shown that for lower Re number of $Re = 2 \times 10^6$, stall occurs at the critical angle of attack of α= 14° while at higher Re numbers, it occurs at α= 16°.

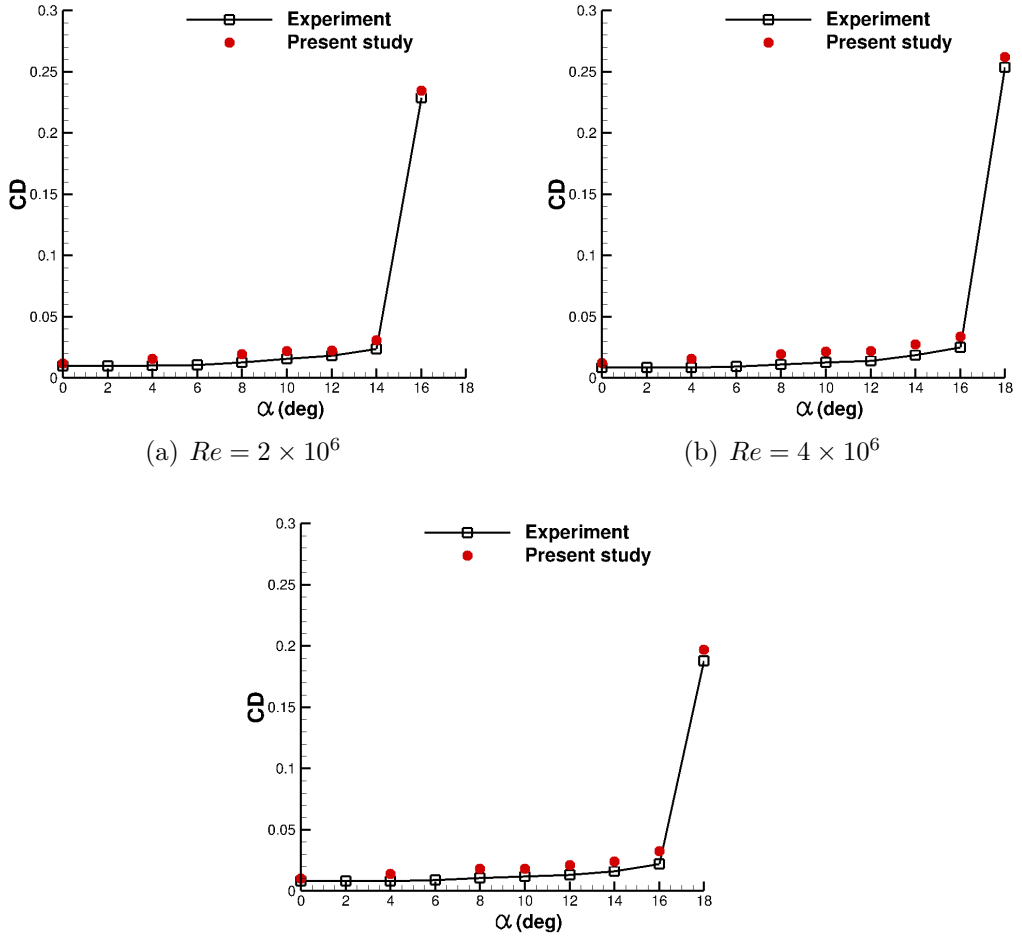

(a) $Re = 2 \times 10^6$

(b) $Re = 4 \times 10^6$

(c) $Re = 6 \times 10^6$

Figure 5.18 Comparison of experimental (Ladson, 1988) and numerical drag coefficients, C_D, on a NACA0012 foil for different Reynolds numbers as a function of the angle of attack, α

5.3 Numerical set-up: structural domain

The ANSYS mesh generator was used to construct the mesh for the solid domain. The solid mesh is composed of 160,000 elements with 400 nodes on the hydrofoil profile and 40 elements in the span-wise direction.

ANSYS has a large library of element types, each of which has a set of degrees of freedom which determines the discipline for which the element is applicable: structural, thermal, electric, etc. The element's degrees of freedom constitute the primary nodal unknowns to be determined by the finite element analysis. The derived results, such as stresses, are computed from these degrees of freedom and hence, the choice of element type is an important step in any ANSYS analysis. The element type should be chosen such that the degrees of freedom are

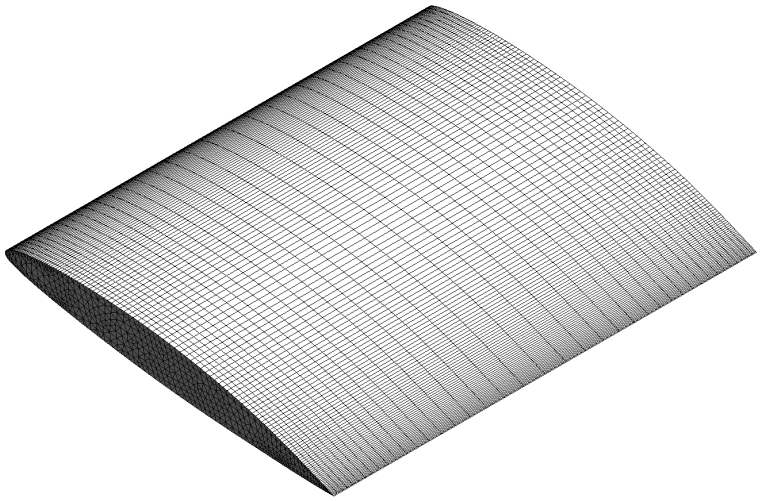

Figure 5.19 The structural mesh used for CSD simulation

sufficient to predict the model's response. Including unnecessary degrees of freedom increases the memory requirements and run time. Similarly, selecting element types with unnecessary features, such as using an element type with plastic capability in an elastic simulation, also unnecessarily increases the running time.

The characteristics of the element types are described in the ANSYS user guide. However, it suffices to mention that in the present study, SOLID185 is used to perform transient structural analysis. This element type is an hexahedral element defined by eight nodes which has plasticity, stress stiffening, large deflection, and large strain capabilities (Reference: ANSYS User Guide).

In ANSYS, the transient structural analysis is used to determine the time-dependent displacements, strains, stresses, and forces in the structure as it responds to the total forces received from the CFD simulation.

5.4 Mesh convergence study

Proper grid refinement is crucial for accurate prediction of turbulent features in the study of hydroelastic response and stability of hydrofoils, particularly in regions where laminar separation occurs, in order to properly capture the rapid transition due to the separation bubble.

Mesh convergence studies are conducted for the case corresponding to a rigid NACA66 hydrofoil at an angle of attack of α=8° in steady flow with u_0= $5m/s$; the relevant experimental data is taken from Ref. (Akcabay et al., 2014). The mesh convergence study is performed

considering three different parameters; Y^+ near the hydrofoil surface, the number of nodes on the hydrofoil profile in the stream-wise direction N_{foil}, and the number of elements on the hydrofoil in the span-wise direction n_{span}. In all the convergence results shown in this subsection, the time step is chosen to be $\Delta t = 1 \times 10^{-4}$.

Figure 5.20 shows the effect of boundary layer resolution, Y^+, on the pressure coefficient, $C_p = (p - p_0)/(0.5\rho_f u_0^2)$, along the free tip of the hydrofoil.

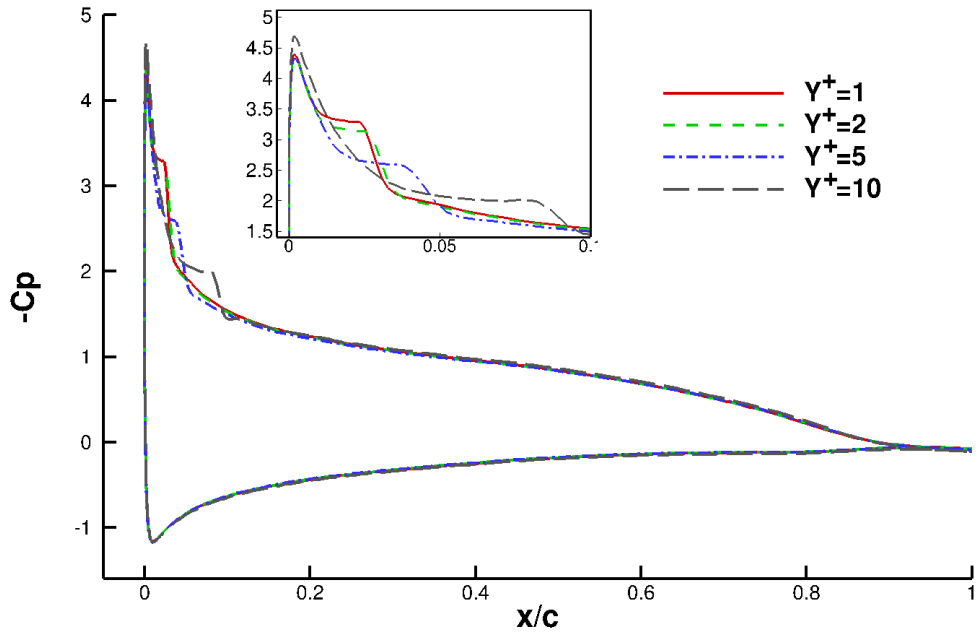

Figure 5.20 Pressure coefficient, C_p, along the hydrofoil surface for the rigid foil at α=8° for different values of Y^+. (N_{foil}=400 and n_{span}=40)

The high pressure gradient near the foil leading edge results in the formation of a laminar separation bubble near the foil leading edge which has an immediate effect on the hydroelastic response of the foil. This figure illustrates how the onset and the amount of flow separation depends on the value of the boundary layer resolution, Y^+. Therefore, Y^+=1 is chosen in the present study in order to fully resolve the boundary layer. It should be noted that the number of nodes on the hydrofoil profile in the stream-wise direction, N_{foil}, is set to 400 and there are 40 elements in the span-wise direction.

The influence of number of nodes on the NACA66 profile, N_{foil}, is depicted in Fig. 5.21. The figure shows that in order to capture the high pressure gradient near the foil leading edge, a sufficient number of nodes is needed in this region.

The computed lift coefficient convergence according to N_{foil} is summarized in Table 5.2. It is shown that C_L converges to its experimental value of C_L=1.065 with an error of less than

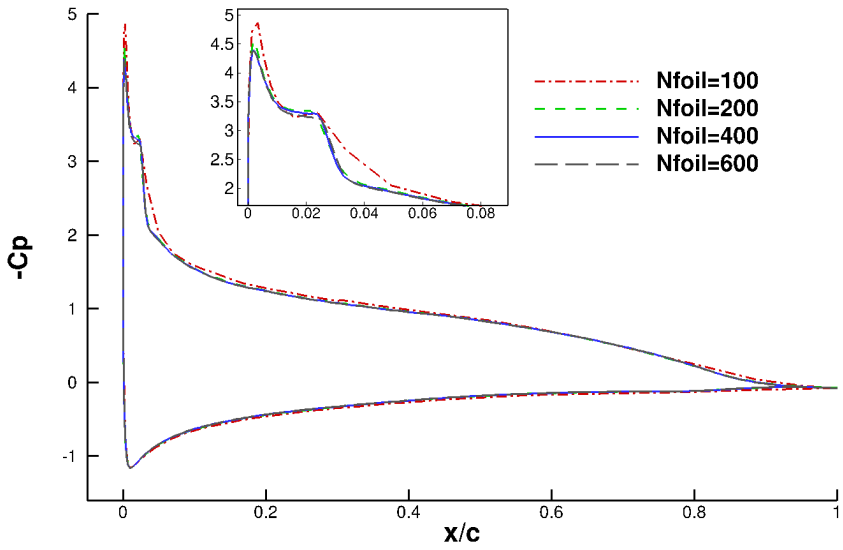

Figure 5.21 Pressure coefficient, C_p, along the foil surface for the rigid hydrofoil at α= 8° for different values of N_{foil}. (Y^+=1 and n_{span}=40)

1% for N_{foil}=400 and above.

The effects of the different numbers of elements on the hydrofoil in the span-wise direction (n_{span}) are also studied and the convergence is shown in Table 5.3. The variation of the hydrodynamic lift coefficient in the span-wise direction confirms the 3D nature of the problem.

It is worth mentioning that different boundary layer resolutions near the channel wall are also studied and Y^+ ≈1 is chosen.

Table 5.2 Lift coefficient convergence as a function of number of nodes on the hydrofoil profile in the stream-wise direction (N_{foil})

N_{foil}	C_L	difference with experiment %
100	1.152	8.1
200	1.085	1.9
400	1.073	0.8
600	1.072	0.7
Experiment (Akcabay et al., 2014)	1.065	-

Table 5.3 Lift coefficient convergence as a function of number of elements in the span-wise direction (n_{span})

n_{span}	C_L	difference with experiment %
20	1.114	4.6
30	1.079	1.3
40	1.073	0.8
50	1.071	0.6
Experiment (Akcabay et al., 2014)	1.065	-

5.5 Validation of the two-way FSI solver

The FSI simulations are validated through comparison with experimental data measured for flow over both rigid and flexible NACA66 hydrofoils at 8° angle of attack in a water tunnel facility at the French Naval Academy by Akcabay et al. (Akcabay et al., 2014). u_0= $5m/s$ is the nominal free stream velocity that yields a moderate Reynolds number of $Re = 0.75 \times 10^6$ in this part of our study.

Figure 5.22 shows a good agreement between the computed and measured (Akcabay et al., 2014) pressure coefficients along the rigid hydrofoil surface at α=8°. However, there were no available experimental data for the leading edge upper surface pressure peak.

The experimentally measured hydrodynamic load coefficients (C_L and C_D) for the rigid hydrofoil and the tip section vertical displacement (δ_y) measured at the leading edge of the flexible hydrofoil are compared with computational values in Table 5.4. These comparisons show that the present numerical results yield a better agreement with the experimental measurements than those obtained by Akcabay et al. (Akcabay et al., 2014) and (Wu et al., 2015). This might be partly due to the 2D flow assumption in these studies, which ignored 3D effects, such as the contributions from the induced drag due to the finite aspect ratio (s/c = 1.27) and the boundary layer effects at the foil root, whereas these are accounted for in the present study. The 2D hydrofoil assumption in Ref. (Akcabay et al., 2014) and neglecting the effects of the fixed root leads to noticeable discrepancies in the magnitudes of the hydrofoil displacement (error of 58% between the experimental and numerical values), while in the present study the difference between the experimental and numerical results for δ_y is $\approx$ 4%. Considering all the structural DOFs, the solution of the complete set of struc-

tural equations and incorporating a two-way FSI coupling method in the current study also provides more accurate results than the loosely coupled method in the studies of Akcabay et al. (Akcabay et al., 2014) and (Wu et al., 2015) who used a simple 2-DOF model to simulate only the tip section bend and twist deformations for the solid domain. Furthermore, although the SST turbulence model has been used in the studies of Akcabay et al. (Akcabay et al., 2014) and (Wu et al., 2015), in the present study this model is coupled with a transition model, whereas no transition modelling has been used in these two references. As mentioned in the previous literature and will be investigated in Section 5.7, the incorporation of transition modeling is highly effective in the accurate prediction of the flow separation, which has immediate effect on the hydrodynamic response of the hydrofoils.

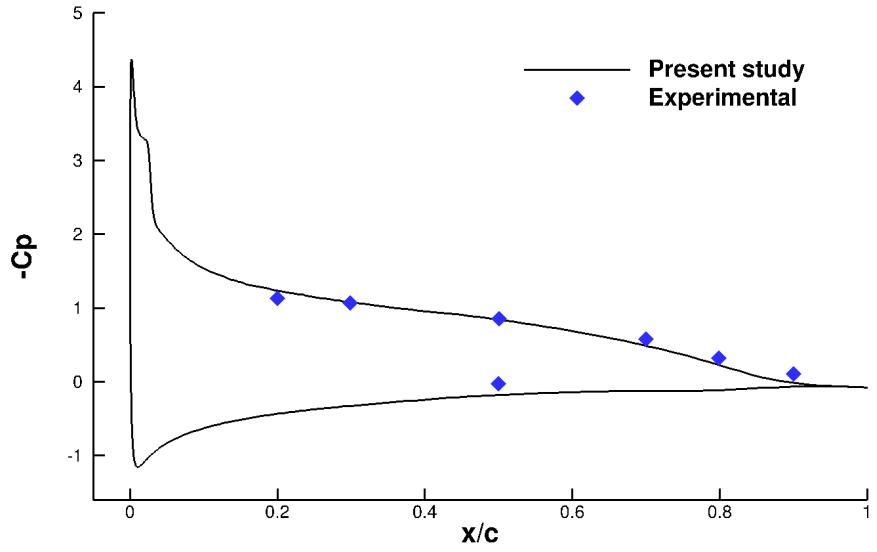

Figure 5.22 Comparison of the experimental (Akcabay et al., 2014) and computational pressure coefficient, C_p, along the free tip of the rigid hydrofoil surface at α=8°

C_L is primarily affected by pressure changes, while C_D is affected by 3D effects such as energy dissipation through the gap and tip vortices. The influence of tip gap flow is neglected in the present study. This could be the reason why there is only a small difference between the measured and computed C_L, while the measured C_D is much higher than the numerical values.

The proposed advanced 3D methodology in the present strongly-coupled two-way FSI simulations, results in more accurate hydrodynamic lift and drag coefficients in comparison with the available numerical results in the above-mentioned references. It has to be mentioned that this comparison, which shows the improvement of the numerical results, has been performed for low-loaded conditions; i.e. u_0=5 m/s, which was the test case in the studies of Akcabay

Table 5.4 Comparison of the experimental (Akcabay et al., 2014) and computational lift and drag coefficients and the tip section displacement for the rigid and flexible hydrofoils at α=8°

		C_L	C_D	$\delta_y(mm)$
Rigid	Experiment (Akcabay et al., 2014)	1.065	0.048	-
	Present study	1.073	0.036	-
	Computation Ref. (Akcabay et al., 2014)	1.19	0.022	-
	Computation Ref. (Wu et al., 2015)	1.15	-	-
Flexible	Experiment (Akcabay et al., 2014)	-	-	3.6
	Present study	1.16	0.029	3.45
	Computation Ref. (Akcabay et al., 2014)	1.22	0.022	1.5
	Computation Ref. (Wu et al., 2015)	1.2	-	2

et al. (Akcabay et al., 2014) and (Wu et al., 2015). However, at highly loaded conditions (u_0= 15 to 25 m/s), where the flow is fully turbulent and the flow detachment and instabilities might occur, the 3D assumption becomes a necessity. In this case, the flow-induced deformation of the flexible hydrofoil becomes high enough to reach instabilities and hence, the accuracy of results becomes more dependent on how strongly the fluid and solid domains are coupled. Therefore, our proposed methodology is clearly able to predict accurate results at highly loaded operating conditions.

Based on these good agreement with experiment, from now on, the analysis will be based on numerical simulations which are assumed to correctly reproduce the experimental data. The model will be used to study the hydroelastic response of the hydrofoil subjected to flows with higher Reynolds numbers in the next chapter.

5.6 Comparison of one-way and two-way coupling methods for FSI analysis of the flexible hydrofoils

In this section, one-way and two-way coupling methods are compared for FSI analysis of the hydrofoil. For one-way coupling calculations, once the flow field is computed, only the fluid pressure acting on the structure is transferred to the structural solver. For two-way-coupling

calculations, the displacement of the structure is also transferred back to the fluid solver.

To better understand the difference between the two methods, only the flexible hydrofoil at a high angle of attack, α= 8°, will be studied. The hydrofoil is subjected to flows with u_0= $5m/s$, $10m/s$, $15m/s$, $20m/s$ and $25m/s$.

The total displacements of the hydrofoil, computed with one-way and two-way coupling methods, are compared in Fig. 5.23. Figure 5.24 shows the comparison between the vertical tip section displacement, δ_y, measured at the leading edge of the flexible hydrofoil at α= 8°, subjected to flows with u_0= $5m/s$, $10m/s$, $15m/s$, $20m/s$ and $25m/s$, for one-way and two-way coupling methods. It is shown that higher Re number flows lead to higher deformation in the foil due to higher hydrodynamic loading. Comparison between the displacements obtained from the one-way and two-way coupling methods shows that at lower loaded conditions, such as u_0= $5m/s$ and $10m/s$, the structural deformations are small and hence, the result of both coupling methods are almost similar. However, a larger difference is observed at higher loading conditions where the structure undergoes larger deformations. Under these conditions, there is a strong relationship between the two fields that are coupled, and hence, two-way FSI needs to be undertaken.

The velocity contours are also compared for one-way and two-way coupling methods in Fig. 5.25. At low loading conditions, the flow pattern computed with both one-way and two-way coupling methods are almost similar, except that the flow velocity near the leading edge is higher in the two-way approach due to the foil higher deformation. As mentioned before, the difference is significantly more noticeable at high loading conditions, in which the structural deformation is significant and strongly affects the flow field. As shown in Fig. 5.25(h), for a flexible hydrofoil subjected to flow with a velocity of u_0= $20m/s$, high hydrodynamic loading leads to high deformation of the foil, and as a result, the flow becomes fully detached and stall occurs. This will be discussed in the next chapter in more detail. It is clearly observed that stall is not captured by the one-way coupling method.

The lift and drag coefficients are also computed with both one-way and two-way coupling methods and compared in Fig. 5.26. It is shown that for one-way coupling method, the difference in the hydrodynamic coefficients caused by different Re numbers is much lower than the two-way coupling method. It is also shown that at high loading conditions, the hydrodynamic coefficients obtained from the two-way simulations are higher than those from one-way simulations due to the higher deformation. As shown in this figure and will be discussed in the next chapter, when stall occurs in the two-way FSI simulations of a flexible foil subjected to a flow with u_0= $20m/s$, a dramatic increase is observed for the drag coefficient due to the fully detached flow over the foil. In this case, the lift coefficient decreases significantly.

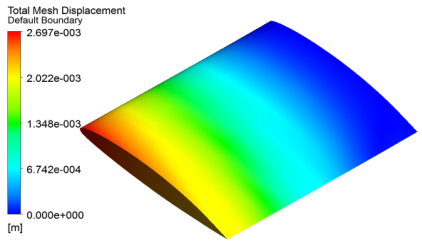

(a) one-way, u_0= $5m/s$

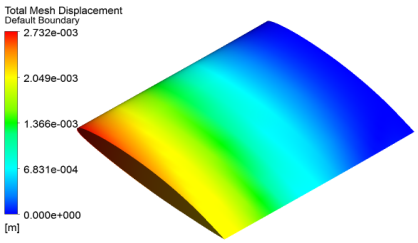

(b) two-way, u_0= $5m/s$

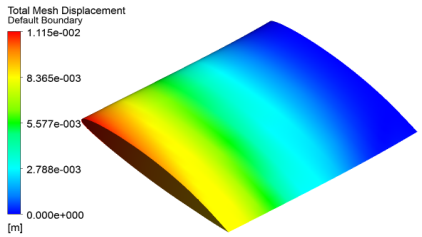

(c) one-way, u_0= $10m/s$

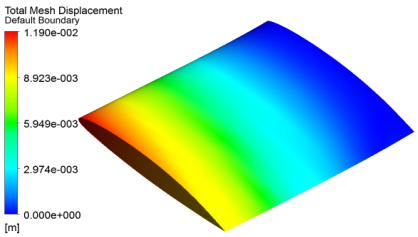

(d) two-way, u_0= $10m/s$

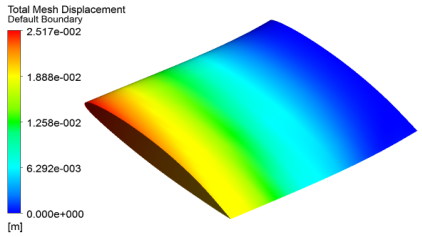

(e) one-way, u_0= $15m/s$

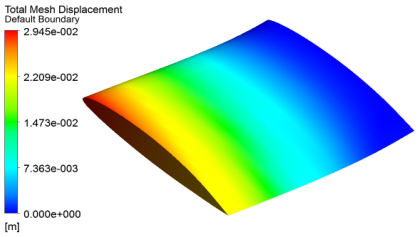

(f) two-way, u_0= $15m/s$

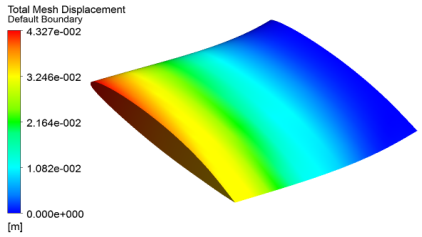

(g) one-way, u_0= $20m/s$

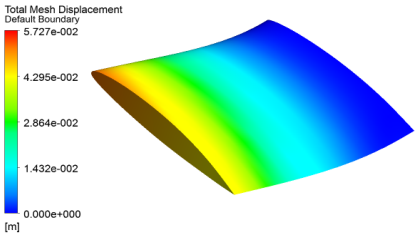

(h) two-way, u_0= $20m/s$

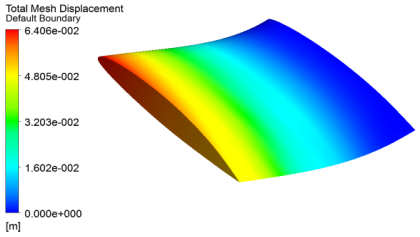

(i) one-way, u_0= $25m/s$

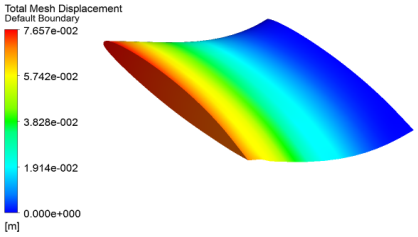

(j) two-way, u_0= $25m/s$

Figure 5.23 Comparison of the total displacement for the flexible hydrofoil at $\alpha = 8°$ with one-way (left column) and two-way (right column) coupling methods

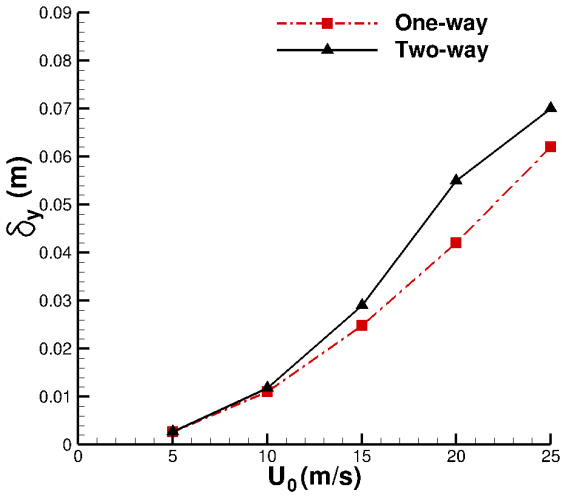

Figure 5.24 Comparison of the vertical tip section displacement, δ_y, for the flexible hydrofoil at $\alpha = 8°$ with one-way and two-way coupling methods

For moderate to high Re number flows, high hydrodynamic loading conditions result in large structural deformations that strongly affects the flow field. In other words, the structural analysis produces results that, when applied as loads in the fluid analysis, significantly affects the flow solution. It can be concluded that two-way FSI needs to be incorporated to accurately capture and analyze the deformation-dependant phenomena in the flow, such as separation and stall.

The fluid-structure problem is solved with a finite volume technique using the CFD code CFX, for the fluid, and a finite element code using the CSD code ANSYS, for the structure. The available coupling capability enables CFX to work with the ANSYS Mechanical solver within an ANSYS Multi-field simulation. During coupled simulations, the ANSYS CFX and Mechanical solvers execute the simulation through a sequence of multi-field steps, each of which consists of one or more coupling iterations. In the proposed strongly-coupled FSI algorithm, the results of the CFD model are transferred to the structural part whereas the subsequently calculated displacements at the interface are transferred back to the CFD analysis through mesh deformation.

5.7 Transition modelling: effects on laminar to turbulent transition

It has been discussed earlier that the hydroelastic response of a flexible hydrofoil is highly affected by the turbulence predictions and boundary layer detachment at high Reynolds

(a) one-way, u_0= $5m/s$

(b) two-way, u_0= $5m/s$

(c) one-way, u_0= $10m/s$

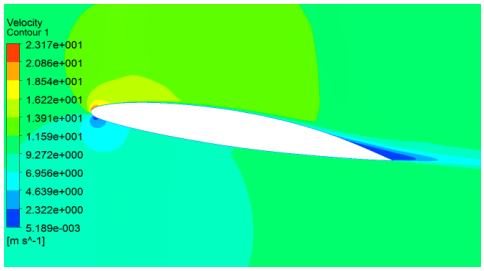

(d) two-way, u_0= $10m/s$

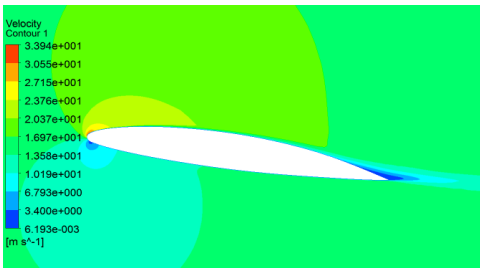

(e) one-way, u_0= $15m/s$

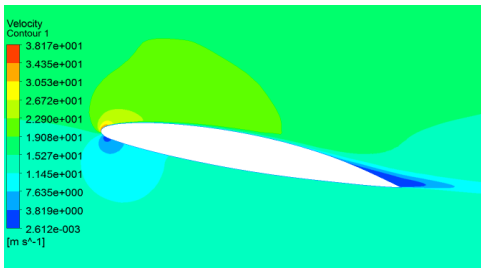

(f) two-way, u_0= $15m/s$

(g) one-way, u_0= $20m/s$

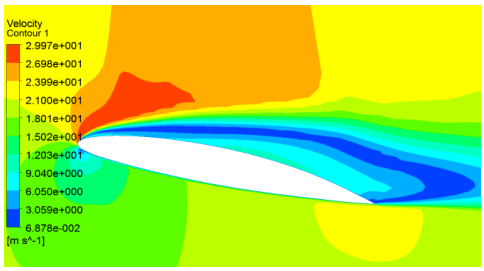

(h) two-way, u_0= $20m/s$

(i) one-way, u_0= $25m/s$

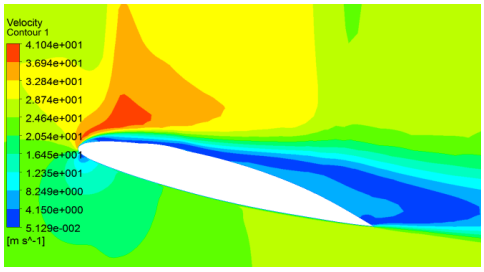

(j) two-way, u_0= $25m/s$

Figure 5.25 Comparison of the velocity contours for the flexible hydrofoil at $\alpha = 8°$ with one-way (left column) and two-way (right column) coupling methods

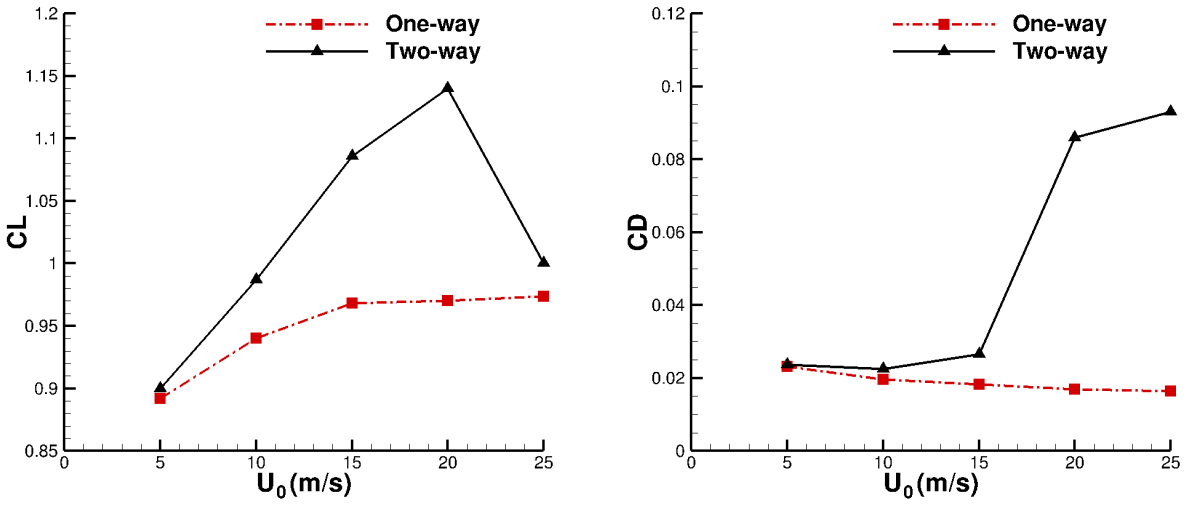

(a) (b)

Figure 5.26 Comparison of (a) lift coefficient (b) drag coefficient of flexible hydrofoils at $\alpha = 8°$ with one-way and two-way coupling methods

numbers. The current simulations use the SST turbulence model which has been shown to be accurate for boundary layer detachment prediction and turbulence behaviour of flexible foils at high Reynolds numbers. To accurately capture the major transition effects in our study, the SST turbulence model is coupled with the "Gamma Theta" transition model. Incorporation of transition modeling has been shown to be highly effective in the prediction of the onset of the flow separation under adverse pressure gradient conditions.

The aim of this section is to investigate the effects of transition modelling on laminar to turbulent transition over the hydrofoil. For this purpose, we will compare the results for a case of separation-induced transition, with and without using the transition model.

To better understand the effect of transition modelling, the laminar to turbulent transition point is analyzed. The transition point can be approximated as the point where the skin friction coefficient is equal to zero (Menter et al., 2006; Ducoin and Young, 2013).

Figures 5.27 and 5.28 show the distribution of the skin friction coefficient, C_f, on the suction side of the flexible hydrofoil at α=6° subjected to flows with velocities of u_0= $20m/s$ and $25m/s$. The distribution of C_f is compared in these figures for the simulations with and without incorporating the transition modeling coupled to the turbulent modeling.

Figure 5.27 shows that the flow separation near the trailing edge has been captured with and without using the transition model at x/c≈0.85, where the skin friction coefficient is equal to zero. With the use of transition modeling, the laminar saparation bubble near the

leading edge is also captured at x/c≈0.01. However, without using the transition modeling, the laminar saparation bubble near the leading edge is not captured.

Furthermore, the distribution of C_f shown in Fig. 5.28 and the comparison of the velocity countours shown in Fig. 5.29 show that the incorporation of transition modeling in the case of flow with u_0= $25m/s$, forces globally turbulent flow on the suction side of the flexible hydrofoil, the flow becomes fully detached and the hydrofoil experiences the well-known phenomenon of stall. However, the SST model without the transition model can only capture the transition point near the trailing edge (x/c≈0.78).

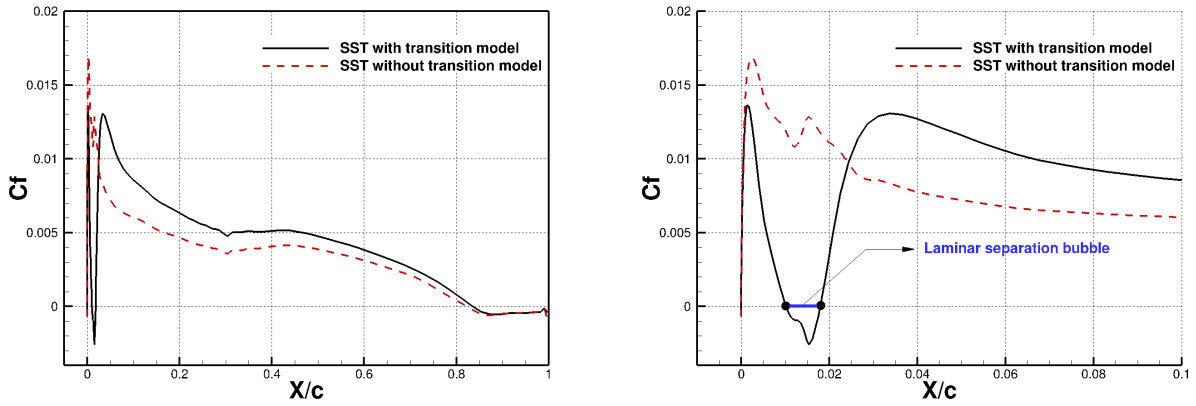

(a) the full-extend of the C_f distribution

(b) a close-up near the foil leading edge

Figure 5.27 Skin friction coefficient along the hydrofoil upper surface for the flexible hydrofoil at α=6° with u_0= $20m/s$

The effect of laminar-to-turbulent transition modelling was investigated for a case of separation-induced transition corresponds to a flexible hydrofoil at high hydrodynamic loading condition, for which no experimental data is available. Hence, although a significant different was observed between the cases with and without transition modelling, the reliability of the results may not be justified. Therefore, the investigation of laminar-to-turbulent transition modeling will be performed for a separation-induced transition case with available experimental data. We will choose a case corresponds to the flow over a NACA0012 airfoil at an incidence angle of α=18° with a Reynolds number of $Re = 4 \times 10^6$ taken from Ref. (Ladson, 1988). This test case has already been validated in Section 5.2.

The lift and drag coefficients are compared for the simulations with and without transition modeling in Table. 5.5. It is shown that the results obtained with the incorporation of transition modeling match the experiments better in comparison to fully turbulent computations.

It is shown in Fig. 5.30(a) that a leading edge vortex develops along the entire foil, which

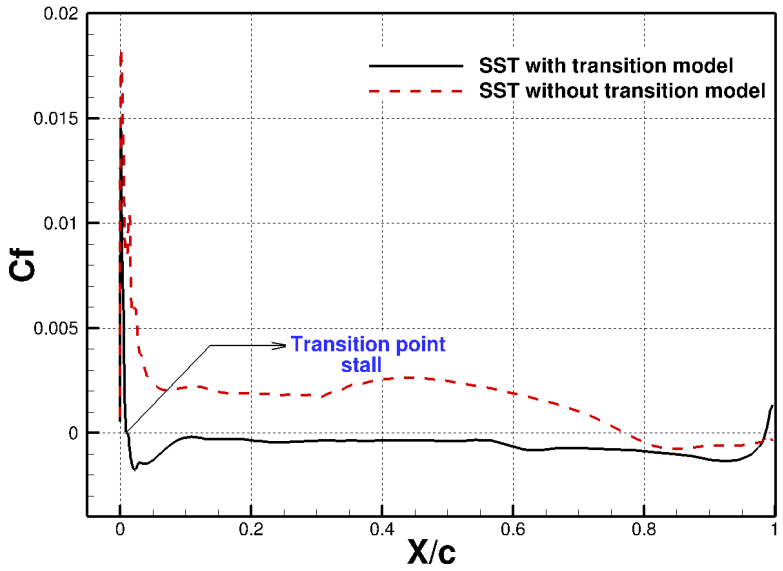

Figure 5.28 Skin friction coefficient along the hydrofoil upper surface for the flexible hydrofoil at α=6° with u_0= 25m/s

Table 5.5 Comparison of the lift and drag coefficients for NACA0012 airfoil at α=18° and $Re = 4 \times 10^6$, with and without transition modeling

	with transition modeling	without transition modeling	experiment
C_L	0.95	0.68	0.99
C_D	0.27	0.19	0.25

sheds partially into the wake and leads to an unsteady flow. The interaction between the clock-wise leading edge vortex with the counter clock-wise trailing edge vortex is observed in this figure. However, the streamlines depicted in Fig. 5.30(b) show that the fully turbulent simulation is not able to accurately predict the flow separation on the foil, which consequently leads to discrepancies in the lift and drag coefficients, as presented in Table. 5.5.

To recapitulate, the SST turbulence model coupled with the "Gamma Theta" transition model in the proposed methodology was shown to be an accurate model for flow separation prediction and turbulence behaviors over the foils.

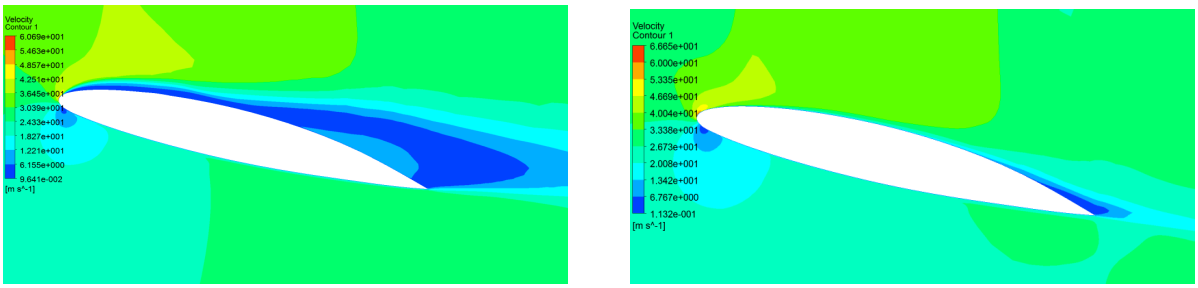

(a) with transition model (b) without transition model

Figure 5.29 Comparison of the velocity contours at the free tip of the flexible hydrofoil at α=6° with u_0= $25m/s$ with and without transition modeling

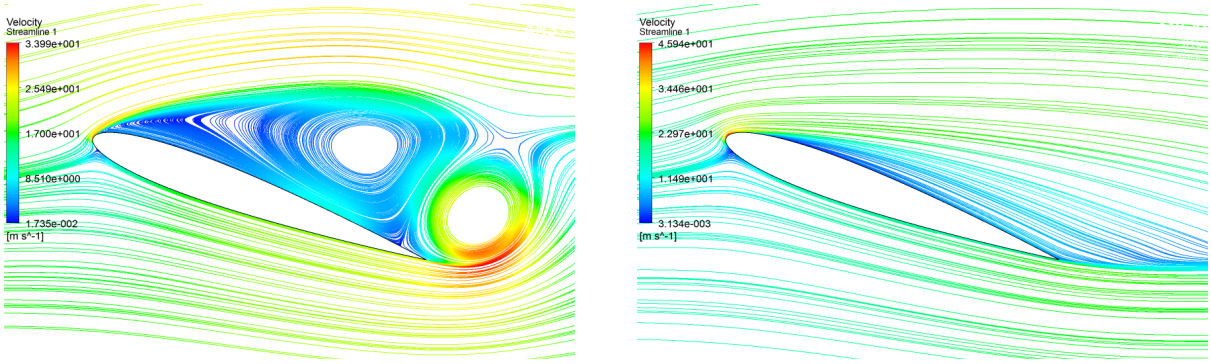

(a) with transition model (b) without transition model

Figure 5.30 Comparison of the streamlines for a NACA0012 airfoil at α=18° and $Re = 4\times10^6$, with and without transition modeling

CHAPTER 6 RESULTS

In this chapter, the hydroelastic response of 3D hydrofoils will be studied at various operating conditions; i.e. different angles of attack and inlet velocities.

To investigate and quantify the effects of hydrofoil flexibility, a solid understanding of the rigid foil dynamics is required. This will be undertaken by comparing the performance of rigid and flexible hydrofoils. For comparison, both rigid and flexible hydrofoils are considered in the same operating conditions and identical initial undeformed geometries.

As discussed in chapter 5, to avoid confinement effects caused by large elastic foil deformations at highly hydrodynamic loaded conditions, the infinite-like boundary fluid domain shown in Fig. 5.1.(b) is used in this chapter.

6.1 Flow-induced deformation of the flexible hydrofoil

The flow-induced displacement of the flexible hydrofoil at α=8° subjected to flow at $Re = 0.75 \times 10^6$ is depicted in Fig. 6.1, which is scaled to enhance legibility. The 3D feature of the foil deformation (fixed at the root and free at the tip) is clearly shown in this figure. It is also shown that the deformation of the hydrofoil near the leading edge is higher than the corresponding value near the trailing edge. This confirms that, as indicated by Ducoin and Young Ducoin and Young (2013), the flexible hydrofoil undergoes a clockwise twist deformation, which increases the effective angle of attack. Furthermore, although the solid equations considering all the DOFs of the domain are fully solved in this study, the span-wise upward bending and the clockwise twisting deformation of the hydrofoil seem to be the most noticeable DOFs for this hydrofoil set-up, as depicted in Fig. 6.2 for the flexible hydrofoil subjected to flow with u_0= $20m/s$. Bending and twist deformation of the hydrofoil are the only DOFs that were considered in Refs. Ducoin and Young (2013); Akcabay and Young (2014); Akcabay et al. (2014); Chae et al. (2013); Wu et al. (2015); Chae et al. (2016).

The variation of vertical tip section displacement, δ_y, measured at the leading edge of the flexible hydrofoil is given in Fig. 6.3 as a function of the initial angle of attack, α. It shows that high loaded conditions, i.e. high angles of attack or high Re number flows, lead to higher displacements of the foil. For instance, the flexible hydofoil initially placed at the angles of incidence of $\alpha = 4°$ and higher, experiences a vertical displacement of more than one half of its chord length when u_0= $25m/s$.

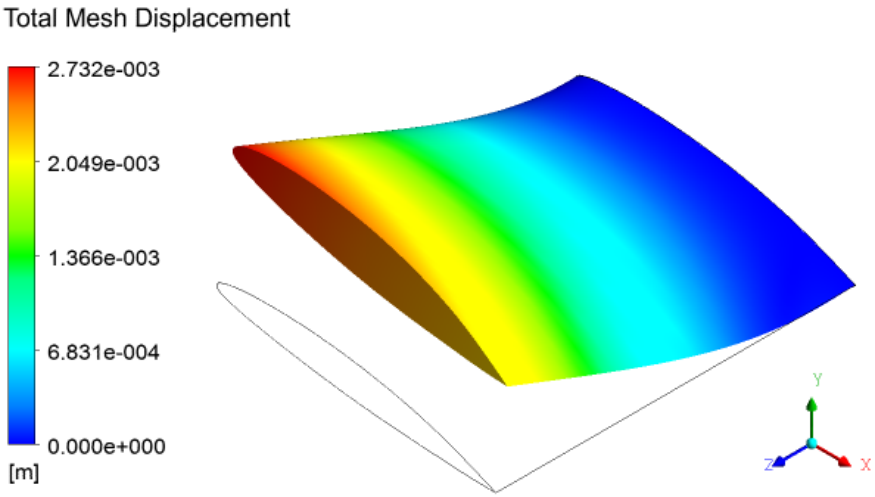

Figure 6.1 Total mesh displacement contour for the flexible hydrofoil at α=8° with u_0= $5m/s$

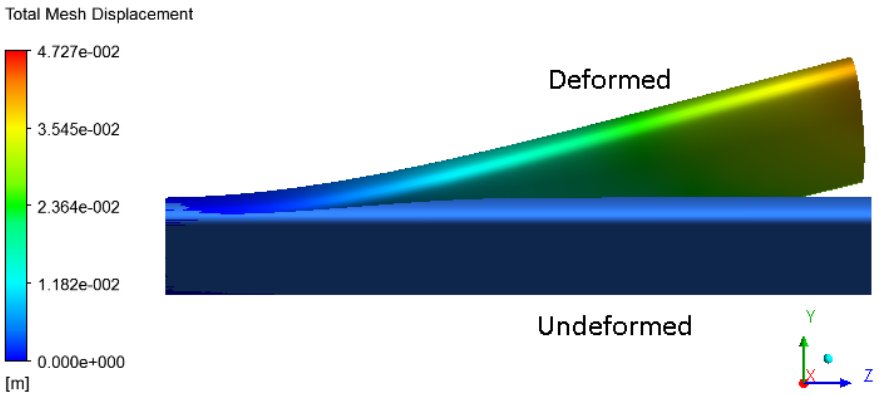

Figure 6.2 Total mesh displacement contour for the flexible hydrofoil at α=8° with u_0= $20m/s$

6.2 Pressure coefficient distribution at the hydrofoil tip

The pressure coefficients along the hydrofoil surface (at the hydrofoil free tip) are compared for rigid and flexible hydrofoils at various α subjected to flow with u_0= $10m/s$ and $15m/s$ in Fig. 6.4 and 6.5, respectively. Comparison between the rigid and flexible hydrofoils in all cases reveals that the deformation of the flexible hydrofoil leads to increases in net pressure loading as well as higher pressure gradient near the foil leading edge.

Table 6.1 shows a comparison between the minimum pressure coefficients for rigid and flexible hydrofoils subjected to flows with u_0= $10m/s$ and $15m/s$. For instance, for flows with u_0= $10m/s$ the minimum pressure coefficient drops from C_p=-4.2 for the rigid hydrofoil to C_p=-4.8 for the flexible hydrofoil at α=8° and from C_p=-2.6 for the rigid hydrofoil to C_p=-3 for

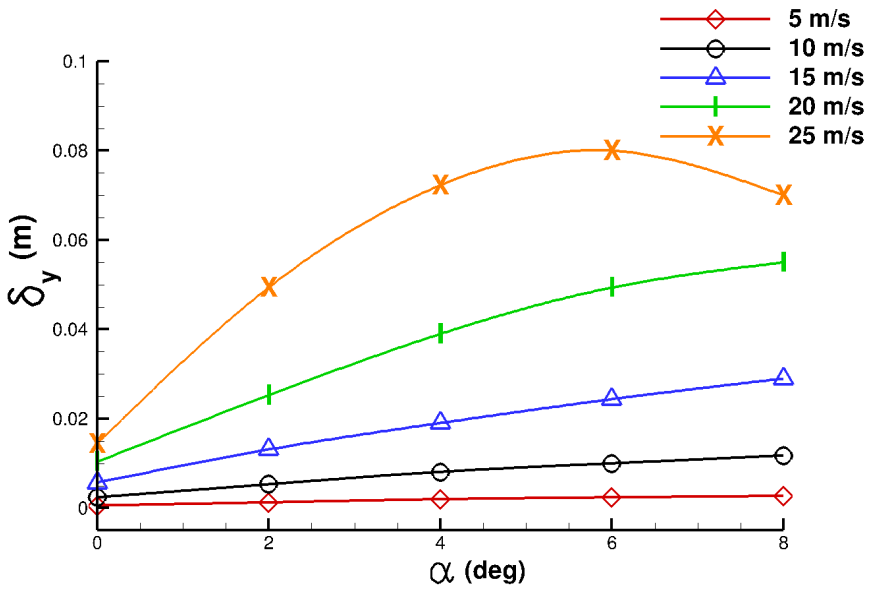

Figure 6.3 The vertical tip section displacement, δ_y, for the flexible hydrofoil at various angles of attack

the flexible hydrofoil at α=6°.

For flows with higher inlet velocities and hydrofoils at higher angles of incidence, the difference between pressure coefficient for the rigid and flexible hydrofoils becomes more noticeable because of the higher hydrodynamic loading, as depicted in Fig. 6.6 and 6.7 which compare the pressure coefficients for the rigid and the flexible hydrofoils with u_0= 20m/s and 25m/s, respectively.

6.3 Flow patterns

It has been discussed earlier that the structural behavior is affected by the transition from laminar to turbulent flow. The streamline pattern, depicted in Fig. 6.8, shows the laminar to turbulent transition by Laminar Separation Bubble (LSB) for α=0° and α=8° when u_0= 5m/s. It is shown that at small angles of attack, α=0°, the onset of flow separation occurs around the trailing edge while attached flow over the wing remains dominant. As the angle of attack increases, the separated region on the top of the wing increases in size in the vacinity of the trailing edge, and as depicted in Fig. 6.8(b), and a second LSB is induced near the foil leading edge at α=8°, due to the high pressure gradient.

To quantify the effect of foil flexibility, the velocity contours for both the rigid and flexible hydrofoils at various angles of attack are compared in Fig. 6.9, 6.10 and 6.11 for u_0= 15m/s, 20m/s and 25m/s, respectively. For lower Reynolds number flows, as shown in Fig. 6.9 for

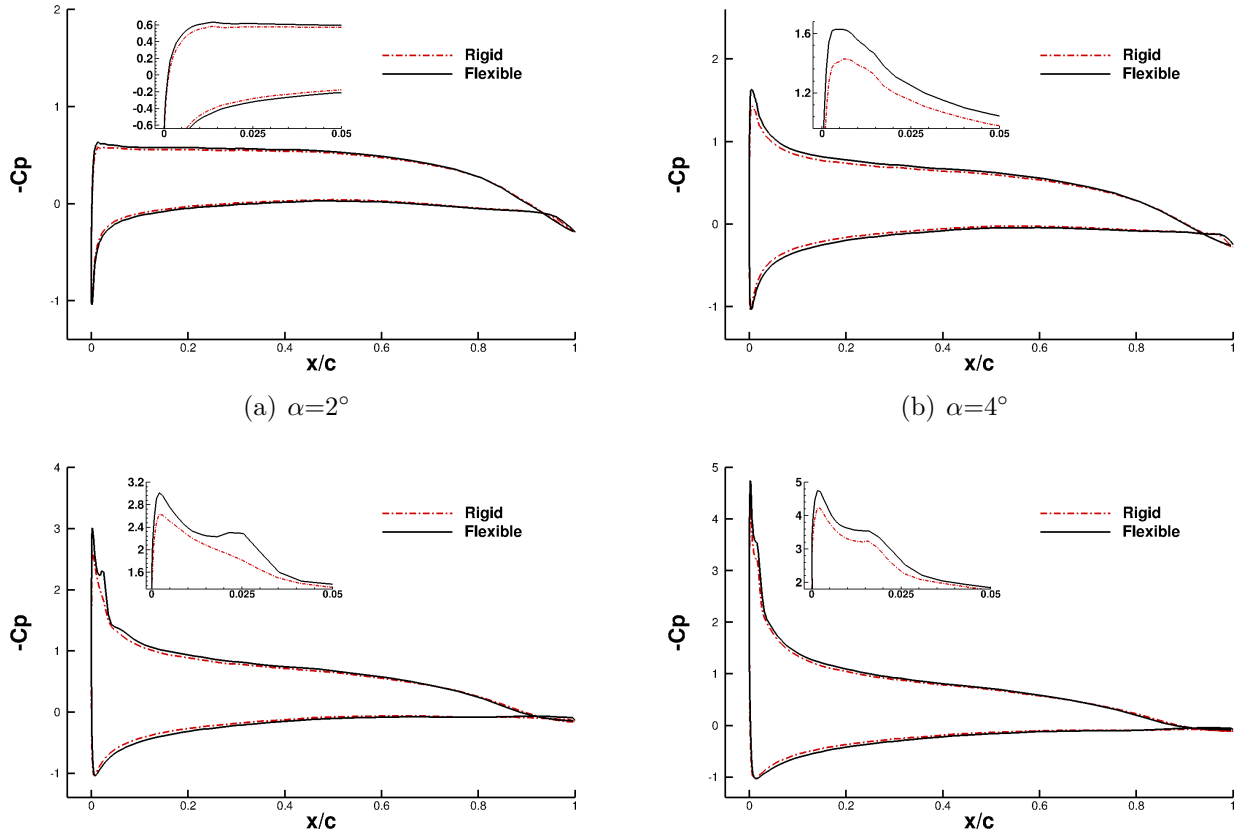

(a) α=2° (b) α=4°

(c) α=6° (d) α=8°

Figure 6.4 Pressure coefficient, C_p, for the rigid and flexible hydrofoils subjected to flow with u_0= 10m/s at: (a) α=2°, (b) α=4°, (c) α=6° and (d)α=8°

the flow velocity of u_0= 15m/s, the velocity contours for both the rigid and flexible hydrofoils are almost similar, except that the flow velocity near the leading edge of the flexible hydrofoil is higher than the rigid one. This is due to the foil deformation and the increase in the effective angle of attack. For flow velocities of u_0= 20m/s and 25m/s, a more noticeable difference is observed between the flow patterns over the rigid and flexible hydrofoils in figs. 6.10 and 6.11, because of the higher hydrodynamic loading. For both rigid and flexible hydrofoils at low angles of attack, the boundary layer experiences a laminar to turbulent transition near the trailing edge. As the angle of attack increases, the transition point moves toward the leading edge. The clockwise twist deformation of the flexible hydrofoil increases the effective angle of attack, which leads to an earlier transition to turbulence. The higher difference occurs at higher angle of attack as a result of higher hydrodynamic loading.

The flexible hydrofoil at α = 8°, which is subjected to higher inlet velocity of u_0= 20m/s,

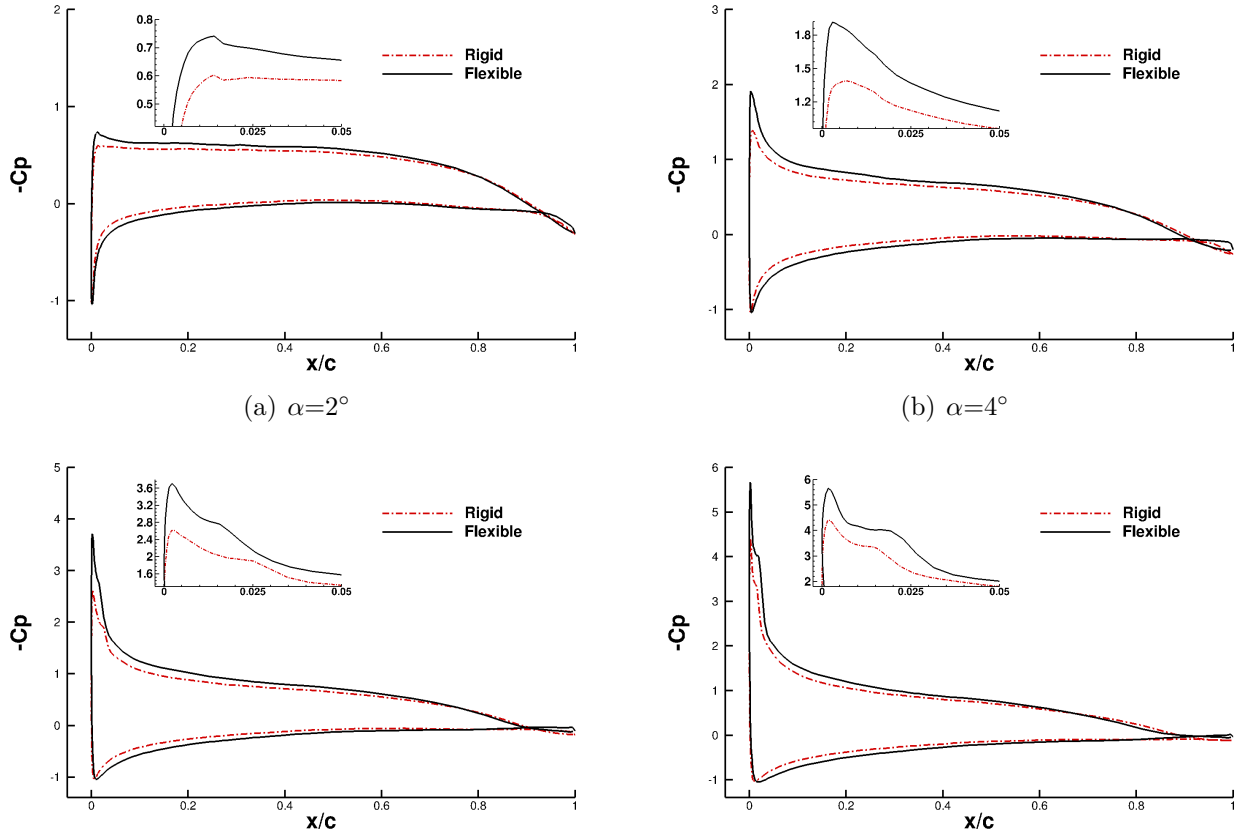

(a) α=2° (b) α=4°

(c) α=6° (d) α=8°

Figure 6.5 Pressure coefficient, C_p, for the rigid and flexible hydrofoils subjected to flow with u_0= 15m/s at: (a) α=2°, (b) α=4°, (c) α=6° and (d)α=8°

undergoes high flow-induced deformation and as a consequence, as shown in Fig. 6.10(h), the vortex developed from the foil's trailing edge moves toward the foil's leading edge, the flow becomes fully detached and stall occurs.

As shown in Fig. 6.11(f), for the flexible hydrofoil subjected to flow velocity of u_0= 25m/s, stall occurs at the angle of attack of $\alpha = 6°$.

6.4 Lift and drag coefficients

In Figs. 6.12 and 6.13, the lift and drag coefficients of the rigid hydrofoil at various angles of attack are shown together with the corresponding values for the flexible hydrofoil to illustrate the effects of flexibility on hydrodynamic coefficients. In general, the lift coefficient of the flexible hydrofoil is higher than the rigid hydrofoil. The higher lift coefficient of the flexible

Table 6.1 Comparison of the minimum pressure coefficient for the rigid and flexible hydrofoils

		$C_{p_{min}}$, Rigid	$C_{p_{min}}$, Flexible
u_0= 10m/s	α=2°	0.59	0.64
	α=4°	1.39	1.6
	α=6°	2.6	3.0
	α=8°	4.2	4.8
u_0= 15m/s	α=2°	0.6	0.74
	α=4°	1.43	1.9
	α=6°	2.64	3.7
	α=8°	4.4	5.7

hydrofoil is due to the deformation and higher effective angle of attack caused by the clockwise twist deformation, as discussed before. The higher difference is observed at higher angles of attack, due to the higher hydrodynamic loading. In addition to increases in C_L, the increase in effective angle of incidence also increases the drag coefficient, as shown in Fig. 6.13.

To illustrate the effects of Reynolds number on the hydrodynamic performance of the hydrofoils, the lift and drag coefficients of the rigid and flexible hydrofoils at various angles of attack are shown in figs. 6.14 and 6.15 for different values of inlet velocities. For rigid hydrofoils, the differences in the results due to Reynolds number effects is almost negligible, as evident from these results.

It has been discussed earlier that at highly loaded conditions, the flow-induced twist deformation of the flexible hydrofoil becomes high enough to reach stall.

It is shown in Fig. 6.14(b) and 6.15(b) that when stall occurs, at the critical angle of attack of α=6°, the slope of the lift curve ($dC_L/d\alpha$) decreases and the drag coefficient increases. For flows with inlet velocity of u_0= 25m/s, massive stall occurs at the critical angle of attack of α=6°, in which a dramatic increase is observed for the drag coefficient while the lift coefficient decreases significantly such that the slope of the lift curve becomes negative.

The direct correspondance between the C_L values in Fig. 6.14 and the foil tip displacement in Fig. 6.3 shows that the linear hydroelastic response of the flexible hydrofoil is a consequence of hydrodynamic loading only, i.e. no hysteresis or other nonlinear structural response.

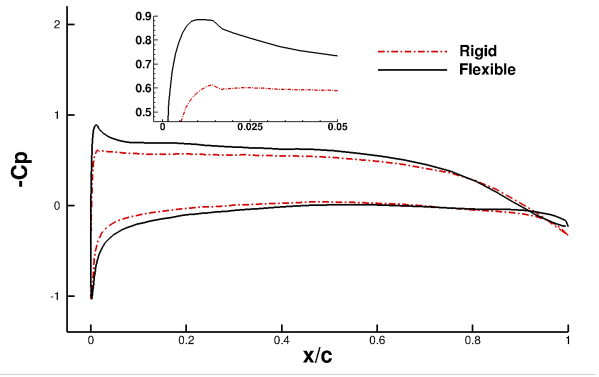

(a) α=2°

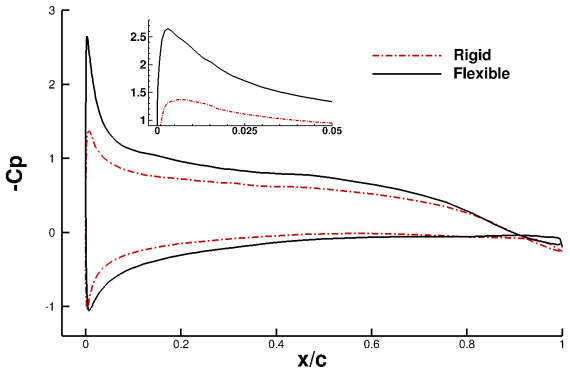

(b) α=4°

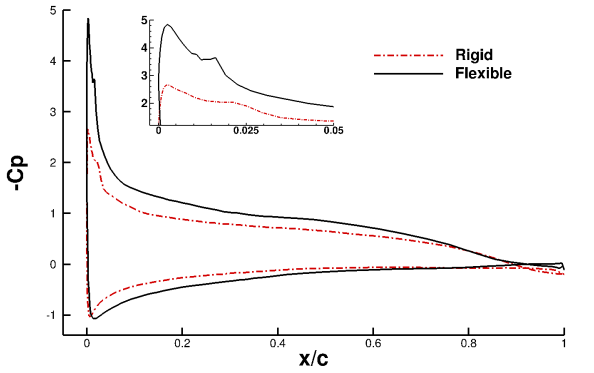

(c) α=6°

Figure 6.6 Pressure coefficient, C_p, for the rigid and flexible hydrofoils subjected to flow with u_0= 20m/s at: (a) α=2°, (b) α=4° and (c) α=6°

6.5 Pressure coefficient distribution along the span-wise direction

The pressure distribution along the hydrofoil surface at different sections in the span-direction is depicted in Fig. 6.16 and 6.17 for flexible hydrofoils at α=6° and α=8°, respectively. Considering the section, $z/b = 0$, as the fixed root of the hydrofoil, and $z/b = 1$ as the hydrofoil free tip, three-dimensional effects are clearly shown in this figure (z represents the span-wise direction and b is the foil span).

At lower hydrodynamic loading condition, it is shown that except for a small region near the foil root ($z/b = 0$ to 0.25), the pressure distribution is similar for the sections along the span. However, the difference between the pressure distribution at different sections along the span becomes much more noticeable at higher loading conditions.

It is shown in Fig. 6.17(d) that the stalled hydrofoil (at the angle of incidence of α=8°

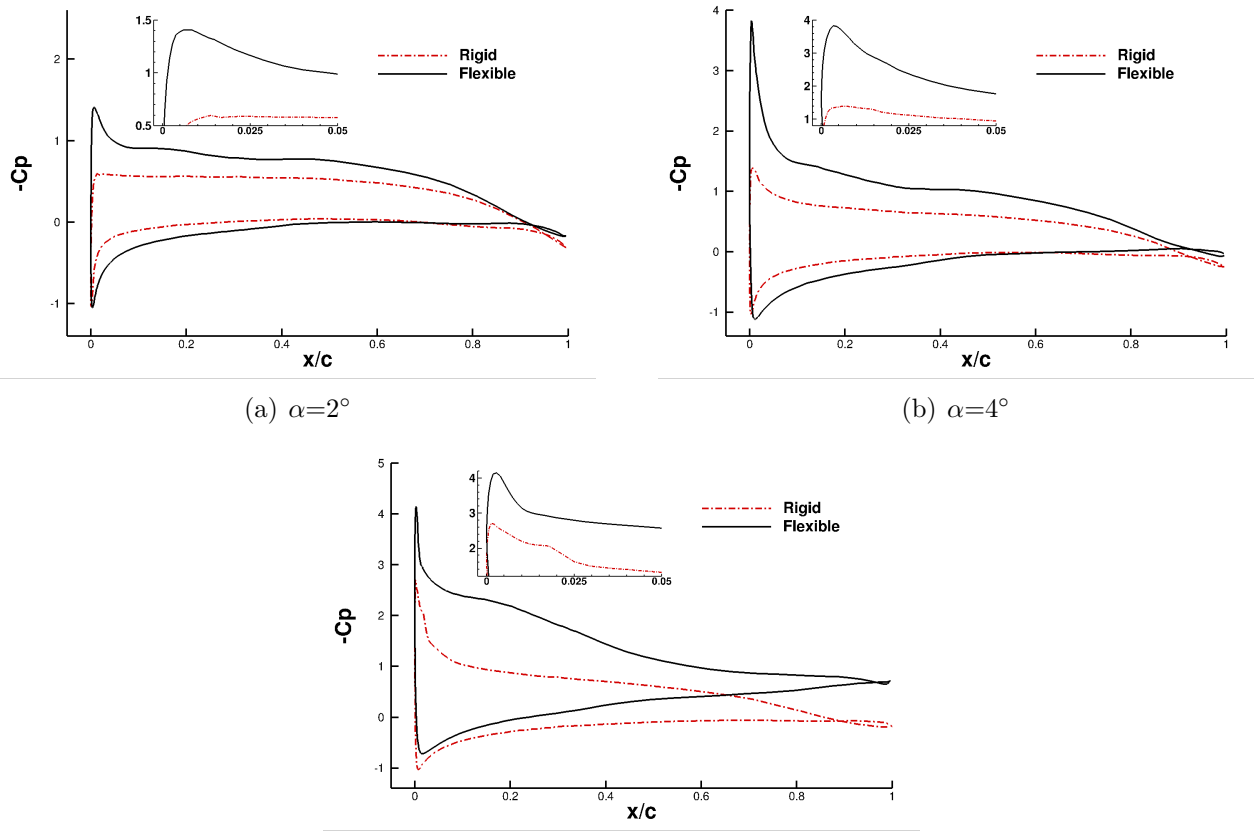

(a) α=2°

(b) α=4°

(c) α=6°

Figure 6.7 Pressure coefficient, C_p, for the rigid and flexible hydrofoils subjected to flow with u_0= 25m/s at: (a) α=2°, (b) α=4° and (c) α=6°

subjected to flow with u_0= 20m/s) experiences fully detatched flow over more than half of its span length. This 3D feature of the flow justifies why at this operating condition, the value of C_L ≈1.3 in the 2D study of (Ducoin and Young, 2013) is higher than the corresponding value of C_L=1.1 in the present study. In Fig. 6.17(d), dx represents the displacement of the foil in the stream-wise direction at the leading edge which is due to the twist deformation of the foil.

The better agreement between the results of the present 3-D simulations with the experimental data than most of the recent 2-D simulations of Akcabay et al. (2014), confirms that considering the 3-D effects is fully justified.

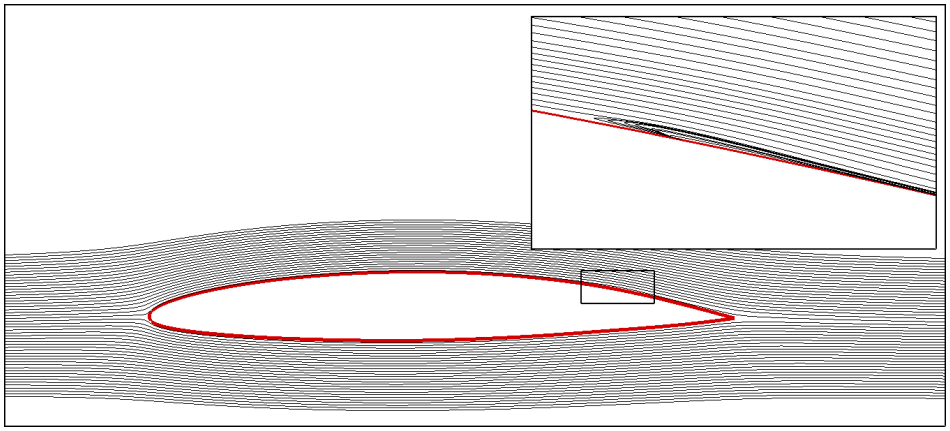

(a) α=0°

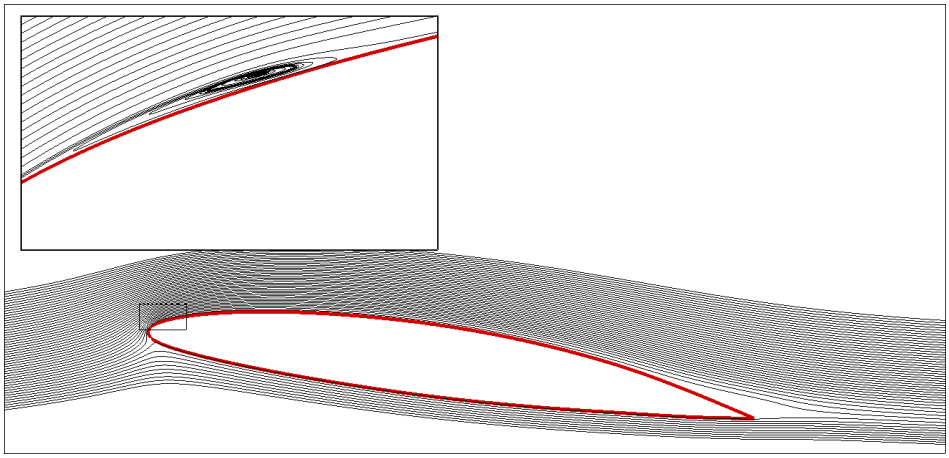

(b) α=8°

Figure 6.8 Laminar to turbulent transition and the laminar separation bubble for u_0= $5m/s$

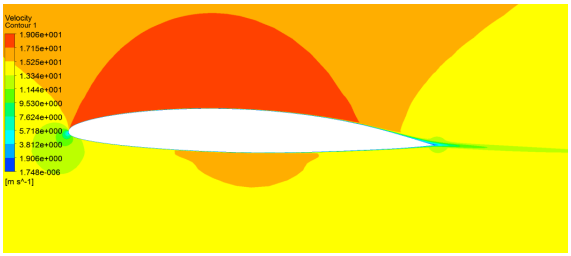

(a) rigid, $\alpha = 2°$

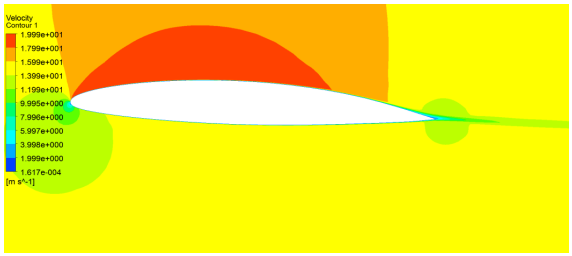

(b) flexible, $\alpha = 2°$

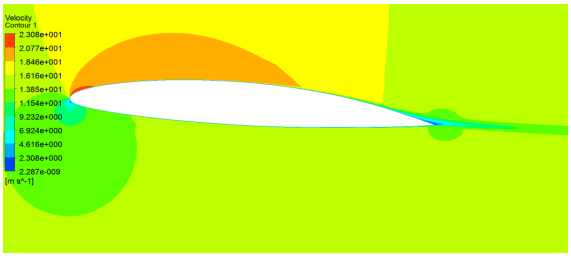

(c) rigid, $\alpha = 4°$

(d) flexible, $\alpha = 4°$

(e) rigid, $\alpha = 6°$

(f) flexible, $\alpha = 6°$

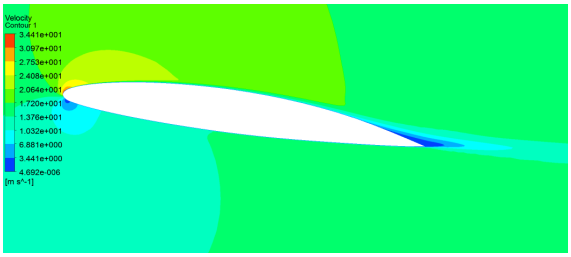

(g) rigid, $\alpha = 8°$

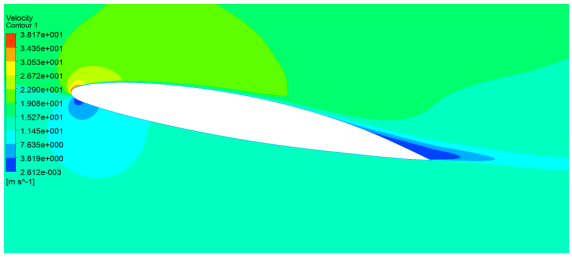

(h) flexible, $\alpha = 8°$

Figure 6.9 Comparison of the velocity contours at the free tip of the rigid (left column) and flexible (right column) hydrofoils at various angles of attack, α, for flow with u_0= $15m/s$

(a) rigid, $\alpha = 2°$

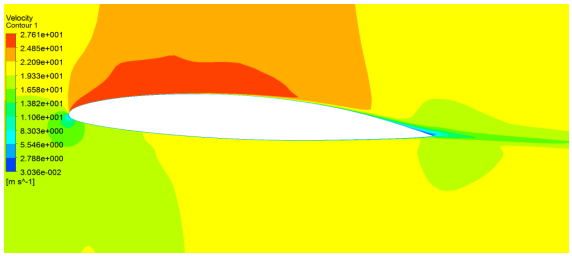

(b) flexible, $\alpha = 2°$

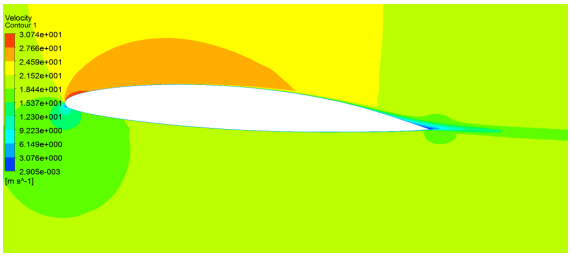

(c) rigid, $\alpha = 4°$

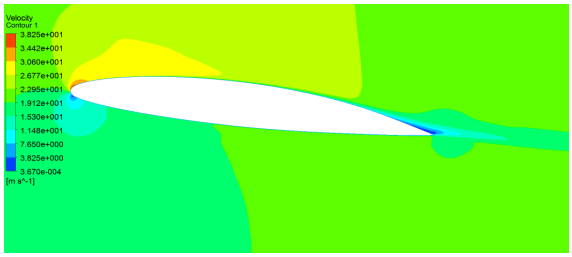

(d) flexible, $\alpha = 4°$

(e) rigid, $\alpha = 6°$

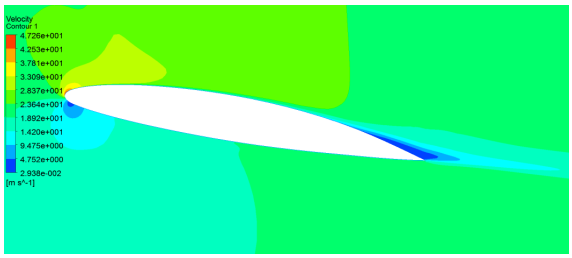

(f) flexible, $\alpha = 6°$

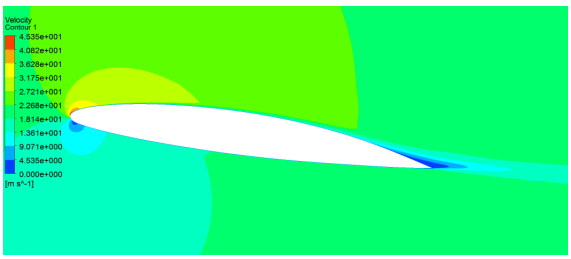

(g) rigid, $\alpha = 8°$

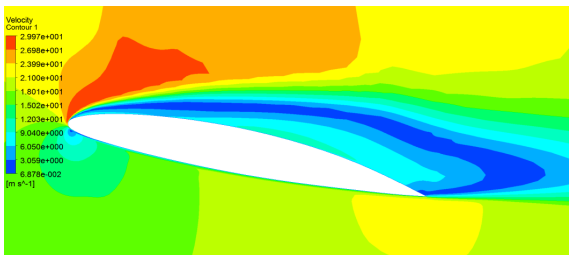

(h) flexible, $\alpha = 8°$

Figure 6.10 Comparison of the velocity contours at the free tip of the rigid (left column) and flexible (right column) hydrofoils at various angles of attack, α, for flow with u_0= $20m/s$

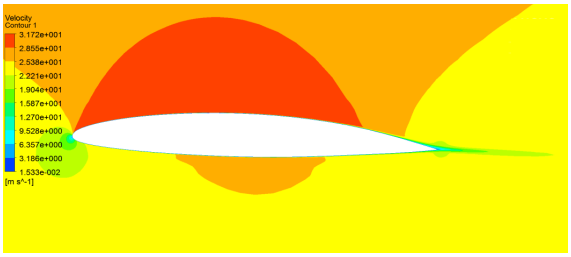

(a) rigid, $\alpha = 2°$

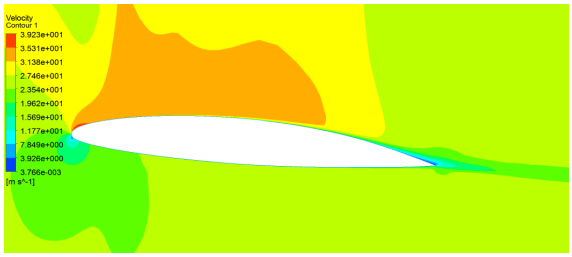

(b) flexible, $\alpha = 2°$

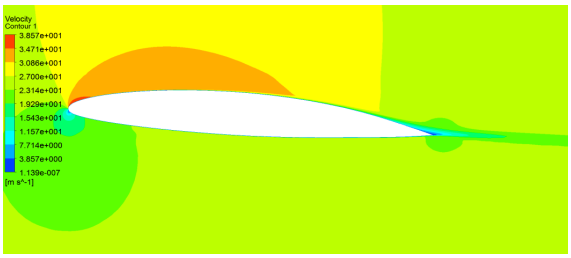

(c) rigid, $\alpha = 4°$

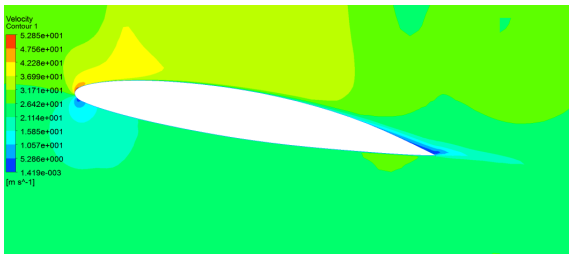

(d) flexible, $\alpha = 4°$

(e) rigid, $\alpha = 6°$

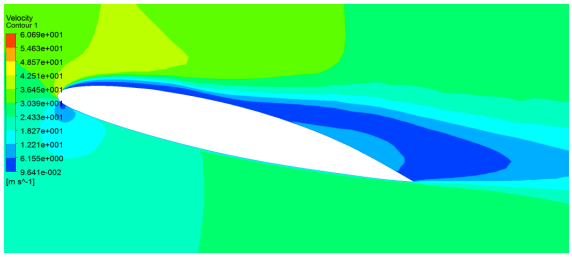

(f) flexible, $\alpha = 6°$

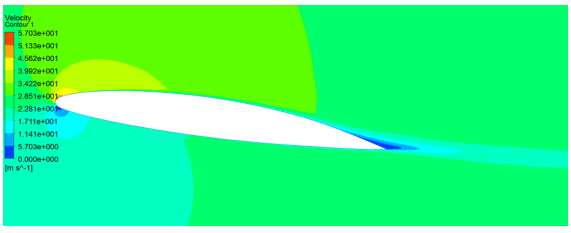

(g) rigid, $\alpha = 8°$

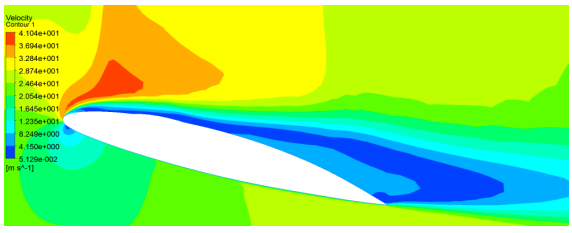

(h) flexible, $\alpha = 8°$

Figure 6.11 Comparison of the velocity contours at the free tip of the rigid (left column) and flexible (right column) hydrofoils at various angles of attack, α, for flow with u_0= $25m/s$

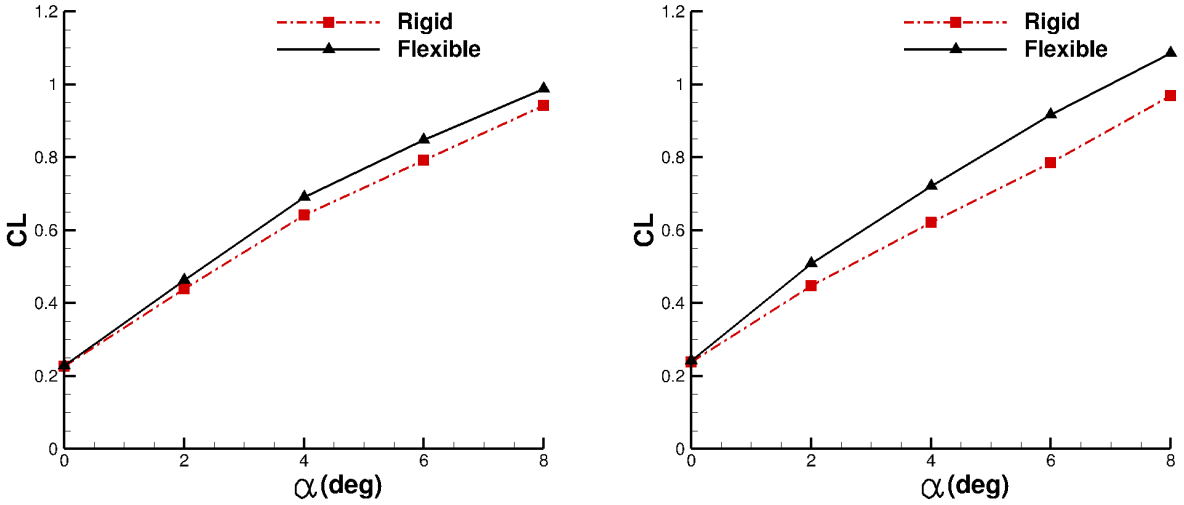

(a) u_0= $10m/s$ (b) u_0= $15m/s$

Figure 6.12 Lift coefficient for rigid and flexible hydrofoils as a function of the angle of attack

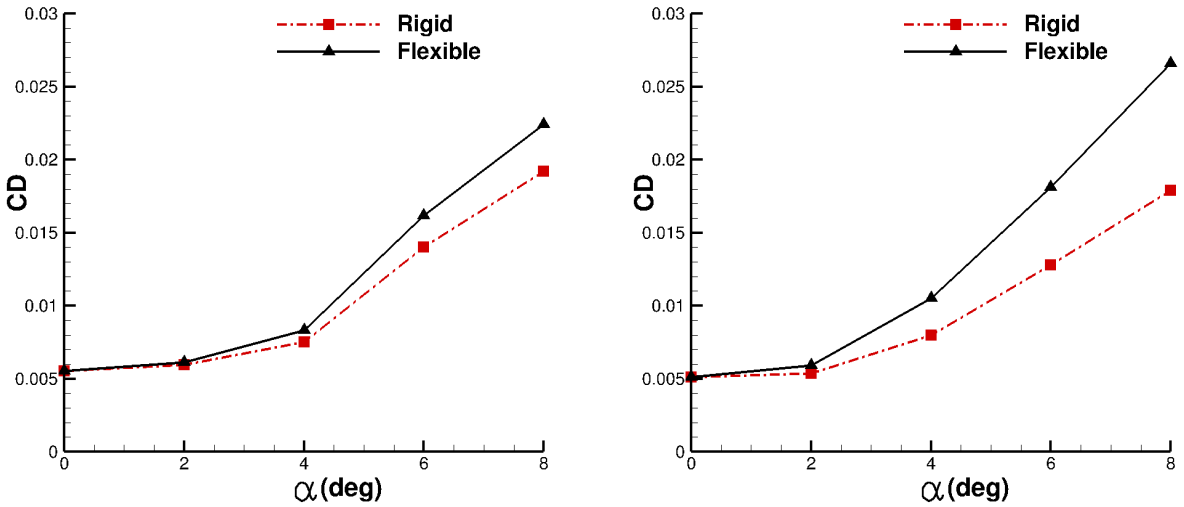

(a) u_0= $10m/s$ (b) u_0= $15m/s$

Figure 6.13 Drag coefficient for rigid and flexible hydrofoils as a function of the angle of attack

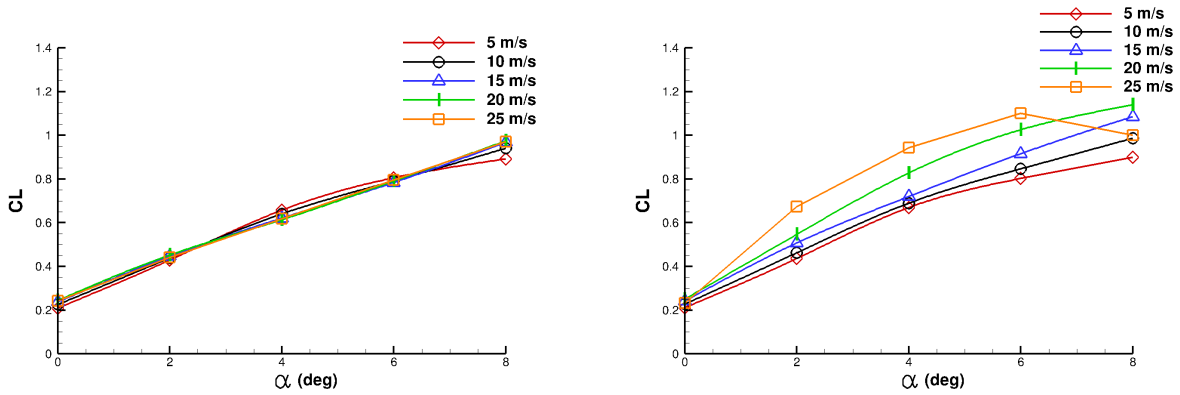

(a) rigid (b) flexible

Figure 6.14 Lift coefficient for rigid and flexible hydrofoils as a function of the angle of attack for different values of inlet velocities

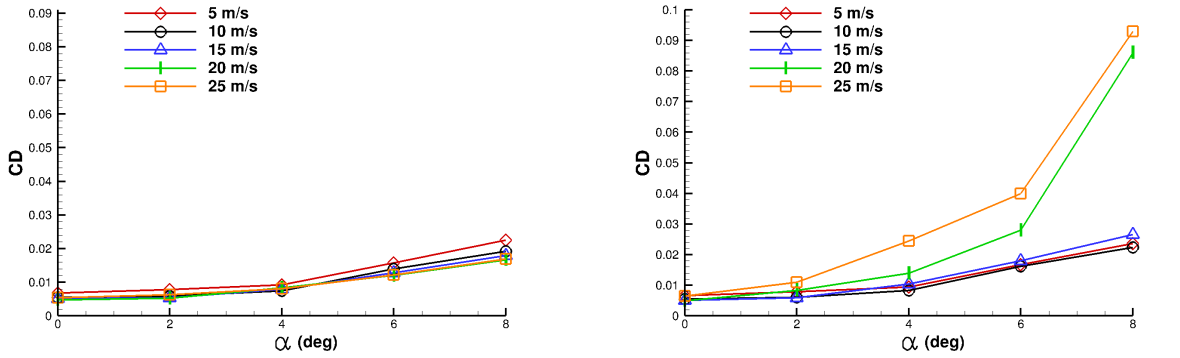

(a) rigid (b) flexible

Figure 6.15 Drag coefficient for rigid and flexible hydrofoils as a function of the angle of attack for different values of inlet velocities

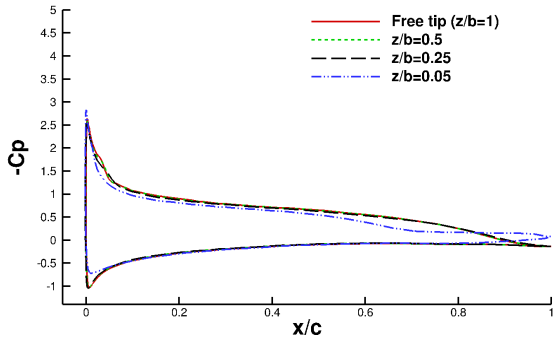

(a) u_0= $5m/s$

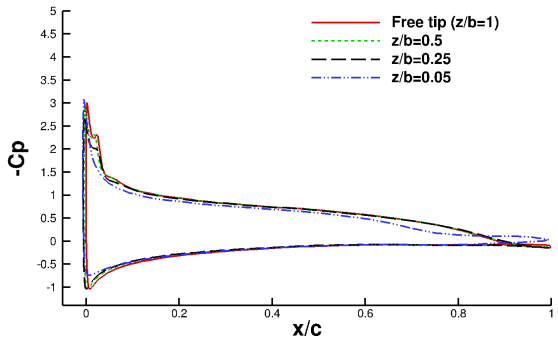

(b) u_0= $10m/s$

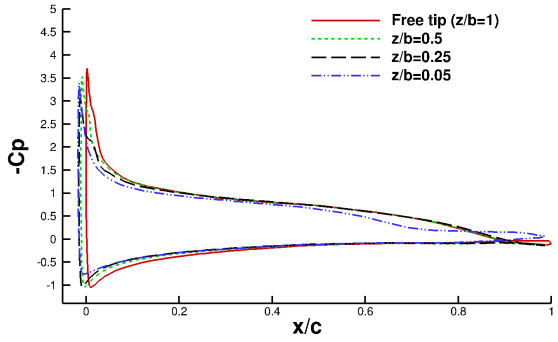

(c) u_0= $15m/s$

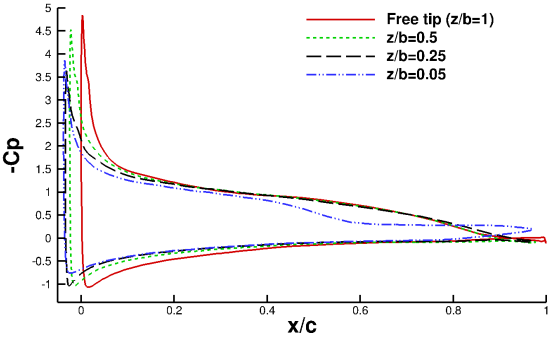

(d) u_0= $20m/s$

Figure 6.16 Pressure distribution along the hydrofoil surface at four sections in the span-wise direction for the flexible hydrofoil at α=6°

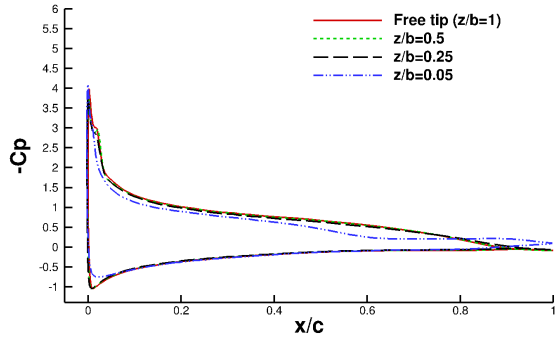

(a) u_0= $5m/s$

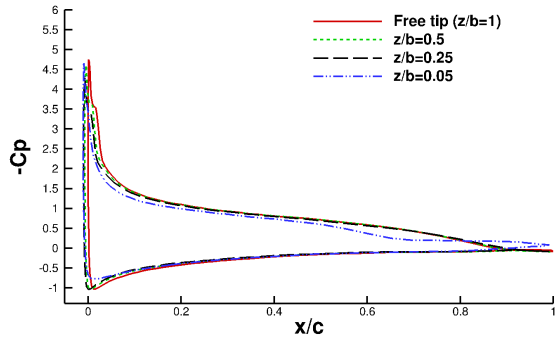

(b) u_0= $10m/s$

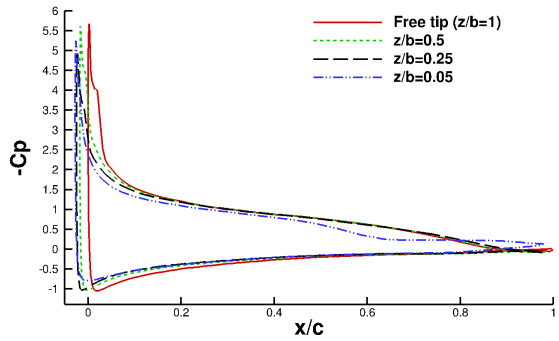

(c) u_0= $15m/s$

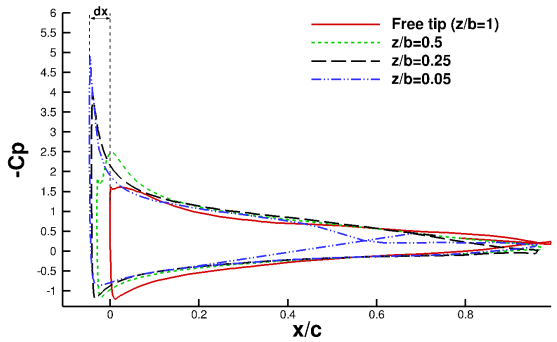

(d) u_0= $20m/s$

Figure 6.17 Pressure distribution along the hydrofoil surface at four sections in the span-wise direction for flexible hydrofoil at α=8°

CHAPTER 7 CONCLUSION

7.1 Summary

An advanced strongly-coupled two-way fluid-structure interaction methodology was proposed to investigate hydroelastic response of three-dimensional lightweight flexible hydrofoils in viscous flow at moderate to high Reynolds number. The fluid-structure problem was solved with a finite volume-based CFD code, CFX, for the fluid, which was coupled to a finite element-based CSD code ANSYS, for the structural domain. The two-way coupling capability enables CFX to work with the ANSYS Mechanical solver within an ANSYS multi-field simulation.

To investigate and quantify the FSI effects, rigid (stainless steel) and flexible (POM Polyacetate) hydrofoils were simulated and compared. The flow-induced deformation and hydroelastic response of those structures subjected to moderate to high Reynolds number flows were studied.

For the operating flow conditions of the study, numerical results revealed that the flow experiences complex boundary layer events such as laminar to turbulent transition, leading edge and trailing edge laminar separation bubbles, and flow detachment at stall. Hence, proper grid refinement was crucial for accurate prediction of these features, which have significant effects on the hydrodynamic loadings and structural response. Furthermore, to limit mesh distortion issues in the transient moving boundary problem at hand with large deformation, care was taken to ensure that the initial mesh is fine enough. In our proposed methodology, high spatial accuracy is required particularly at the interface where interaction takes place between a highly flexible stucture and a viscous flow.

Mesh convergence studies were performed and the viscous fluid solver and the coupled FSI solver were both validated by comparing the numerical results with experimental measurements. In general, very good agreement was observed; the differences were less than 1% for the lift coefficient and $\approx 4\%$ for the value of vertical displacement measured at the leading edge of the flexible foil. Comparisons showed that the present methodology has been able to improve the accuracy of the available numerical results for the lift and drag coefficients. This might be partly due to the 2D flow assumption in the previous studies, which ignored 3D effects, such as the contributions from the induced drag due to the finite aspect ratio and the boundary layer effects at the foil root, whereas these are accounted for in the present study. The 2D hydrofoil assumption in the previous numerical studies and neglecting the effects of the fixed root lead to noticeable discrepancies in the magnitudes of the hydrofoil displace-

ment (error of 58% between the experimental and numerical values in the study of (Akcabay et al., 2014)), while in the present study the difference between the experimental and numerical results is $\approx 4\%$. Considering all the structural DOFs, the solution of the complete set of structural equations and incorporating a two-way FSI coupling method in the current study also provides more accurate results than other FSI methods in the previous numerical studies. Furthermore, in the present study the SST turbulence model was coupled with a transition model, whereas no transition modelling has been used in the studies of Akcabay et al. (Akcabay et al., 2014) and (Wu et al., 2015). It was shown that the incorporation of transition modeling plays a major role in the accurate prediction of the flow separation, which has immidiate effect on the hydrodynamic response of the hydrofoils.

7.2 Limitations and future work

Regarding the proposed methodology for modeling 3D flexible hydrofoils, there are some numerical limitations and hence, the following subjects are suggested for future works:

- The current FSI methodology is limited to steady-state assumptions. Additional studies are needed to analyze the dynamic FSI effects and investigate the transient vibration characteristics due to transition and load fluctuations associated with large scale vortex shedding, as well as buffeting, resonance, and flutter instabilities.
- Additional studies are needed to investigate flexible hydrofoils at higher angles of attack and higher inflow velocities; i.e. at post-stall condition, where the unsteady vortex shedding frequency may lock in to one of the foil natural frequencies.
- Although the 3D flow effects caused by foil spanwise/chordwise bending and twist deformations are accounted for in the present study, gap flow and the effects of tip vortices are neglected. Further investigation is needed to study these features.
- Due to the limitations in the mesh deformation technique, higher structural deformation as a result of higher hydrodynamic loading lead to mesh distortion issues in the present study. This requires further investigation and more suitable numerical techniques, such as variable mesh stiffness model exponent, are needed to overcome this issue.
- Although the flow was relatively complex, the unsteady 3D simulation times for one-way coupling were reasonable. However, for the two-way coupling analyses, the simulations were super long. Therefore, two-way analysis should only be undertaken when absolutely necessary.

- More numerical simulations with different flexible materials, are needed to improve our understanding of flow-induced vibrations and the resulting effects on the performance and stability of lifting bodies. For instance, with the increased interest in the use of composites as alternate materials for marine propellers, more investigations need to be undertaken to understand how the use of such materials can offer the potential benefits of reduced corrosion and cavitation damage, improved fatigue performance, lower noise, improved material damping properties, and reduced lifetime maintenance cost.

- The small time-step sizes for the test cases of flow over flexible hydrofoils, lead to transient start-up convergence problems and solver failure. Although the choice of larger time-steps in the present study with negligible transient features is justified, this issue needs further investigations for the study of dynamic FSI effects and investigation of the transient load fluctuations and structural instabilities.

REFERENCES

D. T. Akcabay and Y. L. Young, "Influence of cavitation on the hydroelastic stability of hydrofoils," *Journal of Fluids and Structures*, vol. 49, pp. 170–185, 2014.

D. T. Akcabay and Y. Young, "Hydroelastic response and energy harvesting potential and flexible piezoelectric beams in viscous flow," *Physics of Fluids*, vol. 24, no. 5, 2012.

D. T. Akcabay, E. J. Chae, Y. L. Young, A. Ducoin, and J. A. Astolfi, "Cavity induced vibration of flexible hydrofoils," *Journal of Fluids and Structures*, vol. 49, pp. 463–484, 2014.

D. T. Akcabay, J. Xiao, and Y. L. Young, "Numerical stabilities of loosely coupled methods for robust modeling of lightweight and flexible structures in incompressible and viscous flows," *Acta Mechanica Sinica*, vol. 33, no. 4, pp. 709–724, 2017.

J. M. Anderson, K. Streitlien, D. S. Barrett, and M. S. Triantafyllou, "Oscillating foils of high propulsive efficiency," *Journal of fluid mechanics*, vol. 360, pp. 41–72, 1998.

A. Barker and X.-C. Cai, "Scalable parallel methods for monolithic coupling in fluid–structure interaction with application to blood flow modeling," *Journal of Computational Physics*, vol. 229, pp. 642–659, 2010.

O. O. Bendiksen, "Role of shock dynamics in transonic flutter," *AIAA paper*, vol. 2121, pp. 401–414, 1992.

O. Bendiksen, "Multibranch and period tripling flutter," in *IMECE2002 ASME International Mechanical Engineering Congress and Exposition*, New Orleans, Louisiana, USA, 2002.

F. Benra, H. J. Dohmen, J. P. S. Schuster, and B. Wan, "A comparison of one-way and two-way coupling methods for numerical analysis of fluid-structure interactions," *Journal of Applied Mathematics*, vol. 2011, p. 16 pages, 2011.

V. Carstens, R. Kemme, and S. Schmitt, "Coupled simulation of flow-structure interaction in turbomachinery," *Aerospace Science and Technology*, vol. 7, pp. 298–306, 2003.

E. J. Chae, D. T. Akcabay, and Y. L. Young, "Dynamic response and stability of a flapping foil in a dense and viscous fluid," *Physics of Fluids*, vol. 25, no. 10, 2013.

E. J. Chae, D. T. Akcabay, A. Lelong, J. A. Astolfi, and Y. L. Young, "Numerical and experimental investigation of natural flow-induced vibrations of flexible hydrofoils," *Physics of Fluids*, vol. 28, p. 075102, 2016.

E. J. Chae, D. T. Akcabay, and Y. L. Young, "Influence of flow-induced bend–twist coupling on the natural vibration responses of flexible hydrofoils," *Journal of Fluids and Structures*, vol. 69, no. Supplement C, pp. 323–340, 2017.

L. J. Clancy, *Aerodynamics*. New York : Wiley, 1975.

B. S. H. Connell and D. K. P. Yue, "Flapping dynamics of a flag in a uniform stream," *Journal of Fluid Mechanic*, vol. 581, no. 1, pp. 33–67, 2007.

A. Coutu, D. Proulx, S. Coulson, and A. Demers, "Dynamic assessment of hydraulic turbines-high head francis," in *Hydrovision*, Montréal, 2004.

A. Coutu, H. Aunemo, B. Badding, and O. Velagandula, "Dynamic behaviour of high head francis turbines," in *Hydro 2005*, Villach, Austria, 2005.

A. Coutu, C. Monette, and O. Velagandula, "Francis runner dynamic stress calculations," in *Hydro 2007*, Granada, Spain, 2007.

E. H. Dowell and K. C. Hall, "Modeling of fluid–structure interaction," *Annual Review of Fluid Mechanics*, vol. 33, pp. 445–490, 2001.

A. Ducoin and Y. L. Young, "Hydroelastic response and stability of a hydrofoil in viscous flow," *Journal of Fluids and Structures*, vol. 38, pp. 40–57, 2013.

A. Ducoin, J. Astolfi, F. Deniset, J. Sigrist, and V. Soyer, "An experimental and numerical investigation of flow over a hydrofoil in transient regimes based on wall-pressure analysis, volume 4: Fluid-structure interaction," in *ASME Pressure Vessels and Piping Division Conference*, Chicago, Illinois, USA, 2008.

A. Ducoin, J. A. Astofli, F. Deniset, and J. F. Sigrist, "An experimental and numerical study of the hydroelastic behavior of an hydrofoil in transient pitching motion," in *First International Symposium on Marine Propulsors*, Trondheim, Norway, 2009.

A. Ducoin, J. A. Astolfi, F. Deniset, and J. F. Sigrist, "Computational and experimental investigation of flow over a transient pitching hydrofoil," *European Journal of Mechanics/BFluids*, vol. 28, pp. 728–743, 2009.

A. Ducoin, J. A. Astolfi, and M. L. Gobert, "An experimental study of boundary-layer transition induced vibrations on a hydrofoil," *Journal of Fluids and Structures*, vol. 32, pp. 37–51, 2012.

A. Ducoin, J. A. Astolfi, and J. Sigrist, "An experimental analysis of fluid structure interaction on a flexible hydrofoil in various flow regimes including cavitating flow," *European Journal of Mechanics/BFluids*, vol. 36, pp. 63–74, 2012.

I. E. Garrick, *Bending-torsion flutter calculations modified by subsonic compressibility corrections*, Technical Report No. 836 (National Advisory Committee for Aeronautics), 1946.

M. Gee, "Truly monolithic algebraic multigrid for fluid–structure interaction," *International Journal for Numerical Methods in Engineering*, vol. 85, pp. 987–1016, 2011.

N. Gregory and C. L. O'Reilly, "Low-speed aerodynamic characteristics of naca 0012 aerofoil section, including the effects of upper-surface roughness simulating hoar frost," in *NASA Reports and Memoranda No. 3726*, 1970.

W. Haase, B. Aupoix, U. Bunge, and D. Schwamborn, *FLOMANIA - A European Initiative on Flow Physics Modelling*. Berlin: Springer, 2006.

C. Harwood, J. Ward, Y. L. Young, and S. Ceccio, "Experimental investigation of the hydroelastic response of a surface-piercing hydrofoil in multi-phase flow," in *31st Symposium on Naval Hydrodynamics*, Monterey, California, 2016.

D. H. Hodges and G. Pierce, *Introdutction to Structural Dynamics and Aeroelasticity (Fourth edition)*. Kluwer Academic Publishers, Dordrecht/Boston/London, 2004.

G. Hou, J. Wang, and A. Layton, "Numerical methods for fluid-structure interaction — a review," *Communications in Computational Physics*, vol. 12, no. 2, p. 337–377, 2012.

R. F. Huang and C. L. Lin, "Vortex shedding and shear-layer instability of wing at low-reynolds numbers," *AIAA Journal*, vol. 3, no. 8, pp. 1398–1403, 1995.

S. R. Hutchison, "Numerical modelling of hydrofoil fluid-structure interaction," Ph.D. dissertation, University of Tasmania, 2012.

Y. W. Jung and S. O. Park, "Vortex-shedding characteristics in the wake of an oscillating airfoil at low reynolds number," *Journal of Fluid and Structures*, vol. 20, pp. 451–464, 2005.

C. L. Ladson, "Effects of independent variation of mach and reynolds numbers on the low-speed aerodynamic characteristics of the naca 0012 airfoil section," in *NASA TM 4074*, 1988.

W. M. Lai, E. Krempl, and D. Rubin, *Introduction to Continuum Mechanics, Fourth Edition*. Burlington, Elsevier Science, 2010.

T. Lee and P. Gerontakos, "Investigation of flow over an oscillating airfoil," *Journal of Fluid Mechanics*, vol. 512, pp. 313–341, 2004.

E. Lefrançois, "How an added mass matrix estimation may dramatically improve fsi calculations for moving foils," *Applied Mathematical Modelling*, vol. 51, pp. 655–668, 2017.

E. Lefrançois, B. Anais, and S. Mottelet, "Strongly coupling partitioned scheme for enhanced added mass computation in 2d fluid-structure interaction," *Coupled Systems Mechanics, An International Journal*, vol. 5, pp. 235–254, 2016.

J. Leroux, J. Astolfi, and J. Billard, "An experimental study of unsteady partial cavitation," *Journal of Fluids Engineering*, vol. 126, pp. 94–101, 2004.

T. Liaghat, "Two-way fluid-structure coupling in vibration and damping analysis of an oscillating hydrofoil," Master's thesis, École polytechnique de Montreal, Montreal, Canada, 2014.

T. Liaghat, F. Guibault, L. Allenbach, and B. Nennemann, "Two-way fluid-structure coupling in vibration and damping analysis of an oscillating hydrofoil," *ASME 2014 International Mechanical Engineering Congress and Exposition (American Society of Mechanical Engineers)*, vol. 4A, p. V04AT04A073 (10 pages), 2014.

H. G. Matthies and J. Steindorf, "Partitioned strong coupling algorithms for fluid−structure interaction," *Computers & Structures*, vol. 81, no. 8–11, pp. 805 – 812, 2003, k.J Bathe 60th Anniversary Issue.

F. R. Menter and Y. Egorov, "A scale-adaptive simulation model using two-equation models," in *43rd AIAA Aerospace Sciences Meeting and Exhibit*, American Institute of Aeronautics and Astronautics Inc., 2005, pp. 271–283.

F. R. Menter, M. Kuntz, and R. Langtry, "Ten years of industrial experience with the sst turbulence model. begell," 2003.

F. R. Menter, R. B. Langtry, S. R. Likki, Y. B. Suzen, P. G. Huang, and S. Völker, "A correlation-based transition model using local variables: Part I — model formulation," in *ASME. Turbo Expo: Power for Land, Sea, and Air, Volume 4: Turbo Expo*, Vienna, Austria, 2004.

F. Menter, R. Langtry, and S. Völker, "Transition modelling for general purpose cfd codes," *Flow, Turbulence and Combustion*, vol. 77, no. 1, p. 277–303, 2006.

S. Moffatt and L. He, "On decoupled and fully-coupled methods for blade forced response prediction," *Journal of Fluids and Structures*, vol. 20, pp. 217–234, 2005.

Z. Mortazavinia, A. Zare, and A. Mehdizadeh, "Effects of renal artery stenosis on realistic model of abdominal aorta and renal arteries incorporating fluid-structure interaction and pulsatile non-newtonian blood flow," *Applied Mathematics and Mechanics*, vol. 33, no. 2, pp. 165–176, 2012.

C. Munch, P. Ausoni, and O. Braun, "Fluid-structure coupling for an oscillating hydrofoil," *Journal of Fluids and Structures*, vol. 26, pp. 1018–1033, 2010.

R. Nichols, *Turbulence Models and Their Application to Complex Flows.* University of Alabama at Birmingham, 09 2010.

D. Poirel and W. Yuan, "Aerodynamics of laminar separation flutter at a transitional reynolds number," *Journal of Fluid and Structures*, vol. 26, no. 7-8, pp. 1174–1194, 2010.

D. Poirel, Y. Harris, and A. Benaissa, "Self-sustained aeroelastic oscillations of a naca0012 airfoil at low-to-moderate reynolds numbers," *Journal of Fluid and Structures*, vol. 24, no. 5, pp. 700–719, 2008.

R. S. Raja, "Coupled fluid structure interaction analysis on a cylinder exposed to ocean wave loading," Master's thesis, Chalmers University of Technology, Göteborg, Sweden, 2012.

M. Reese, "Vibration and damping of hydrofoils in uniform flow," Ph.D. dissertation, Pennsylvania State University, 2010.

C. Rhie and W. Chow, "Numerical study of the turbulent flow past an airfoil with trailing edge separation," *AIAA Journal*, vol. 21, pp. 1525–1532, 1983.

P. B. Ryzhakov, R. Rossi, S. R. Idelsohn, and E. Oñate, "A monolithic lagrangian approach for fluid–structure interaction problems," *Computational Mechanics*, vol. 46, no. 6, pp. 883–899, Nov 2010.

W. R. Sears, "Some aspects of non-stationary airfoil theory and its practical application," *Journal of the Aeronautical Sciences(Institute of the Aeronautical Sciences)*, vol. 8, no. 3, pp. 104–108, 1941.

C. Seeley, A. Coutu, C. Monette, B. Nennemann, and H. Marmont, "Characterization of hydrofoil damping due to fluid–structure interaction using piezocomposite actuators," *Smart Materials and Structures*, vol. 21, p. 035027 (9pp), 2012.

A. Shelton, J. Abras, B. Hathaway, M. Sanchez-Rocha, M. Smith, and S. Menon, "An investigation of the numerical prediction of static and dynamic stall," in *Proceedings of the 61 American Helicopter Society Annual Forum*, Grapevine, 2005.

M. Smith, T. Wong, M. Potsdam, J. Baeder, and S. Phanse, "Evaluation of cfd to determine two-dimensional airfoil characteristics for rotorcraft applications," in *American Helicopter Society 60th Annual Forum*, Baltimore, MD, 2004.

M. Song, E. Lefrancois, and M. Rachik, "A partitioned coupling scheme extended to structures interacting with high-density fluid flows," *Computers & Fluids*, vol. 84, pp. 190–202, 2013.

F. Sotiropoulos and X. Yang, "Immersed boundary methods for simulating fluid–structure interaction," *Progress in Aerospace Sciences*, vol. 65, pp. 1–21, 2014.

H. Tennekes and J. L. Lumley, *A First Course in Turbulence*. Cambridge, MA: MIT Press, 1972.

B. Thapa, A. Panthee, and B. Thapa, "Computational methods in research of hydraulic turbines operating in challenging environments," *International Journal of Advanced Renewable Energy Research*, vol. 1, no. 2, pp. 1–4, 2012.

T. Theodorsen, *General theory of aerodynamic instability and the mechanism of flutter*, Technical Report No. 496 (National Advisory Committee for Aeronautics), 1935.

D. M. Tran, C. Liauzun, and C. Labaste, "Methods of fluid-structure coupling in frequency and time domains using linearised aerodynamics for turbomachinery," *Journal of Fluids and Structures*, vol. 20, p. 1161–1180, 2005.

T. Tran, B. Nennemann, T. C. Vu, and F. Guibault, "Investigation of cavitation models for steady and unsteady cavitating flow simulation," *International Journal of Fluid Machinery and Systems*, vol. 8, pp. 240–253, 10 2015.

M. R. Visbal, R. E. Gordnier, and M. C. Galbraith, "High-fidelity simulations of moving and flexible airfoils at low reynolds numbers," *Experiments in Fluids*, vol. 46, pp. 903–922, 2009.

J. Ward, C. Harwood, and Y. Young, "Inverse method for hydrodynamic load reconstruction on a flexible surface-piercing hydrofoil in multi-phase flow," *Journal of Fluids and Structures*, vol. 77, pp. 58–79, 2018.

Wikipedia, *Flow separating from a foil and stall at high angles of attack, (accessed April 23, 2018)*, 2018, https://en.wikipedia.org/wiki/Stall_(fluid_mechanics).

Q. Wu, B. Huang, G. Wang, and Y. Gao, "Experimental and numerical investigation of hydroelastic response of a flexible hydrofoil in cavitating flow," *International Journal of Multiphase Flow*, vol. 74, 09 2015.

Q. Wu, B. Huang, G. Wang, and S. Cao, "The transient characteristics of cloud cavitating flow over a flexible hydrofoil," *International Journal of Multiphase Flow*, vol. 99, pp. 162–173, 2018.

Z. Yao, F. Wang, M. Dreyer, and M. Farhat, "Effect of trailing edge shape on hydrodynamic damping for a hydrofoil," *Journal of fluids and structures*, vol. 51, p. 189–198, 2014.

Y. Young, "Time-dependant hydroelastic analysis of cavitating propulsors," *Journal of Fluids and Structures*, vol. 23, pp. 269–295, 2007.

Y. L. Young, "Fluid-structure interaction analysis of flexible composite marine propellers," *Journal of Fluids and Structures*, vol. 24, pp. 799–818, 2008.

Y. L. Young and S. A. Kinnas, "Numerical analysis of surface-piercing propellers," in *Propellers/Shafting 2003*, Virginia Beach, VA., 2003.

Y. Young and S. A. Kinnas, "Numerical modeling of supercavitating propeller flows," *Journal of Ship Research*, vol. 47, no. 1, 2003.

Y. L. Young and S. A. Kinnas, "Performance prediction of surface-piercing propellers," *Journal of Ship Research*, vol. 48, no. 4, pp. 288–304, 2004.

Y. L. Young and B. R. Savander, "Numerical analysis of large-scale surfacepiercing propellers," *Ocean Engineering*, vol. 38, pp. 1368–1381, 2011.

Y. L. Young, E. J. Chae, and D. T. Akcabay, "Hybrid algorithm for modeling of fluid-structure interaction in incompressible, viscous flows," *Acta Mechanica Sinica*, vol. 28, no. 4, pp. 1030–1041, 2012.

APPENDIX A COORDINATES OF THE NACA66 HYDROFOIL

x/c	y/c	x/c	x/c
0.0	0.0	0.0	0.0
-0.000173	0.002046	0.000123	-0.000530
0.000246	0.004647	0.001125	-0.002977
0.001346	0.00711	0.002705	-0.005255
0.003148	0.009593	0.004941	-0.007456
0.005551	0.012035	0.007885	-0.009478
0.008995	0.014762	0.012011	-0.011509
0.013509	0.017653	0.017255	-0.013475
0.019545	0.020864	0.024086	-0.015482
0.02707	0.024273	0.03244	-0.017467
0.036197	0.027872	0.042411	-0.019444
0.046867	0.031575	0.053931	-0.021377
0.059025	0.035312	0.06693	-0.023242
0.072601	0.039049	0.081336	-0.025035
0.087531	0.042754	0.09708	-0.026756
0.10375	0.046389	0.114097	-0.028391
0.121195	0.049922	0.132317	-0.029933
0.139799	0.053343	0.151675	-0.031393
0.159495	0.056643	0.172102	-0.032772
0.180221	0.059786	0.193536	-0.034041
0.201918	0.062725	0.215911	-0.035169
0.224521	0.065435	0.23916	-0.036161
0.247963	0.067921	0.263218	-0.037034
0.272179	0.070179	0.288017	-0.037790
0.297102	0.072199	0.313493	-0.038414
0.322671	0.073961	0.339581	-0.038910
0.348822	0.075431	0.366214	-0.039267
0.375488	0.076615	0.393327	-0.039470
0.402604	0.077522	0.420855	-0.039540
0.430107	0.078104	0.448731	-0.039410
0.457932	0.0783	0.47689	-0.039042
0.48601	0.078085	0.505264	-0.038453
0.514276	0.077477	0.533788	-0.037652
0.542662	0.076471	0.562395	-0.036640
0.571101	0.075059	0.591019	-0.035423
0.599524	0.073243	0.619594	-0.034009
0.627866	0.071022	0.648054	-0.032405
0.656057	0.06839	0.676334	-0.030630
0.68403	0.065358	0.704371	-0.028722
0.711719	0.061944	0.7321	-0.026703
0.739054	0.058133	0.759457	-0.024586
0.765966	0.053929	0.786385	-0.022480
0.792374	0.049272	0.812828	-0.020500
0.8182	0.044138	0.838712	-0.018533
0.843402	0.038681	0.863964	-0.016484
0.867937	0.033027	0.888517	-0.014315
0.891756	0.02725	0.9123	-0.012005
0.914812	0.021431	0.935248	-0.009564
0.93706	0.015648	0.957425	-0.006953
0.958581	0.009949	0.978894	-0.004146
0.979449	0.004342	1.0	-0.001178
1.0	-0.001178		